Thesis for the Master's degree in chemistry

Shewangizaw Teketel

Studies of the Methanol-to-hydrocarbon (MTH) reaction over new 8- and 10-ring acidic zeolites

60 study points

DEPARTMENT OF CHEMISTRY
Faculty of mathematics and natural sciences
UNIVERSITY OF OSLO 05/2009

Abstract

Developing a process in which natural gas, coal and biomass can be converted to valuable petrochemical products is becoming increasingly important. The methanol-to-hydrocarbon (MTH) reactions constitute the final step in one such route. The MTH reaction is catalyzed by acidic zeolites. ZSM-22 zeolite is a less studied catalyst for the MTH reaction and has unidirectional non-interacting channels of 4.6 x 5.7 Å dimensions.

In this work, ZSM-22 zeolite previously believed to be inactive catalyst in the methanol-to-hydrocarbon reaction is investigated as an active catalyst. Several ZSM-22 catalysts were synthesized, and all were found to be active catalysts for the MTH reaction. Low feed rates between 2.05 and 4.05 $gg^{-1}h^{-1}$ and temperatures 350-500 $^{\circ}C$ were used for the investigation. The methanol conversion capacity of ZSM-22 was found to be comparable to that of SAPO-34. The C_{5+} fraction was rich in branched alkenes (~70 %), very little C_2 and negligible amounts of aromatic hydrocarbons (~1 %) were formed. This product blend meets the requirements for a cleaner gasoline and might be used for the production of environmentally friendly gasoline by hydrogenation. Alternatively, the alkene rich product might be used as alkylation feedstock. The product spectrum of the ZSM-22 catalyzed MTH reaction is intermediate to those found in MTO and MTG, and this might provide product flexibility in an MTH application. Isotopic labeling studies revealed that the alkene methylation-cracking mechanism is the main reaction mechanism for the MTH reaction over ZSM-22 catalys. Alkali treatment of the material is found to be promising for improving its catalytic activity.

SUZ-4 zeolite that has 10-membered ring straight channels interconnected by zigzag 8-ring channels is synthesized. The 10-ring straight channels have dimensions 4.6 x 5.2 Å

Acknowledgment

I would first like to acknowledge the Norwegian quota scheme for accepting my application to study in Norway and for the financial support.

I would like to express my gratitude to my supervisors Professor Unni Olsbye, Associate Professor Stian Svelle, and Professor Karl-Petter Lillerud for giving me the chance to follow this project. Unni and Stian, thank you for your guidance, discussions and comments throughout my study.

My special thanks are given to Anette who helped me in TEM analyses, Stig Rune who helped me in FTIR analyses, Sissel and Per Olav for their help in Al-NMR.

I would like to take this opportunity to express my sincere thanks to colleagues and friends from the catalysis group for the very nice working environment. Melina, Francesca, Linn and Sharmala, thank you for helping me in the lab. Wegard, Ole, Marius and Bjørn T. thank you for the friendship and discussions. Special thanks to Marius for your comments regarding the writing of this thesis.

I want to thank my family for their encouragement and support during these years.

Table of Contents

1. INTRODUCTION

A catalyst is any substance that accelerates a chemical reaction. In order for a chemical reaction to occur, the reactant (reactants) must overcome an energy barrier. Figure 1.1 (left panel) displays a potential energy diagram for non-catalytic reactions. In Figure 1.1 (right panel), the potential energy diagrams for both catalytic and non-catalytic reactions are presented. For the non-catalytic path the reaction proceeds when the reactant molecules, A and B, collide with sufficient energy to overcome the energy barrier. The energy barrier for the catalytic path of a chemical reaction is significantly lower than the energy barrier for the non-catalytic path. Thus, a catalyst is any substance that accelerates the progress of a chemical reaction towards equilibrium, and allows the reaction to occur with low energy barrier [1].

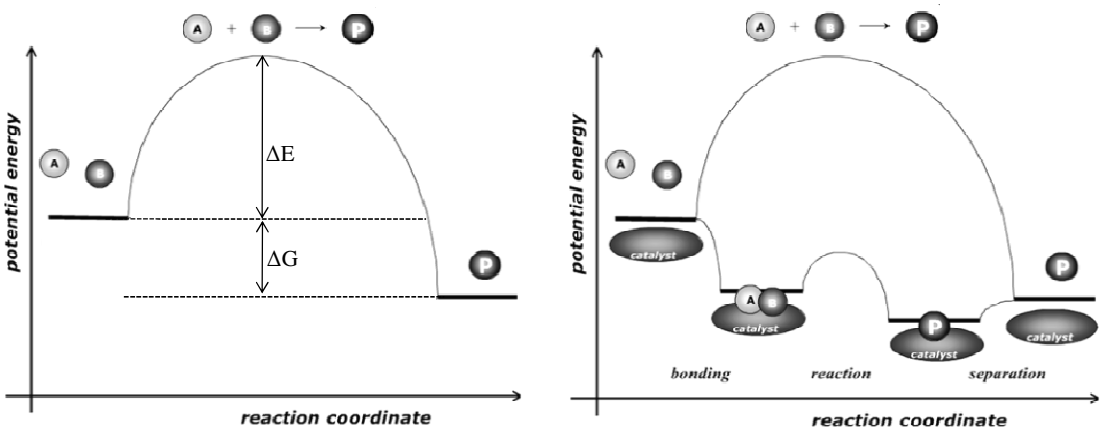

Figure 1.1: Potential energy diagram for non-catalytic path (left panel) and potential energy diagram for catalytic and non-catalytic paths (right panel)

The catalytic reaction starts by adsorbing of the reactants A and B to the catalyst, and they react to form the product while they are bound to the catalyst. Finally the product detaches from the catalyst. Here the catalyst offers an alternative more complex path for the reaction, but energetically more favorable. The free energy of the reaction is the same in both catalytic and non-catalytic paths.

Catalysis is divided in to three sub-disciplines: homogeneous, heterogeneous and biocatalysis or enzymatic catalysis. In homogeneous catalysis, the reactant, product and the catalyst are in one phase, usually in a liquid phase. In heterogeneous catalysis, the reactant, product and the catalyst are in different phases. Usually, the catalyst is a solid while the reactant and product are gases or liquids. The other sub-discipline, bio-catalysis, is based on natural catalysts called

Enzymes. Enzymes are proteins which are highly specific to certain substrate and they catalyze reactions efficiently.

1.1 Zeolites

Zeolites are three dimensional crystalline aluminosilicate minerals that can both be found in nature and synthesized in a laboratory.

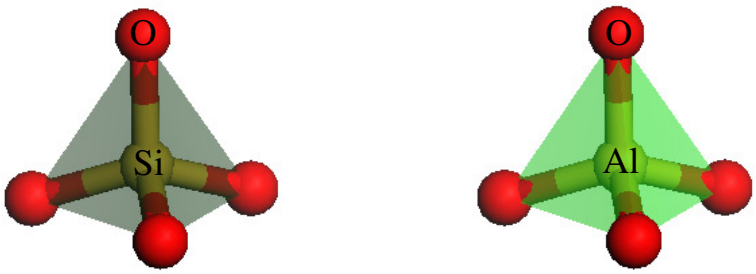

Figure 1.2: Tetrahedra of $[SiO_4]^{4-}$ (left panel) and $[AlO_4]^{5-}$ (right panel)

The three dimensional framework structures of zeolites arises from corner sharing of tetrahedra of $[SiO_4]^{4-}$ and $[AlO_4]^{5-}$, primary building units [2]. The primary building units are Si and Al atoms covalently bonded to four oxygen atoms, as displayed in Figure 1.2.

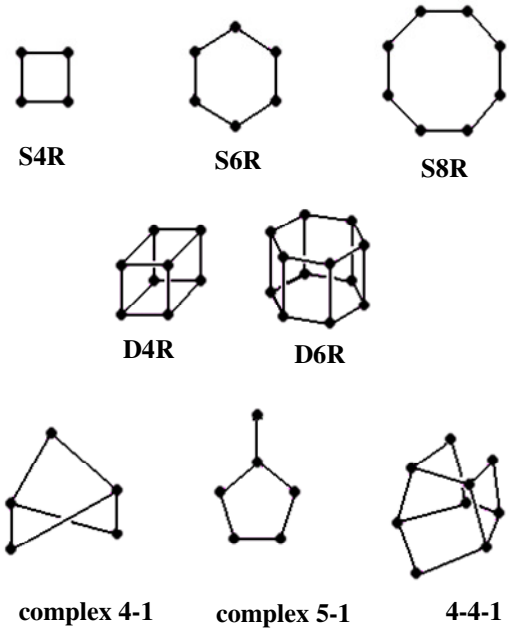

Figure 1.3 Examples of the secondary building units (SUBS) recognized in zeolite frameworks, adopted from [3].

The primary building units (TO_4-tetrahaedra) are linked together covalently by sharing an oxygen atom. This assembling will generate repeating structural sub-units called secondary building units (SBUS), which are characteristic of the structure (Figure 1.3). Combination of

the sbus will form the zeolite framework. A given zeolite structure can have one or more secondary building units.

The assembling of the SBUS in various manners makes the framework of zeolites contain cages (pores which are too narrow to be penetrated by guest species larger than water (Figure 1.4a)), cavities (pores that has at least one face defined by a ring large enough to be penetrated by a guest species, but which is not infinitely extended (Figure 1.4b)), and channels (pores that are infinitely extended in one dimension and are large enough to allow guest species to diffuse along its length (Figure 1.4c)) [4].

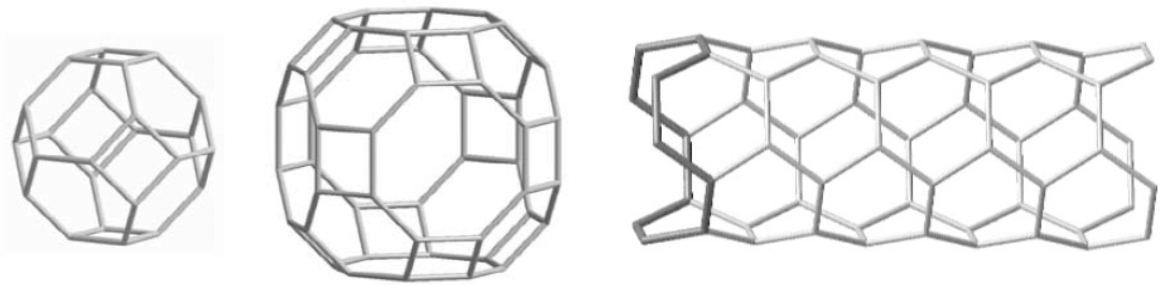

a) Sodalite cage b) α-cavity found in LTA c) 12-ring channel found in CAN

Figure 1.4: Examples of cage, cavity and channel in a zeolite: a) a sodalite cage (β-cage) found in zelite A (LTA), b) α-cavity found in zeolite A (LTA), and c)12-ring channel found in cancrinite (CAN), adopted from [4].

The pores are of molecular dimensions, and usually they contain removable template molecules, exchangeable cations and water. The molecular sieve property of zeolites is due to the cannels, cages and cavities within the framework.

Zeolites can be distinguished from denser silica based on their framework density (FD), the number of tetrahedrally coordinated atoms (T-atoms) per 1000 $Å^3$. For non-zeolitic framework structures, values of at least 20 to 21 T- atoms per 1000 $Å^3$ are generally obtained

while for zeolites the observed values range from about 12.1 T- atoms per 1000 $Å^3$ for structures with large pore volume to around 20.6 T- atoms per 1000 $Å^3$ for dense zeolites [2].

In zeolites the central atoms are Si and Al but, there are other zeolite like materials in which other central atoms are possible. SAPO (in which the central atoms are Si, Al, and P), AlPO4

(in which the central atoms are Al, and P),, MeAPO (in which the central atoms metal cation, Al, and P), and MeSAPO (in which the central atoms metal cation, Si, Al, and P)are known to exist.

1.2 Zeolite catalysis

Zeolites catalyze numerous reactions. By generating framework and/or extra framework active sites, zeolites can be used as acid, base, acid-base, redox and bifunctional catalysts [5]. The most of important application both for large scale industry and fine chemical being however are catalyzed by acid sites [6].

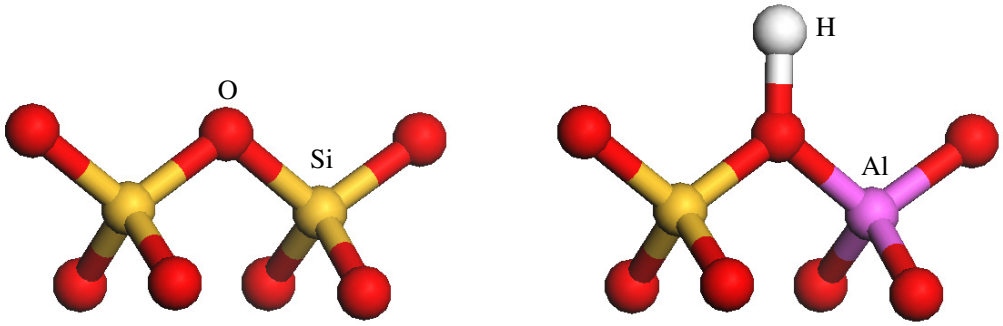

Figure 1.5: **Illustration of the connection of two $[SiO_4]^{4-}$ tetrahedra via oxygen bridge (left panel) and formation of acid site when replacing $[SiO_4]^{4-}$ with $[AlO_4]^{5-}$.**

Acid sites can be introduced in zeolites by isomorphous substitution of Si by Al in the framework. If the framework of a zeolite is constructed only from SiO_4 tetrahedra results in neutral framework, but replacing Si with Al give rise to a negative charge of the framework which must be balanced by non-framework cations. The cation can be metal ions or a proton. If the cation is a proton, an active site which can donate a proton is formed. Being a proton donor, the site is called a Brønsted acid. Figure 1.5 displays two tetrahedra of $[SiO_4]^{4-}$ connected via oxygen bridge (left panel) and tetrahedra of $[SiO_4]^{4-}$ and $[AlO_4]^{5-}$ connected via

oxygen bridge including hydrogen (acid site) attached for charge compensation (right panel). The acidity of proton exchanged zeolite corresponds to 80% H_2SO_4 [7].

Zeolite shape selectivity

Zeolites have pore dimensions of order of magnitude of molecular dimensions, giving rise to special shape selective of zeolites. Reactant, product and restricted transition state selectivities are observed in zeolite catalysis.

Reactant shape selectivity comes from the impossibility of certain molecules in a reactant mixture entering the zeolite pore. It is encountered when the size of the reactant is bigger than the size of the pore. Only reactants that are smaller than the pore opening can diffuse into the channels and cavities of the zeolite and can be converted over the active sites. Bulkier reactant molecules that cannot diffuse into the zeolites pores are excluded from reaching the active sites that are located inside the channels and cavities of the material and they will not be converted as illustrated in Figure 1.6a.

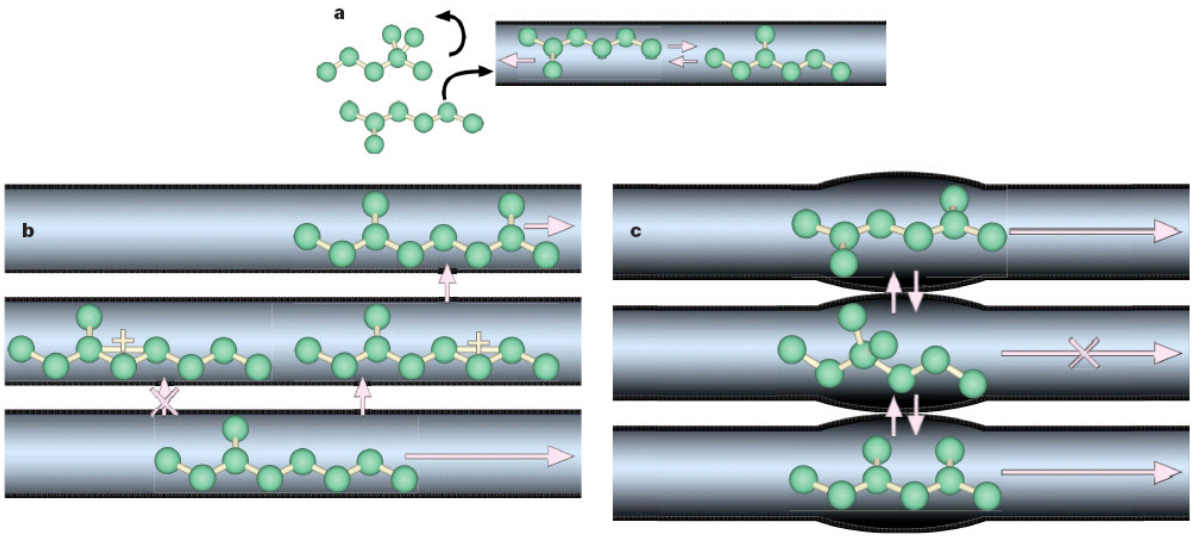

Figure 1.6: **Illustration of zeolite shape selectivity a) reactant selectivity, b) restricted transition state selectivity and c) product selectivity, adopted from [8].**

Restricted transition state selectivity some chemical reactions involve transition states which are too bulky to be accommodated inside the zeolite channels and cavities. The formation of bulky reaction intermediates is sterically hindered by the space around the active sites in the pores of the zeolite. As a consequence the overall reaction will not occur. Instead reactions

having intermediates that can fit into the pores of the catalysts will occur. This kind of selectivity is known as restricted transition state selectivity, illustrated in Figure 1.6b.

Product shape selectivity comes from impossibility of certain product molecules exiting from the zeolite pores. This may be viewed as the reverse of reactant shape selectivity. Some zeolite structures have cavities which allow formation of both small and bulky products. Molecules which are smaller than the oxygen window of the framework will diffuse out of the material, while the bulky product molecules undergo further reactions to smaller molecules to leave the cage or to form higher molecular species that retained in the cage of the zeolite. This

will eventually lead to catalyst deactivation by pore blockage. Product shape selectivity is illustrated in Figure 1.6c.

1.3 ZSM-22 (TON)

The framework of ZSM-22 is iso-structral with Theta-1, ISI-1, and NU-10. This framework type is known by the IUPAC three letter code TON. The framework of ZSM-22 is made up by 5-, 6-, and 10-membered rings of TO_4 tetrahedra and can be constructed from complex 5-1 secondary building units, and it has a framework density of 19.7 [2]. A projection of the structure parallel to [001] shows edge-sharing five-membered rings of TO_4 tetrahedra forming a zig-zag chain in the crystallographic ***a-****direction,* displayed in Figure 1.7 (emphasized in bold). These chains are linked through corner sharing of oxygen atoms in the crystallographic ***b-*** and ***c-****directions.* This kind of linkage gives rise to 10-membered channels parallel to [001]. There are two such 10-membered ring channels per unit cell, and they are slightly zigzag (Figure 1.8). These channels are slightly elliptical in cross-section, and have a diameters of 4.6 X 5.7Å [2, 9] which is remarkably smaller than the 10-membered ring channels of ZSM-5 (5.3 X 5.5 and 5.4 X 5.6Å) [10]. The 10-membered ring channels are not interconnected, and so they represent a one-dimensional channel system. There are no 4 rings in the framework.

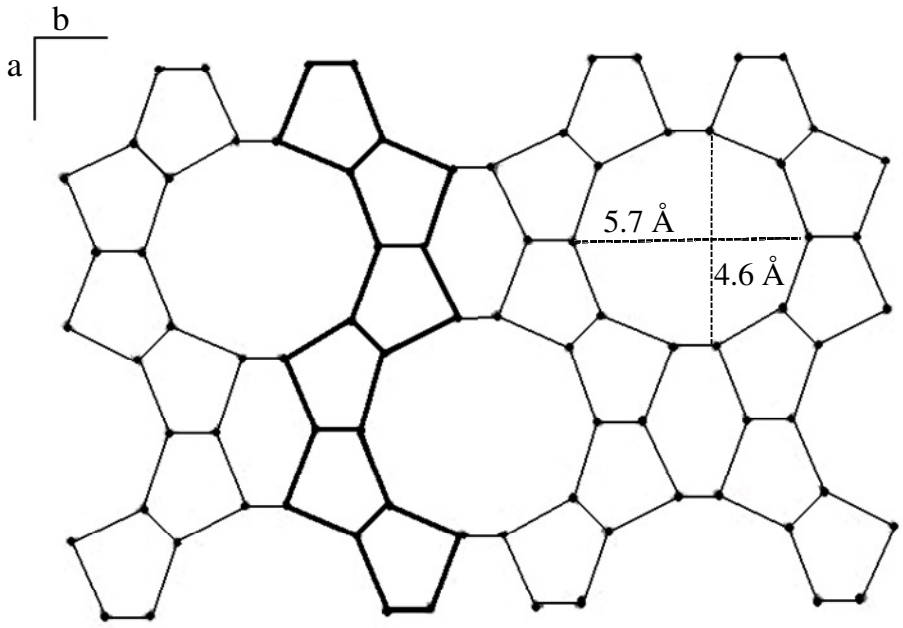

Figure 1.7: Projection of the silica-ZSM-22 framework along [001]. One chain of edge-sharing five-membered rings is emphasized in bold.

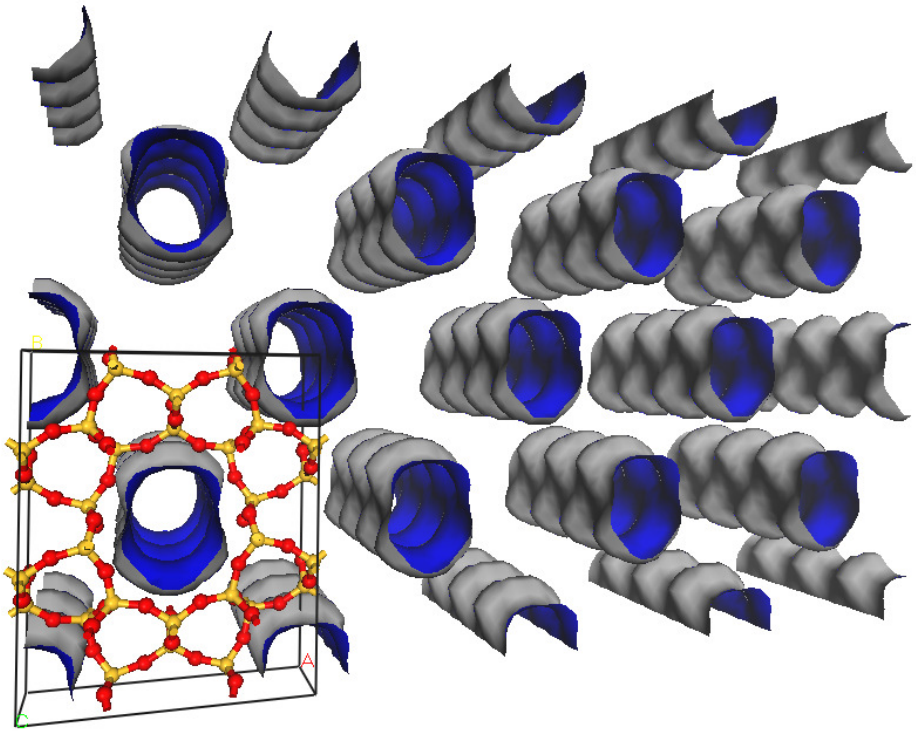

Figure 1.8: illustrations the slightly zigzag 10-ring channels of ZSM-22.

Kokotailo et al. determined the structure of ZSM-22 (Si/Al=74) from powder diffraction data [11] later Marler determined the structure of silica-ZSM-22 using single crystal refinement [9] the results are displayed in Table 1.1.

Table 1.1: Discription of ZSM-22 unit cell parameters as determined from powder diffraction data and single crystal diffraction data.

ZSM-22 unit cell	Determined form powder diffraction data [11]	Determined form single crystal diffraction data[9]
Symmetry	orthorhombic	orthorhombic
a	13.86 ± 0.03 Å	13.859(3)
b	17.41 ± 0.04 Å	17.420(4)
c	5.04 ± 0.02 Å	5.038(3)
$\alpha = \beta = \gamma$	90.0 °	90.0 °
Space group	Cmcm	Cmcm
Z	24	24

2. METHANOL-TO-HYDROCARBON (MTH)

Worldwide natural gas reserves have been increasing steadily over the last 10 years and are comparable in size to the reservoirs of crude oil [6, 12]. However, much of this gas is located in remote sites without access to pipeline and where transportation cost to get the gas to established markets are prohibitive. At the present time significant volumes of natural gas are used for the production of chemicals such as methanol, ammonia, hydrogen and others [12], natural gas is also used for heating purpose. On the other hand, every year oil producers flare and vent large volume of natural gas. This process of burning gas (flaring) or releasing it into the atmosphere (venting) harms the environment by adding to the greenhouse emission. According to WorldBank estimates, 110 billion cubic meters (bcm) of gas is flared and vented annually [13].

Developing a process in which natural gas, coal and biomass can be converted to valuable petrochemical products is becoming increasingly important. One of the promising processes for the economic utilization of natural gas is its indirect use for the production of petrochemicals via methanol [12], illustration of the process is presented in Figure 2.1

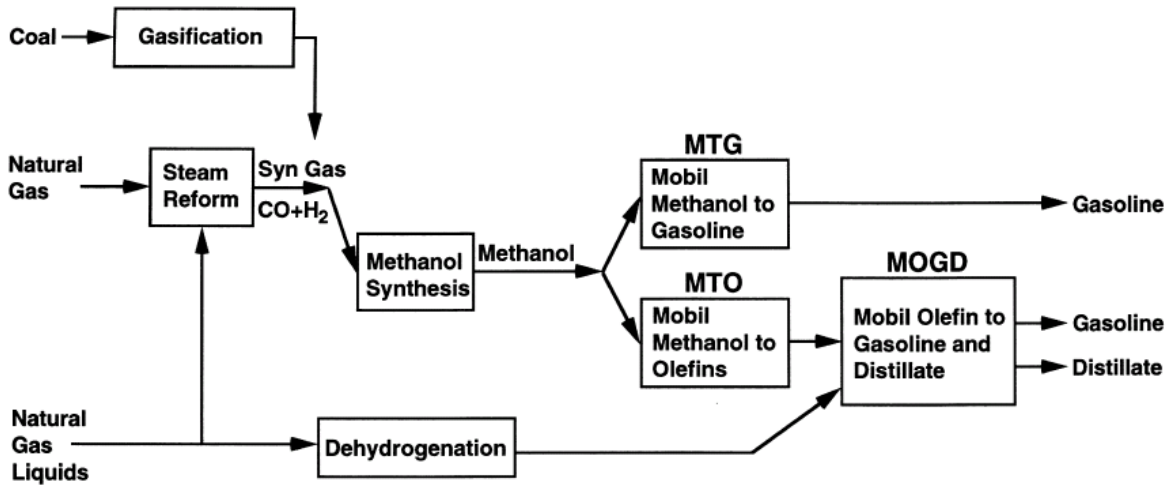

Figure 2.1: Gasoline and distillate production via methanol and Mobil's ZSM-5 technology [14]

Methanol can be produced from natural gas or any gasifiable carbonaceous material such as petroleum, coal or biomass. The production of synthesis gas (syngas) is the first step in large-scale production of methanol, which is formed by methane conversion over supported Ni

catalyst. Syngas is converted to methanol over $Cu/ZnO/Al_2O_3$ catalyst at about 50 atm and 250 °C [1]. The methanol-to-hydrocarbon (MTH) reaction constitutes the final step in one these routes of making valuable petrochemical products from natural gas, coal and biomass.

The MTH reaction proceeds over Brønsted-acidic zeolite or zeotype catalysts, and it was discovered by discovered by Mobil in the 1980s. The researches were trying to discover new ways to make high octane gasoline from methanol and isobutene using H-ZSM-5 [14]. They imagined that methanol would be added to isobutene to form highly branched alkenes. Instead they observed the conversion of methanol to various hydrocarbons.

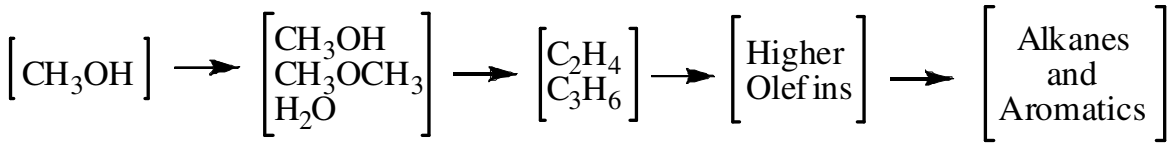

Scheme 2.1: Methanol to hydrocarbons, adopted from [15].

Scheme 2.1 displays the overall methanol conversion steps in the MTH reaction. The MTH reaction starts with equilibrium condensation of methanol to dimethyl ether and water. Then follows formation of light olefins which are the primary hydrocarbon products and mainly consists of ethene, propene and small amounts of C_4 olefins. In the next step of the reaction, the primary hydrocarbon products are oligomerized to form higher alkenes that may crack to an equilibrium distribution. Methylation of the primary hydrocarbon products may also occur to form the next higher alkene (example: propene to butene). Finally, complex reactions are occurring, including hybrid transfer that converts olefins to a mixture of alkanes and methylbenzenes, leading to accumulation of carbon rich hydrocarbons which will eventually deactivate the catalyst [15].

Depending on the catalyst used and process conditions, the product distribution of the MTH process can be varied.

Methanol-to-olefins (MTO) - in this process methanol is converted to light alkenes, mainly ehtene and propene. The MTO process is based on SAPO-34 catalyst where the narrow pores of the catalyst restricts diffusion of heavy and branched hydrocarbons. Bulky and branched

product molecules have to be cracked to diffuse out of the catalyst. The MTO technology has been demonstrated in a demo plant by Norsk hydro [16].

Methanol-to-gasoline (MTG) - in this process methanol is converted to gasoline range, C_5-C_{10} hydrocarbons. The MTG process is based on a ZSM-5 catalyst. The first MTG plant was built in New Zealand by Mobil, with a production of 10 000 barrels day^{-1}(about 30% of the country's need) of gasoline. Later as oil prices retreated the MTG section of the unit was shut down [15].

Methanol-to-propylene (MTP) - The process is also known as Lurgi. The Lurgi plant selectively converts methanol to propylene, with some byproduct gasoline and LPG type fuels. The reaction is based on ZSM-5 catalyst, and suitable reaction conditions are used for high selectivity for propene [17].

2.1 Reaction Mechanisms for the MTH reaction

Acid catalysis over zeotype materials is one of the most important and fundamental topics in catalysis. In addition to the MTH reactions, dimerisation, and C_4 isomerisation can be performed using acid catalysis by zeolites and/or SAPOs. Moreover, refinery processes like catalytic cracking, reforming, aromatisation and C_5-C_6 isomerization rely on zeolite based catalysts as well. However, there is no consensus on the mechanisms of most organic reactions in zeolites [15]. In the last 30 years more than 20 distinct mechanisms have been proposed for the MTH reaction over zeolite catalysts [14]. In the following section the MTH reaction mechanisms based on the current level of understanding are presented.

2.1.1 The hydrocarbon pool reaction mechanism

The overall methanol-to-hydrocarbon reaction can be written as

$$CH_3OH \rightarrow \text{“}CH_2\text{”} + H_2O$$

Where "CH_2": represents the hydrocarbon products. Several studies on the reaction mechanism for the MTH reaction were performed by co-feeding methanol with other hydrocarbons, some of these studies will be discussed in this section.

In 1983 Mole and co-workers studied the MTH reaction over ZSM-5 catalyst by co-feeding Toluene and methanol, and found that the reaction can be accelerated by the "cocatalytic"

effect of added Toluene [18, 19]. The results led Mole to speculate that the cocatalytic effect of Toluene resulted from alkylation of the methyl group on the aromatic ring leading to olefin elimination.

Few years later, in the mid-1990's, Dahl and Kolboe proposed the "hydrocarbon pool mechanism" for the methanol-to-hydrocarbon (MTH) reaction [20-22]. They carried out isotopic labeling experiments by co-feeding olefin precursors (ethanol) and ^{13}C-methanol over a SAPO-34 catalyst. Analysis of the composition of the product showed that ^{12}C was scrambled among the products and only small portion of the products contained ^{12}C. The hydrocarbon pool mechanism brought a major breakthrough in the fundamental understanding of acid catalysed reactions in zeolites and related catalysts. According to the mechanism, the first olefins in the MTH reaction are formed from a "hydrocarbon pool", organic species contained within the pore of the catalyst, as illustrated by Figure 2.2. Since then, a parallel effort by various groups studying the MTH reaction over different zeotype system has come to a unified view on the hydrocarbon pool mechanism.

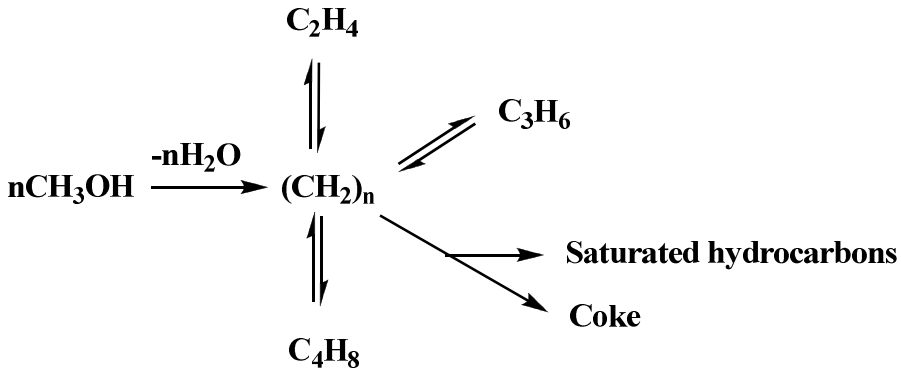

Figure 2.2 Kolboe's hydrocarbon pool mechanism, adopted from [22]

Studies over different catalysts have reported that polymethylbenzenes are the major hydrocarbon pool species [23-31].

The exocyclic methylation route and the paring reaction were reported as possible routes for the formation of initial olefins [12]. The exocyclic methylation cycle, originally proposed by Mole, [18, 19] starts with deprotonation of heptamethylbenzanium ion to HMMC (1,2,3,3,4,5-hexamethyl-6-methylene-cyclohexadiene). The presence of heptamethylbenzanium ion inside zeolite H-Beta has been reported previously [28, 29]. The exocyclic double bond on the HMMC is methylated to form an ethyl group, which is eliminated as ethene, or the ethyl group is further methylated to from an isopropyl group and it will detach form the ring as propene as illustrated in Scheme 2.2

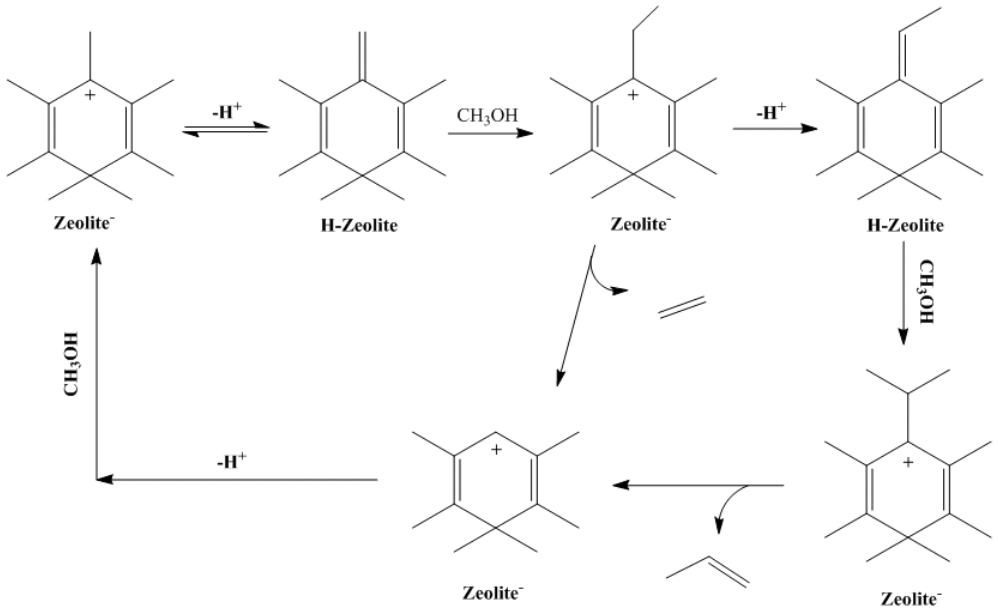

Scheme 2.2: The exocyclic methylation cycle. Adopted from [12]

The paring reaction mechanism was first proposed by Sullivan et al. in 1961[32], illustrated in Scheme 2.3**.** The complete cycle of this mechanism involves contraction of aromatic ring to a 5-ring intermediate followed by expansion of the 5-ring back to 6-ring aromatics. This contraction and expansion of the ring leads to extending of the alkyl chain from the ring, and a carbon atom interchange between the ring and the methyl-substituent. The paring reaction mechanism favors the formation of propene and isobutene.

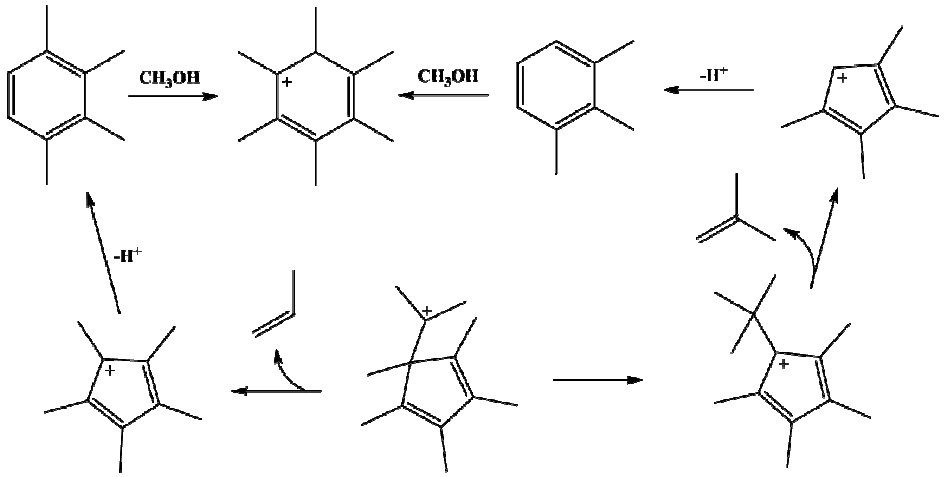

Scheme 2.3: The paring reaction cycle. Adopted from [12]

2.1.2 The Olefin methylation-cracking mechanism

Dessau and co-workers proposed the olefin methylation-cracking pathway as a main reaction mechanism for the MTH reaction during the 1980s [33, 34]. According to this mechanism, the initial olefins are formed from reactions involving $C_1 + C_1$ bond formation, once olefins are formed, the reactions leading to the initial olefin formation is irrelevant [33]. Only methylation of those olefins to the next higher alkene (illustrated in example: propene to butane) is responsible for the MTH reaction. Methylation of the light olefins can occur more than once, leading to formation of higher alkenes which in turn undergo cracking reactions.

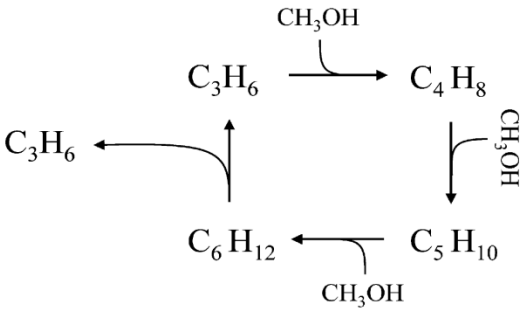

Scheme 2.4 illustration for propene formation via alkene methylation-cracking mechanim, adopted from [35].

Svelle et al. studied the kinetics of methylation reactions over the ZSM-5 catalyst [36, 37], and reported that the olefin methylation-cracking reaction mechanism is taking place in parallel to the hydrocarbon reaction mechanism. Extremely high feed rate ~300 $gg^{-1}h^{-1}$ was used for the investigation to suppress hydrocarbon pool reactions.

Later, Svelle et al. [38] and Bjørgen et al. [35] performed isotopic labeling studies over ZSM-5 catalysts, and observed that the ^{13}C content in ethene is different from higher alkenes, and it is similar with the ^{13}C content in retained hydrocarbons especially with lower methylbenezenes. Based on this finding it was reported that ethene formation is mechanistically separated from the formation of higher alkenes, and two mechanistic cycles run simultaneously during the methanol-to-hydrocarbon reaction over a ZSM-5 catalyst, the hydrocarbon pool and the methylation-cracking cycle.

2.2 ZSM-22 as MTH catalyst

ZSM-22 is a less studied catalyst for the MTH reaction. Cui et al. [39-41] and Li et al. [42] have studied the MTH reaction over the catalyst and reported its failure to convert methanol to hydrocarbons [39-41]. Cui et al. compared the activity of ZSM-22 catalyst with other selected zeolite structures [39]. The selection of the zeolites was based on the maximum diameter of a sphere that could be included in the framework (Figure 2.3).

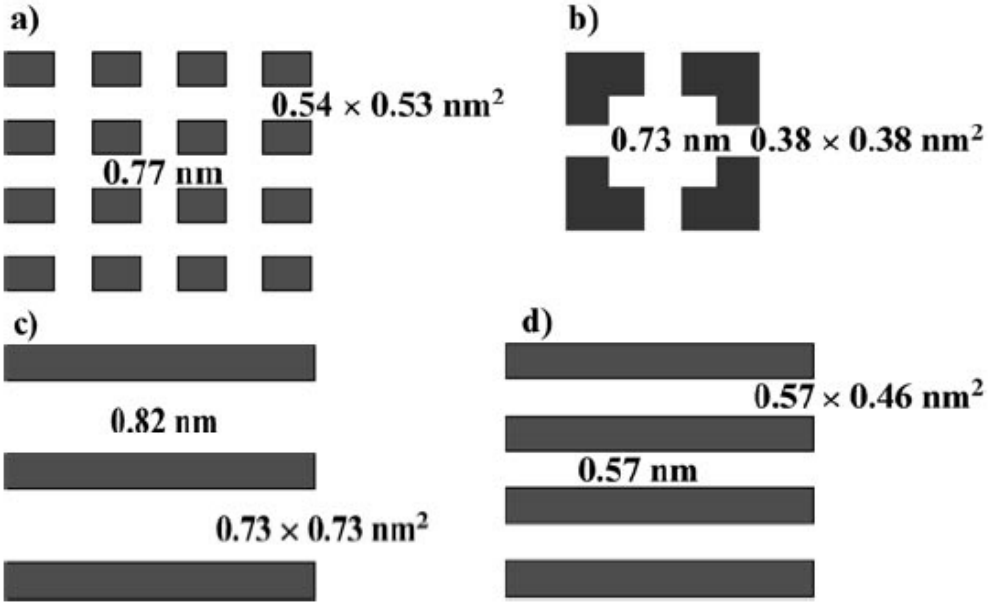

Figure 2.3: **Illustration of zeolite pore structures, adopted from [39] a) MEL structure of ZSM-11, b) CHA structure of SAPO-34, c) AFI structure of SAPO-5 and d) TON structure of ZSM-22. The values inside the pores indicate the maximum diameter of a sphere that can be included in the framework, and those outside the pores indicate the size of the pore openings.**

ZSM-11 (MEL) has a three dimensional pore structure enclosed by 10 oxygen windows. The 10 ring straight channels intersect in the framework giving rise to a free space ~0.77nm at the channel intersection. SAPO-34 (CHA) contains large cavities which are separated by an

aperture of eight oxygen window. The free space of the cavity is ~0.73nm. SAPO-5 (AFI) contains non-interacting unidirectional 12 ring channels with a free diameter of ~0.82nm. ZSM-22 (TON) – contains non-interacting unidirectional 10 ring channels with a free diameter of ~0.57nm.

According to their report all the catalysts, except ZSM-22, converted methanol to hydrocarbons. ZSM-22 with ZSM-11 impurities showed a low production of light olefins during the first few pulses of methanol, however the amount of olefin quickly decreased to essentially zero and dimethyl ether was the only major product. The failure of ZSM-22 as

MTO catalyst was ascribed to its narrow pores (0.57nm), which were assumed to be too narrow to complete the catalytic cycle of space demanding hydrocarbon pool mechanism. Flow type experiments (WHSV = 48 $gg^{-1}h^{-1}$) showed a relatively constant yield of trace amounts of olefins (ethene and propene) in a temperature range of 250 to 400 °C. The low reactivity was believed to be as a result of impurities of ZSM-11, impurities in the methanol (99.5% with acetone as a major compound) and/or external acid sites.

Li et al. to study the co-reaction of ethene and methylation agents over ZSM-22 catalyst [42]. They observed appreciable conversion of methanol (96 %) in the first few minutes on stream (WHSV = 10 $g^{-1}g^{-1}h^{-1}$), but the catalyst deactivated quickly and ~1.5% conversion was observed after 60 minutes on stream.

Both Cue et al. and Li et al. paid no attention to the conversion of methanol in the first few minutes on stream. An extensive study of the MTH reaction over ZSM-22 was not conducted. Thus, this master project was focused on further investigation of methanol to hydrocarbon reaction over ZSM-22 catalyst at a wider reaction conditions.

3. SYNTHESIS AND POST SYNTHESIS TREATMENT OF ZSM-22

In this section the synthesis and various post synthesis treatments of the ZSM-22 catalysts are presented.

3.1 Synthesis of ZSM-22

ZSM-22 catalysts were synthesized under hydrothermal conditions following the procedures in references [43-45]. Three different organic templates were used. A list of reagents used in the synthesis of ZSM-22 catalyst is presented in Appendix-1.

Synthesis using 1-ethylpyridinium bromide as structure directing agent

A ZSM-22 catalyst was synthesized using 1-ethylpyridinium bromide ($C_7H_{10}BrN$) as structure directing agent following the procedure in reference [44]. Two solutions were prepared,

i. 0.169 g of $Al_2(SO_4)_3.16H_2O$ and 1.0 g of $C_7H_{10}BrN$ were dissolved in 12.5 g of water
ii. 6.25 g water glass (35 wt%) was dissolved in 5 g of water

Solution i was added to solution ii while stirring. To the resulting gel 0.313 g H_2SO_4 was added under vigorous stirring. The gel was transferred into 40 ml Teflon lined stainless steel autoclaves and crystallization was carried out at 160 °C for 4 days without stirring. After complete crystallization, the reaction mixture was diluted with distilled water and the product was recovered by filtration, washed and dried overnight at 90 °C.

Synthesis using diethylamine as structure directing agent

A ZSM-22 catalyst was synthesized using diethylamine (DEA, $C_4H_{11}N$) as structural directing agent following the procedure in reference [43]. Three solutions were prepared,

i. 0.63 g of $Al_2(SO_4)_3.16H_2O$ and 1.65 g H_2SO_4 were dissolved in 17.6 g water
ii. 17.0 g of water glass and 0.11g NaOH were dissolved in 22.35 g water
iii. 1.65 g 50% H_2SO_4

Solution ii was added to solution i and the gel was homogenized. Subsequently solution iii and 3.4 g diethylamine (DEA) was added. After homogenization, the gel was transferred into a 40 ml Teflon lined stainless steel autoclaves and crystallization was carried out at 170 °C for 2 days in a vertically rotating oven (25 rpm). Teflon coated bar magnets were used to enhance the gel mixing. After crystallization was complete, the reaction mixture was diluted with distilled water and the product was recovered by filtration. The resulting product was washed and dried overnight at 90 °C.

Synthesis using 1, 8-diaminoocatane as structure directing agent

A ZSM-22 catalyst was synthesized using 1, 8-diaminooctane as structure directing agent following the procedure in reference [45]. Four solutions were prepared,

i. 1.05 g $Al_2(SO_4)_3.16H_2O$ was dissolved in 10.89 g water
ii. 2.39 g KOH was dissolved in 10.89 g water
iii. 6.23 g $C_8H_{20}N_2$ was dissolved in 43.6 g water
iv. 28.50 g LUDOX AS-30 was dissolved in 16.14 g water

Solution ii was added to solution i under stirring. To the resulting mixture, solution iii was added. Finally to the mixture of the three solutions, solution iv was added under vigorous stirring. The final mixture was stirred for 30 min. The batch composition of the synthesis mixture was 8.9 K_2O : Al_2O_3 : 90 SiO_2 : 3 K_2SO_4 : 27.3 DAO : 3588 H_2O, note that the synthesis gel has Si/Al = 45l. After 24 hours ageing time at room temperature, the gel was transferred to 40 ml Teflon lined stainless steel autoclaves. The Si/Al ratio was varied by changing the amount of $Al_2(SO_4)_3.16H_2O$ in the gel. Different crystallization times and different ovens were used during crystallization (see Section 6.1.1 and Appendix 3). After crystallization was complete, the reaction mixture was diluted with distilled water and the product was recovered by filtration. The resulting product was washed and dried overnight at 90 °C.

3.2 Calcination and Ion-exchange

The template was removed by calcination under a flow of pure oxygen at 550 °C for 12 hours. The temperature of the oven was increased step wise , ~100 °C at a time up to 400 °C and ~50 °C at a time above 400 °C (hold time = ~30 min between each increase in temperature). The calcined samples were ion exchanged 3 x 2 hours with 1M NH_4NO_3 in a 70 °C water bath. The ion exchanged catalysts were calcined at 550 °C for 2 hours in static air, for 1 hour *ex situ* in a flow of pure oxygen, and for 1 hour *in situ* in the fixed bed reactor in a flow of pure oxygen prior to each catalytic experiment to desorb ammonia.

3.3 Post synthesis treatment (desilication) of ZSM-22

The confined micropores of zeolites imposes limits on their application as catalysts, due to diffusion limitation of reactants and products, this may result in accessibility of only part of the crystal for reactions [46, 47]. One approach to improve the diffusion properties of zeolites is to selectively remove Si atoms from the framework as illustrated in Scheme 3.1, as a result of this mesopores may be created in the crystals.

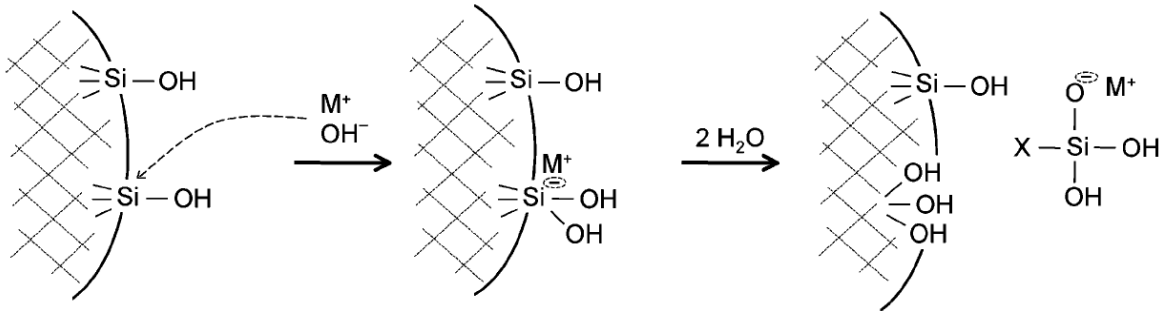

Scheme 3.1 illustrations of Si removal from a zeolite framework in the presence of alkali solution, M+ metal cation, adopted from [47].

Recently, Bjørgen et al. [46] have reported the formation of mesopores upon NaOH treatment of ZSM-5, giving rise to improved catalytic activity for the MTH reaction. Desilication of zeolite beta using tetramethylammonium hydroxide (TMAOH) was reported without loss of crystallinity of the material [48].

In the following section the various post synthesis treatments performed on ZSM-22 catalysts using NaOH and TMAOH are presented.

Post synthesis treatment was performed on two batches of catalysts in alkali media. Two different ZSM-22 catalyst bathes were subjected to post synthesis treatment, hereafter denoted as PARENT-1 and PARENT-2. The difference between PARENT-1 and PARENT-2 catalysts is presented in Section 6.5. The treatment conditions for the two batches of catalysts are displayed in Table 3.1 and Table 3.2.

Prior to the post synthesis treatment, the catalyst were calcined as described in Secion 3.2. The treatments of PARENT-1 catalyst were performed without desorbing ammonia after the ion exchange process. For PARENT-2 catalyst, most of the treatments were performed after desorbing ammonia. PARENR-2-1 (see Table 3.2) was treated in identical condition as that of PARENT-1-0.2M (see Table 3.1) without desorbing ammonia.

All the desilication experiments were performed using constant liquid-to-solid ratio (alkali reagent-to-ZSM-22 catalyst) of 30 ml per gram of zeolite. The pH of the solution was measured at different times during the treatment. After the treatment was over the catalysts were recovered by filtration and washed with distilled water. The treated and washed catalyst samples were dried overnight in an oven at 60 °C. The mass of the catalysts before and after the treatment was measured and the weight loss during the treatment was calculated. The dried catalysts, except the catalysts treated with tetramethylammonium hydroxide (TMAOH), were ion exchanged 3 x 2 hours with 1M NH_4NO_3 and then calcined at 550 °C to desorb ammonia as described in Section 3.2.

Table 3.1: post synthesis treatment conditions for PARENT-1 catalyst

Sample	Treated with	T °C	Stirring	Time
PARENT-1	-			
PARENT-1-0.05M	1.5 mmol NaOH /g catalyst	75	No	30 min
PARENT-1-0.2M	6 mmol NaOH /g catalyst	75	No	30 min
PARENT-1-0.5M	15 mmol NaOH /g catalyst	75	No	30 min

Table 3.2: post synthesis treatment conditions for PARENT-2 catalyst

Sample	Treated with	T °C	Stirring	Time
PARENT-2	-	-	-	-
PARENT-2-1	6 mmol/g NaOH/ g catalyst	75	No	30 min
PARENT-2-2*	6 mmol/g NaOH/ g (x4) catalyst	75	No	30 min x 4
PARENT-2-3	6 mmol/g NaOH/ g catalyst	85	No	30 min
PARENT-2-4	6 mmol/g NaOH/ g catalyst	85	Yes	30 min
PARENT-2-5	6 mmol/g NaOH/ g catalyst	100	Yes	30 min
PARENT-2-6	15 mmol/g NaOH/ g catalyst	85	Yes	30 min
PARENT-2-7	6 mmol/g TMAOH/ g catalyst	75	No	30 min
PARENT-2-8**	6 mmol/g NaOH/ g in 1 M NaCl	75	No	120 min

* = the 30 minutes treatment was repeated 4 times with filtration and washing in between

** = NaOH was dissolved in 1M NaCl solution

TMAOH = tetramethylaluminium hydroxid

For zeolite samples treated under stirring conditions a stirring speed of 400 rpm was used.

4. CHARACTERIZATION OF ZSM-22

ZSM-22 catalysts were characterized using powder X-Ray Diffraction (XRD), Scanning Electron Microscopy (SEM), Inductively Coupled Plasma Atomic Emission Spectroscopy (ICP-AES), BET-measurement (BET), Aluminum Nuclear Magnetic Resonance Spectroscopy (^{27}Al-NMR), Infrared Spectroscopy (FTIR), Transmission Electron Microscope (TEM), Temperature Programmed Desorption (TPD), and Thermogravimetric analysis (TGA). In the following chapter, background for the characterization techniques and the experimental part is presented.

4.1 Powder X-ray Diffraction (XRD)

Background

The regular arrays of atoms in a crystal lattice interact elastically with radiations of sufficiently short wavelength, to yield a diffraction spectrum in which the radiation is scattered out of the incident beam [49], shown in Figure 4.1. Both the diffraction angle and the intensities in the various diffracted beams are sensitive function of crystal structure.

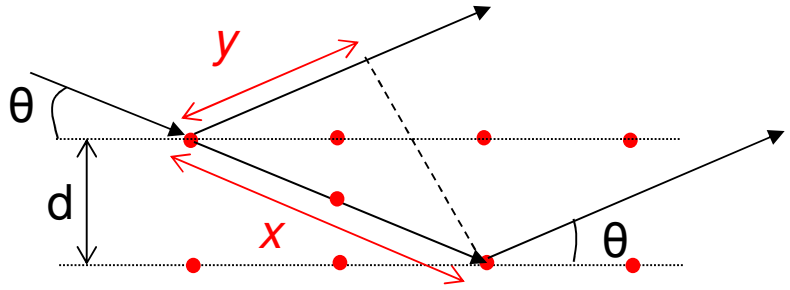

Figure 4.1: Illustration of scattering of radiation from regular arrays of atoms in a crystal, adopted from [49].

Diffraction of various radiations from different crystal plans causes a path difference among the radiations, which will lead to either constructive or destructive interference of a diffracted beam. If the path difference is equal to whole number of the wavelength then Bragg's law is satisfied. Bragg's equation gives the relationship between position of the peak (2θ) and d-spacing of diffracting planes, and is given by:

$$2d \sin\theta = n\lambda \qquad (4.1)$$

Were d is interplanar spacing, n is a positive integer, $2dsin\theta$ is the path difference of the incident radiations, and λ is the wave length of the radiation. The d-spacing is related to unit cell parameters, this means that the position of each peak in a diffraction pattern depends on the unit cell parameters of a crystal, and it is a finger print for a given structure.

In addition to information about the unit cell which can be obtained for the position of a peak, intensities and the Full Width at Half Maximum (FWHM) of the peaks in a diffraction pattern are a source of information. Scherrer equation relates peak broadening with crystal size, and after correcting for instrumental contribution, it can be used for a quick estimation of crystal size [50].

$$L = \frac{k\lambda}{\beta \cos\theta} \tag{4.2}$$

Where β is the full width at half maximum (in radians), k is a constant (approx. 1.0), λ is the wavelength, L is the length of the crystal perpendicular to the lattice plane responsible for the reflection at the Bragg angle θ.

The observed intensities in a diffraction pattern are determined by atoms in a unit cell and their position. The intensities are proportional to the square of the structural factor (F_{hkl}), which includes the effect of the atomic scattering factor for all of the atoms present in the material.

$$F_{hkl} = \sum_{1}^{N} f_n \exp[2\pi i(hu_n + kv_n + lw_n)] \tag{4.3}$$

Where F_{hkl} is the structural factor, f_n is the atomic scattering factor, and the exponential term is functions of the phase difference for radiations scattered by atoms. There are other physical factors which determine intensities in a diffraction pattern and they are summarized in Equation 4.4.

$$I = k|F^2| \frac{1 + \cos^2 2\alpha \cos^2 2\theta}{\sin^2\theta \cos\theta \,(1 + \cos^2 2\alpha)} \cdot P \cdot A(\theta) \cdot \exp\left(-2\frac{B \sin^2\theta}{\lambda}\right) \tag{4.4}$$

Where *I*: is observed intensity, *k* is a scaling factor, *and* *F* is the structural factor. The exponential term is a temperature factor which is related to random atomic vibrations at high temperature, *A(θ)* is absorption factor, *P* is the multiplicity of reflecting plane (number of planes belonging to a particular family of Miller indices), and the rest of terms in the equation correspond to sampling geometry. This equation can be used to calculate simulated integrated intensities for any given structure by using an appropriate computer program [49].

Experimental

The phases purity and crystallinity of the products were identified using X- ray diffraction on a Siemens D-5000 diffractometer with Bragg-Brentano geometry, position sensitive detector and CuKα1 radiation (λ= 1.5406 Å). XRD data were analyzed using EVA 8.0, developed by SOCABIM. The diffraction pattern was compared with the data in the powder diffraction file (PDF) database compiled and revised by Joint Committee on Powder Diffraction Standards International Centre.

4.2 Scanning Electron Microscope (SEM)

Background

Scanning electron microscopy is one of the techniques used to observe samples in a wide range of magnified scales, about x10 to x10^6 [51]. When an electron beam is irradiated on a sample surface, both elastic and inelastic interaction occurs, leading to emission of valuable information. The principle of magnification in SEM is displayed in Figure 4.2. The emitted information is converted into an electric signal, amplified, and then fed into an observation cathode ray tube (CRT), where it is displayed as a magnified image.

A portion of the incident electrons will be back-scatted from the specimen surface (elastic interaction). The amount of back-scattered electrons will depend on the average atomic number of the specimen. Most features detected in the image generated by back-scattered electrons are due to atomic-number contrast and reflect variation in density (composition of the specimen) [49].

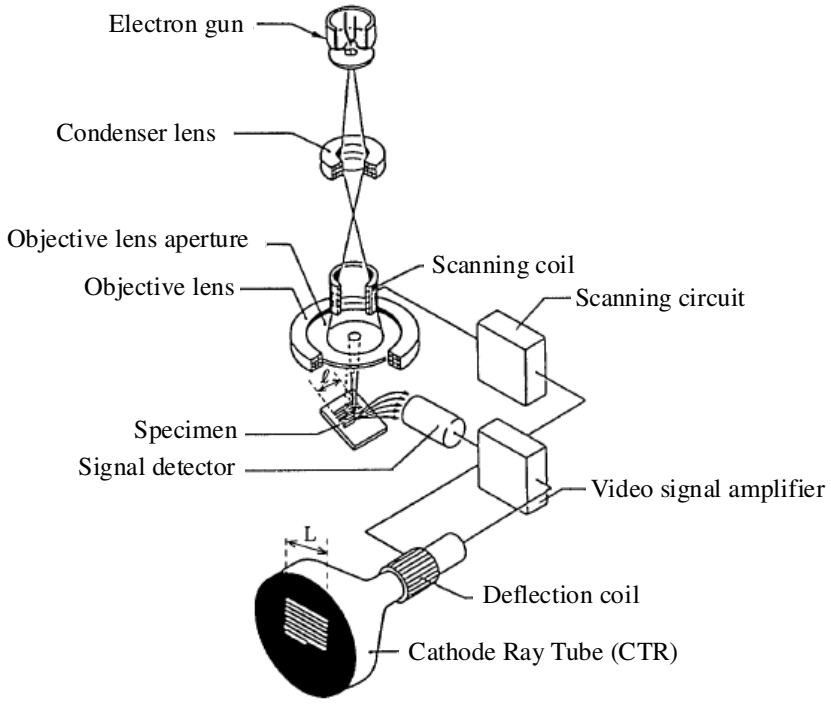

Figure 4.2 Principle underlying the scanning electron microscope SEM, adopted from [51]

At sufficiently high energy of the incident beam, secondary electrons can be ejected from the outer surface of the specimen. The emission of secondary electrons depends on the beam energy and intensity, work function of the surface, density of the specimen, and the surface topology of the specimen. The most pronounced effect arises from the surface topology of the specimen. Thus, the resolution and contrast of secondary electron image is mostly affected by the surface topology of the specimen, protruding regions from the surface will improve emission of secondaries, while recessed regions will emit reduced amounts of scondaries [49]. Thus, the secondary electrons are a source of images at high resolution and good contrast of surface topologies. If secondary electrons are ejected from the inner shells of an atom, transition of electrons from the outer shell to the inner shell will occur. These kinds of transitions emit photons having energies in the X-ray region of the spectrum. The X-ray spectrum generated is a fingerprint for a given element in a sample, and can be used to investigate the chemical composition of a sample both qualitatively and quantitatively.

Experimental

The crystal size and shape were investigated using Scanning Electron Microscopy. ZSM-22 crystals were sprinkled on a carbon tape mounted on a copper grid. Mostly low acceleration voltage (5-10 kV) and spot size 3 were used for imaging. Energy-Dispersive X-ray (EDS) analyses were performed to investigate the elemental composition and purity of the synthesis products. The analysis was performed on a Quanta 200 F (FEI).

4.3 Transmission Electron Microscope (TEM)

Background

Transmission electron microscope (TEM) is one of the tools used to investigate the structure of materials down to sub-nano level. It enables the examinations of specimen which are sufficiently thin to allow transmission of electron beam through them. In TEM, high energy electrons are elastically scattered as they penetrate a thin specimen. The transmitted electrons are then focused by electromagnetic lenses to form an image which can be viewed on a fluorescent screen.

Figure 4.3 displays the underlying principle in TEM. The high energy electrons are focused on the specimen by an electromagnetic lens system, whose focus is adjusted by controlling the lens current [49]. The intermediate lens and projector lens are used as a final imaging system, and the final image is observed on a fluorescent screen.

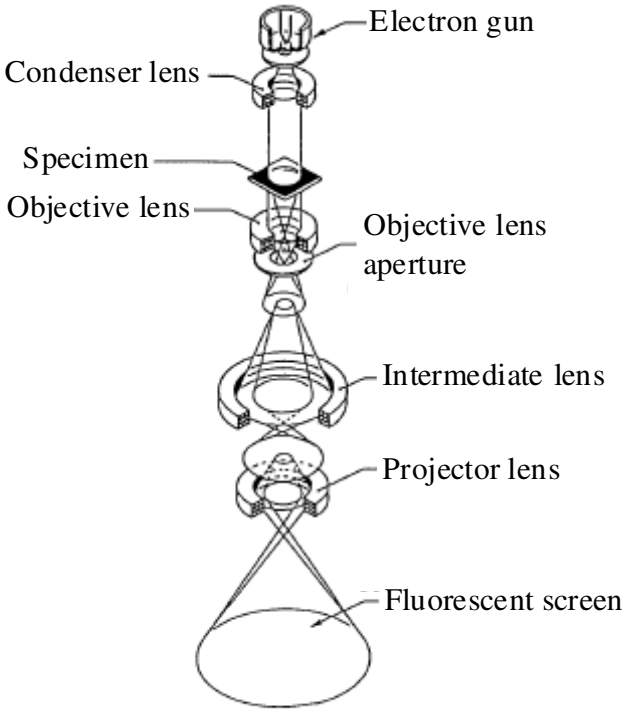

Figure 4.3 Principle underlying the Transmission electron microscope TEM, adopted from[51]

In order to avoid inelastic scattering of the transmitted beam, the sample thickness must be less than 100 nm [49]. This means that careful sample preparation is critical. For better transmission high electron energy is needed. Most instruments have acceleration voltages ranging between 100 – 400 keV. To avoid scattering of the electrons residual gas in the column, the whole microscope column is under vacuum, which should be better than 10^{-6} torr [49].

In a crystalline sample, the electrons are scattered according to Bragg's law, giving rise to a selected-area diffraction pattern. The electron selected area diffraction pattern includes several lattice points surrounding the 000 spot (corresponding to the directly transmitted beam). The length of a vector *R* from the 000 spot to a given lattice point is related to the d-spacing of the reflection and the wave length of the electron beam λ by the following relation

$$R = \frac{\lambda L}{d} \tag{4.5}$$

Where *L* is the effective camera length. This means that from the length of the vectors in a given selected-area electron diffraction, the d-value and other unit cell parameters for a crystalline sample can be calculated.

Experimental

ZSM-22 catalyst was suspended in ethanol, and a drop of the mixture was spread and dried on porous carbon film sample cell. The dried specimens were analyzed using JEOL 2010F electron microscope, the experiments were performed at 200 keV.

4.4 Inductively Coupled plasma Atomic Emission Spectroscopy (ICP-AES)

Background

Atomic spectroscopy is a commonly used technique for trace concentration determination of an element in a given sample.

When an atom in its ground state absorbs energy, either excitation or ionization occurs. In order for an ionization to occur, the absorbed energy should be sufficient to eject an electron from the atom. Atoms are less stable in their exited state and will thus decay back to the ground state through thermal or radiation (emission) energy transitions. Ions also have ground and exited state and they can absorb and emit energy as atoms. Every element has its own unique set of absorption and emission wavelengths, meaning that a given electromagnetic spectrum generated by absorption and emission of energy is a fingerprint of a specific element.

In inductively coupled plasma atomic emission spectroscopy (ICP-AES), samples under investigation are subjected to high temperature which is sufficient to dissociate the sample into its constituent atoms, and cause excitation and ionization of the atoms. Once the atoms and the ions are in their exited state, they decay to the ground state through emission of light. The intensities of the emitted light at specific wavelengths are measured and used to determine the concentration of the elements of interest [52].

Experimental

40 mg of ZSM-22 catalysts were dissolved in 2 ml 15% HF, and diluted to 50 ml using distilled water. Standard solutions containing Si and Al in a wide range of known concentrations were prepared from commercially available stock solutions of the elements. The matrix mixture of the standard solutions and the zeolite sample were identical. All the solutions (standards and zeolites) were analyzed using a Varian VISTA PRO CCD simulant ICP-AES instrument.

4.5 BET measurement

Background

Nitrogen adsorption at boiling temperature (77k) represents the most widely used technique to determine catalyst surface area and to characterize its porous texture. The technique is developed by Brunauer Emmett and Teller, and BET stands for the first letter of their names.

Starting point is the determination of the adsorption isotherm, which is a plot of the amount of gas adsorbed at equilibrium as a function of the partial pressure P/P_o, at constant temperature. The surface area is calculated from the volume of a gas needed to form a complete monolayer. The volume the gas needed for monolayer coverage is calculated from BET equation [53], given by

$$\frac{P}{V_a(P_o - P)} = \frac{1}{CV_o} + \frac{C-1}{CV_o} \cdot \frac{P}{P_o} \tag{4.6}$$

Where C: BET constant V_a: volume adsorbed V_o: monolayer adsorbed volume P_o: standard pressure and P: saturation pressure. Once the volume of monolayer coverage is calculated, it is converted to number of molecules by

$$N_o = \frac{PV_o}{RT} \tag{4.7}$$

The surface area is the product of the number of molecules needed for monolayer adsorption (N_o) and the area occupied by one molecule, for example N_2 occupies 0.162 nm^2 [1].

Experimental

The surface area of ZSM-22 catalysts was determined by nitrogen adsorption at a temperature of 77 k. About 60 mg of the catalysts were pretreated for 5 hours prior to the surface area measurements. The pretreatment was carried out by outgassing the catalysts at 80 °C for 1 hour followed by 4 hours at 300 °C. BET surface area measurements were performed using a BELSORP-mini II instrument.

4.6 Aluminum Nuclear Magnetic Resonance Spectroscopy (^{27}Al-NMR)

Background

The rotation of asymmetric nuclei required to produce nuclear magnetic resonances at specific 'magic' angel gives information as to the nearest coordination neighbors of the assumption nucleus [3].

In zeolites, ^{27}Al-NMR is used to elucidate the local environment of ^{27}Al in the structure. ^{27}Al spectra gives a clear difference between Al tetrahedrally and octahedrally coordinated to oxygen atoms. Al atoms which are tetrahedrally coordinated to oxygen are in the framework, while Al atoms which are octahedrally coordinated to oxygen are out of the framework (extra framework).

Experimental

The samples were packed in a zirconium rotor, 4 mm diameter, and a Kel-F (neppe) cap. ^{27}Al-NMR spectra were recorded using a Bruker AMX-200 instrument. A frequency of 52.138 MHz, and spinning speed of 5 kHz was used. A Number of 64k (i.e. 65536) scans were accumulated with a recycle delay of 10ms.

4.7 Temperature Programmed Desorption (TPD)

Background

Desorption is one of the steps in a complete catalytic cycle, and it a base for temperature programmed desorption. In TPD analysis, the catalysts saturated with adsorbed species on the surface are mounted in a vacuum chamber, where the temperature is increased linearly with time. At sufficiently high temperature, desorption of the adsorbed species will occur. The concentration of the desorbing species is monitored with mass spectrometer or with a simple pressure gauge [1]. TPD instruments are equipped with a vacuum pump, and during experiment high pumping speed is used, so that re-adsorption of the desorbed species will be controlled.

The relative rate of desorption, i.e. the change in adsorbate coverage per unit time, is given by

$$r = \frac{d\theta}{dt} = k_{des}\theta^n = v(\theta)\theta^n exp\left[-\frac{E_{des}(\theta)}{RT}\right] \tag{4.8}$$

$$T = T_o + \beta t$$

Were r is the rate of desorption, θ the coverage in monolayers, t the time, n the order of desorption, T_o the temperature at which the experiment starts, v the pre-exponential factor, E_{des} the activation energy of desorption, and β the heating rate.

A given TPD pattern is a source of valuable information. The area under the peaks is proportional to the initial coverage of the adsorbate, and the temperature at which the desorption occurs is a function of the strength of adsorption interaction between the catalyst and the molecule [1].

Acidity of Zeolites can be investigated using TPD. Acidic zeolites are known to have at least two weight loss regions, which are attributed to desorption of species from weak and strong acid sites in the material [54].

$$Acidity = \frac{\%\ mass\ loss}{100} \cdot \frac{1}{MW.of\ base} \cdot \frac{1000\ g}{1\ g} \qquad (4.9)$$

Where $W\ (g)$ is the weight loss due to desorption of base in chemisorbed region, and acidity is reported in units of millimoles of acid sites per gram of zeolite

Experimental

NH_3-TPD experiments were performed in Holder Topsoe, Denmark. Figure 4.4 together with Table 4.1 displays the various steps performed during the experiments. The red curve corresponds to temperature and the black curve corresponds to the mass of the catalyst.

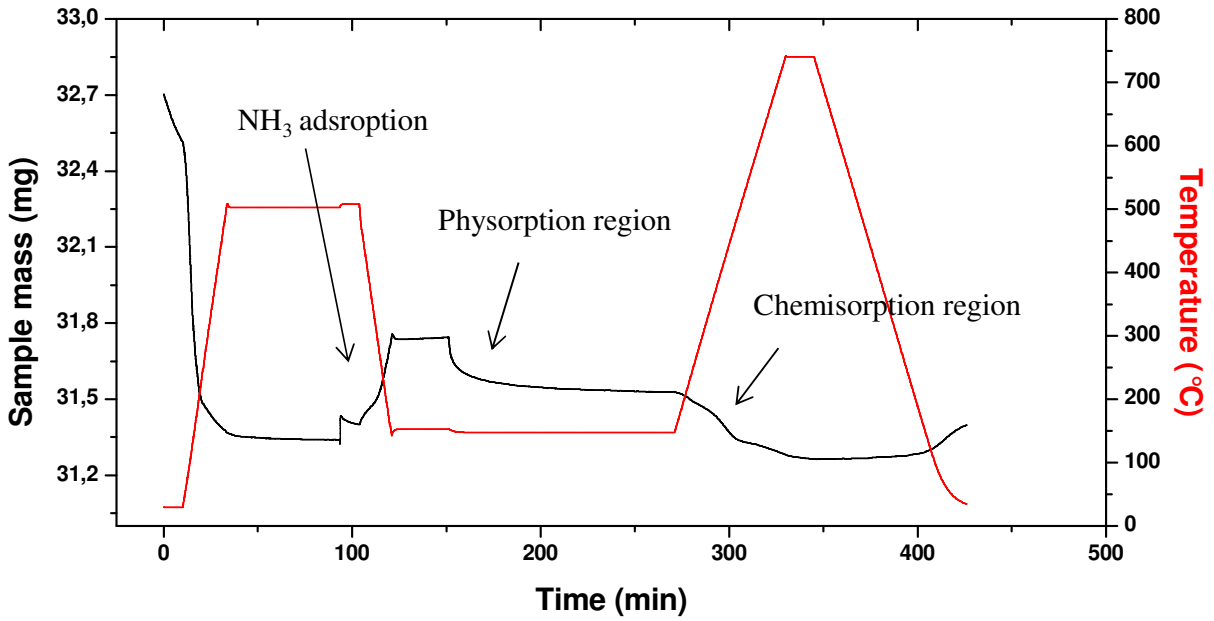

Figure 4.4: The various steps carried out under TPD analysis.

Table 4.1 The various steps carried out under TPD analysis.

Temperature	Heating rate	Hold time	Gas flow	Result
30 °C 30-500 °C 500 °C	-- 20 --	10 min -- 60 min	75 ml/min N_2 75 ml/min N_2 75 ml/min N_2	Drying and removing adsorbed species
500 °C 500-150 °C 150 °C	-- -20 30	10 min -- --	2% NH_3 in 75 ml/min He 2% NH_3 in 75 ml/min He 2% NH_3 in 75 ml/min He	Cooling and adsorption of NH_3
150 °C 150-165 °C	120 10	-- --	75 ml/min N_2 75 ml/min N_2	Desorption of physisorbed NH_3
165-740 °C 740 °C	10 --	-- 15 min	75 ml/min N_2 75 ml/min N_2	Desorption of chemisorbed NH_3
740-30 °C 30 °C	-10 --	 10 min	75 ml/min N_2 75 ml/min N_2	Cooling

4.8 Infra Red Spectroscopy (FT-IR)

Background

A basic principle of vibrational spectroscopy is usually described using a ball-and-spring model, using Hooke's law, which is explained by assuming two atoms m1 and m2 connected by a massless spring. The resulting force of the spring *F* is proportional to the displacement of x of the atom from their equilibrium position,

$$F = -kx \tag{4.10}$$

Were *k* is force constant of the spring, which is the measure of the strength of the bond between the two atoms (Nm^{-1}). Based on this assumption a ball-and-spring model is a harmonic oscillator. The vibrational frequency (v_o) in Hz of the harmonic oscillator in terms of classical mechanics is given by

$$v_0 = \frac{1}{2\pi}\sqrt{\frac{k}{m}} \tag{4.11}$$

Where *m* is the reduced mass in kg and given by

$$m = \frac{m_1 m_2}{m_1 + m_2} \tag{4.12}$$

Transitions between vibrational energy levels occur by absorption of photon with a frequency (vo) in infrared region. Absorption of photon occurs only if the dipole moment of the molecule changes during the vibration. Allowed transitions in harmonic approximation are those for which the vibrational quantum number (n) changes by one unit [1]. However, in realistic potentials forbidden transitions ($\Delta n > 1$) can occur and such transitions are called overtones [1]. Note that in Equation 4.11 only two molecular properties determine the frequency at which a molecule will absorb infrared radiation. The properties are the force constant, the chemical bond between the atoms, and the reduced molecular mass of the atoms. The stronger the force between the atoms, the higher is the frequency of absorption.

The various sites in zeolites absorb photons at different frequencies, and they can be identified using FTIR spectroscopy. Investigation of acid strength of a zeolite can be made by observing the change in absorption frequencies caused by adsorption of probe molecules on active sites of a zeolite. In this thesis CO was used as a probe molecule, the position of the bands due to the interaction of CO with the zeolite acid sites are presented in Section 6.1.6.

Experimental

Thin self-supporting wafers were prepared and their transmittance for IR radiation was checked prier to pretreatment. The wafers were pretreated under vacuum for 3 hours. 1 hour each at temperatures of 120, 350, and 450 °C. Spectra were collected on FTIR Bruker vertex 80 with MCT detector, working at 2 cm^{-1} resolution and a number of 64 scans. Carbon monoxide (CO) was used as a probe molecule, and its interaction with ZSM-22 catalysts has been followed at a temperature of 77 K by using liquid nitrogen as a coolant.

4.9 Thermogravimetric Analysis (TGA)

Background

The scope of this work is to investigate the amount of organic template in the as-made ZSM-22 catalysts and the amount of coke formed in the catalyst after the MTH reaction. The weight loss by removing the organic template from the as-made catalysts or coke formed during catalyst testing was investigated.

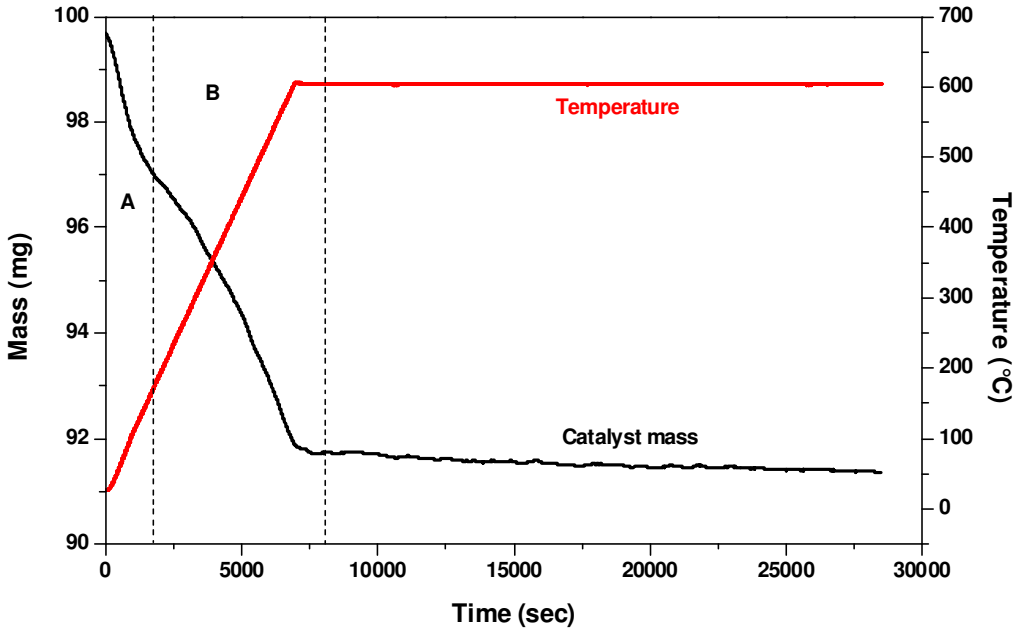

Figure 4.5 TGA plot obtained from ZSM-22 catalyst.

Figure 4.5 displays a TGA plot for a zeolite sample. Two weight regions are observed, region A is due to water loss and region B is due to coke/template oxidation. The weight loss reported in this thesis is based on the weight loss in region B.

Experimental

~10 mg of the catalysts (as-made or tested) was used for the experiments. The organic template or coke was removed by oxidation in oxygen. The temperature of the TGA instrument (Rheometric Scientific SAT 1500) was programmed between 25 and 600 °C (heating rate = 5 °C min^{-1}, hold time = at least 120 min at 600 °C)

5. CATALYTIC TESTS

List of reagents used in the catalytic test of ZSM-22 is presented in Appendix-1.

5.1 Test ring

The reactor system used for the experiments in this master thesis was designed by Rønning [55]. The catalyst testing reaction temperatures were varied between 350-500 °C, most of the experiments were performed at 400 °C. The reaction temperature was measured using a thermocouple inserted inside the catalyst bed.

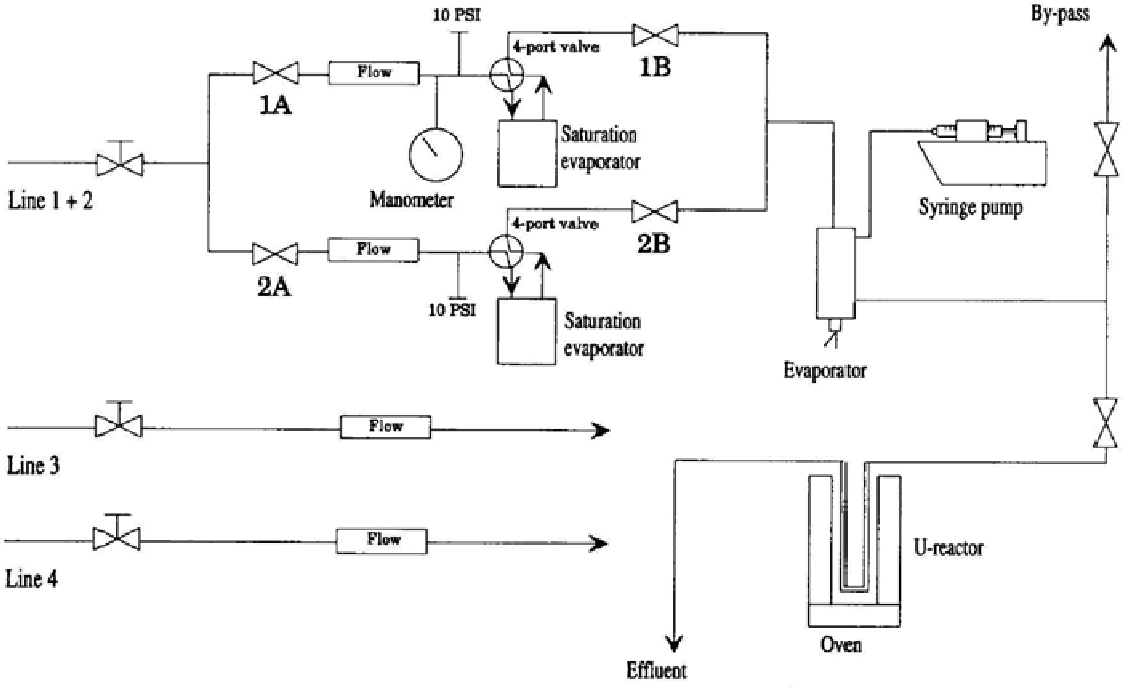

Figure 5.1 Schematic drawing of the reactor system [55].

Figure 5.1 displays a schematic drawing of the reactor system. The carrier gas (He) flow was controlled by Porter P-150 ball flowmeters. Lines 1 and 2 were fitted with saturation evaporators allowing the feeding of liquid reactants. ^{12}C and ^{13}C methanol were fed by passing the carrier gas through the saturation evaporator 1 and 2 respectively. These saturators are bubble saturators where the carrier gas bubbles through the liquid feed present in the saturator. The carrier gas becomes saturated according to the vapor pressure of the reactant at

the temperature of the water bath surrounding the saturators. This means that the partial pressure of methanol may be controlled by controlling the temperature of the saturation evaporators. Line 3 was used for feeding pure He. Line 4 was connected to pure oxygen, used for *in situ* calcination of ZSM-22 prior to catalytic experiments at 550 °C for 1 hour.

5.2 Catalyst, reactor and test conditions

ZSM-22 catalysts were pressed, gently crushed and sieved to a particle size of 0.25-0.42 mm to avoid pressure development over the catalyst bed. All catalytic experiments were carried out in a U-shaped, fixed bed glass reactor with internal diameter 10 mm. Before each test, the reactor was heated to 550 °C under a flow of helium. The catalysts were calcined *in situ* at this temperature with a flow of pure oxygen for 1 hour. Then the reactor temperature was cooled to the experimental temperature where it stayed for half an hour under a flow of helium before methanol feed. Except for a few experiments performed at different temperature and feed rates, the standard test conditions are presented in listed Table 5.1.

Table 5.1: Standard test condition used for the MTH reaction over ZSM-22.

Amount used	50 mg
He flow	10 ml/min
Saturation temperature	20 °C
Reaction temperature	400 °C

In addition to the standard test conditions and catalyst displayed above, other ZSM-22 catalysts were tested in a temperature range of 350 – 500 °C and feed rate (WHSV) between 2.05 – 4.05 g $g^{-1}h^{-1}$.

5.2 Product analysis

5.2.1 Online effluent analysis

In all experiments the first GC analysis was performed after feeding methanol for 3 minutes, automatic injection was used. Each GC analysis took 29.6 minutes, and most of the reactions were stopped after complete deactivation of the catalyst. The reactor effluent was analyzed by on-line Gas Chromatography (Agilent 6890 A with FID) using a Supelco SPB-5 capillary

column (60m, 0.530 mm i.d., stationary phase thickness 3µm). The temperature was programmed between 45 and 260 °C with a heating rate of 25 °C min^{-1} (hold time = 5 min at 45 °C and 16 min at the final temperature).

5.2.2 Offline effluent analysis

Detailed Analysis of the composition of the effluent, especially C_{5+} fraction, and isotopic switch experiments were performed with a HP 6890 gas chromatograph equipped with a GS-GASPRO column (60m, 0.32 mm) and a HP-5973 Mass Selective Detector. Each analysis took 40 minutes, and the temperature was programmed between 100 and 250 °C with a heating rate of 10 °C min^{-1} (hold time = 10 min at 100 °C and 15 min at 250 °C)

5.3 Analysis of retained hydrocarbons

5.3.1 Qualitative analysis

After reacting methanol over ZSM-22 catalyst for a certain time, the retained hydrocarbons in the material were analyzed following dissolution procedures as described in literatures [35, 38]. 20 mg of spent ZSM-22 catalyst was transferred into a screw-cap teflon vial and 1ml of 15% HF was added. After 45 min the catalyst was dissolved completely. To the resulting catalyst-acid solution, 1 ml of dichloromethane (CH_2Cl_2) having hexachloroethane (C_2Cl_6) as an internal standard was added. Half an hour later, the organic phase was extracted and analyzed using an Agilent 6890N Gas Chromatograph connected to an Agilent 5793 Mass Selective Detector equipped with either a HP-Innovax column (60 m, 0.25 mm i.d., stationary phase thickness 0.5 µm) or a HP-5MS column (60 m, 0.25 mm i.d., stationary phase thickness 0.25 µm). The temperature was programmed between 60 and 240 °C with a heating rate of 5 $^oC\ min^{-1}$ in the range 60-200 °C and 20 °C min^{-1} in the range 200-240 °C (hold time = 5 min at 60 °C, 20 min at 200 °C and 20 min at the final temperature). The compounds were identified by comparing with the mass spectral library of NIST98 database.

5.3.2 Analysis hydrocarbons retained on the external surface of ZSM-22

The motivation for this experiment is presented in section 6.4.2. ZSM-22 catalyst deactivated at 400 °C was washed with CH_2Cl_2 to remove retained hydrocarbons from the external surface

of the catalyst. 20 mg of the catalyst was transferred into a small flask and to this 1ml of CH_2Cl_2 with hexachloroethane standard was added. The resulting mixture was kept overnight at room temperature. The CH_2Cl_2 was removed and analyzed using GC-MS. The catalyst was further washed by adding 1ml CH_2Cl_2 and was refluxed at 50 °C in a water bath. The washing process by refluxing at 50 °C was repeated 10 times. Finally, the washed catalyst was acid digested and the organic extract were analyzed using GC-MS as described in Section 5.3.1.

5.3.3 Quantitative analysis

20 mg of spent ZSM-22 catalyst was dissolved in 15% HF and the retained hydrocarbons were analyzed as described in Section 5.3.1. The response factor of the GC-MS instrument for compounds of interest was calculated (see Appendix 4), and the concentration of retained hydrocarbons is calculated from the response factor and the relative area of the compounds, and it is given by

$$C_{mmol/L}(x) = \frac{A_{rel}(x)}{K_{L/mmol}(x)} \tag{5.1}$$

Where $C_{mmol/L}\ (x)$ is the concentration of the compound *'x'* in millimol per liter, $A_{rel(x)}$ is the relative area of compound *'x'* (obtained by dividing the area of the compound by the area of the standared C_2Cl_6), and $K_{L/mmol\ (x)}$ is the response factor of the GC-MS for the compound *'x'*. The concentration of zeolite in the solution was calculated using the molecular mass of silica (SiO_2) and is given by

$$C_{mol/L}(SiO_2) = \frac{mass\ dissolved\ (g)}{60\ g/mol} \tag{5.2}$$

Dividing Equation 5.1 by Equation 5.2 gives the concentration of retained hydrocarbons per the concentration of dissolved zeolite, and multiplying the resulting concentration with Si/Al ratio of the catalyst gives the concentration of retained hydrocarbons per acid sites, and this is used to calculate the number of retained hydrocarbon per acid site.

To calculate the number of retained hydrocarbons in a channel, the number of retained hydrocarbons per unit cell was calculated. This can be performed by calculating the number of acid sites in a unit cell, which can be obtained by dividing the number of T-atoms in a unit

cell by the Si/Al ratio. From the number of retained hydrocarbons per unit cell, the distance between the retained hydrocarbons was calculated and used to determine the number of hydrocarbons in a channel.

5.4 Isotopic labeling studies

The isotopic distribution of the ^{13}C was determined in both effluent and retained hydrocarbons of the MTH reaction over ZSM-22 catalyst. The procedure for determining isotopic distribution is developed by Per Rønning [55].

The calculation is based on only molecular ions and fragment ions with intact carbon skeletons, it is assumed that there is no kinetic isotope effect. Three standard ^{12}C-spectra were recorded by reacting ordinary ^{12}C-methanol and corrected for the naturally occurring ^{13}C-atom (1.11%) in a molecule. The average of the three ^{12}C-spectra was used for the calculation.

For a given ion with N carbon atoms with mass number m/z = i, the statistical probability that the ion contain n^{13}C-atom is given by

$$P_n = \frac{N!}{n!\,(N-n)!} \cdot 0.0111^n \cdot 0{,}9889^{N-n} \tag{5.3}$$

Where P_n: Statistical probability, $\frac{N!}{n!(N-n)!}$: Number of permutations of n^{13}C atoms in an ion with N carbon atoms.

The single ion peak was integrated and corrected for naturally occurring ^{13}C. The corrected single ion peak area is given by

$$A_{corr}(i) = A_{obs}(i) - \frac{\sum_{n=1}^{N} A_{corr}(i-n) \cdot P_n}{0{,}9889^N} \tag{5.4}$$

Where P_n: Statistical probability, $A_{corr}(i)$: Corrected single ion peak area with ion mass i, $A_{obs}(i)$: Observed single ion peak area with ion mass i, and $A_{corr}(i\text{-}n)$: Corrected single ion peak area with ion mass i-n.

Single ion peak chromatograms were extracted from the Total ion chromatogram and integrated. The single ion peak area is a sum of ions with the same mass numbers but with different number of hydrogen atoms ^{13}C atoms, for example the area of the ion peak m/z = 25 in the Total ion chromatogram of ethene is the sum of contributions from ^{12}C-^{12}CH and ^{13}C-^{12}C. The observed peak area of ion with mass number i is given by

$$A_{obs}(i) = A_{sum}D_{12c}(i)X_{12C} + \sum_{n=1}^{N} A_{sum}D_{12c}(i-n)X(n) \quad (5.5)$$

Where Asum: Sum of ion peak areas, $D_{12C}(i)$: Fraction of ions with mass number i in a pure ^{12}C spectrum, X(n): Fraction of ions containing n ^{13}C atoms, and X_{12C}: Fraction of ions containing ^{12}C atoms only. Other symbols as before. Equation 5.5 expresses the observed single ion peak area as linear combination of the fraction of 13C atoms in the ion. A set of linear equations are formulated for a given compound and solved using multivariable linear regression procedure. An Excel spreadsheet programmed to formulate appropriate set of equations for a given compound and to solve the set of equations is used for the calculations.

The agreement between the model and observed data is given by the correlation coefficient from the regression and the root mean square, defined as the squares the difference between observed and calculated single ion peak areas.

Experimental

The experiments were conducted at 400 °C, WHSV = 2.05 $gg^{-1}h^{-1}$. Ordinary ^{12}C methanol was fed for 5 or 18 min followed by a switch to ^{13}C methanol. The isotopic compositions of both the effluent and the organic retained materials in the zeolite channel were determined after the $^{12}C/^{13}C$ methanol switch. The ^{13}C content in the reaction effluent was determined after reacting ^{13}C methanol for 0.5, 1.0, and 2.0 min. The effluents were analyzed using GC-MS (see Section 5.2.2). The ^{13}C content in the retained organic materials was determined by thermally quenching the reaction after 0.5, 1.0, and 2.0 min of ^{13}C methanol reaction. 20 mg of the catalysts were dissolved in 15% HF, the organic materials were extracted with CH_2Cl_2 and analyzed using GC-MS (see Section 5.3.1).

6. RESULTS AND DISCUSSION

6.1 Materials synthesis and characterization

6.1.1 XDR and SEM

Synthesis Using 1-Ethylpyridinum Bromide As Structure Directing Agent

In Appendix 3 lists of syntheses of ZSM-22 catalyst are presented. In the following sections, the syntheses that resulted in ZSM-22 crystals are presented.

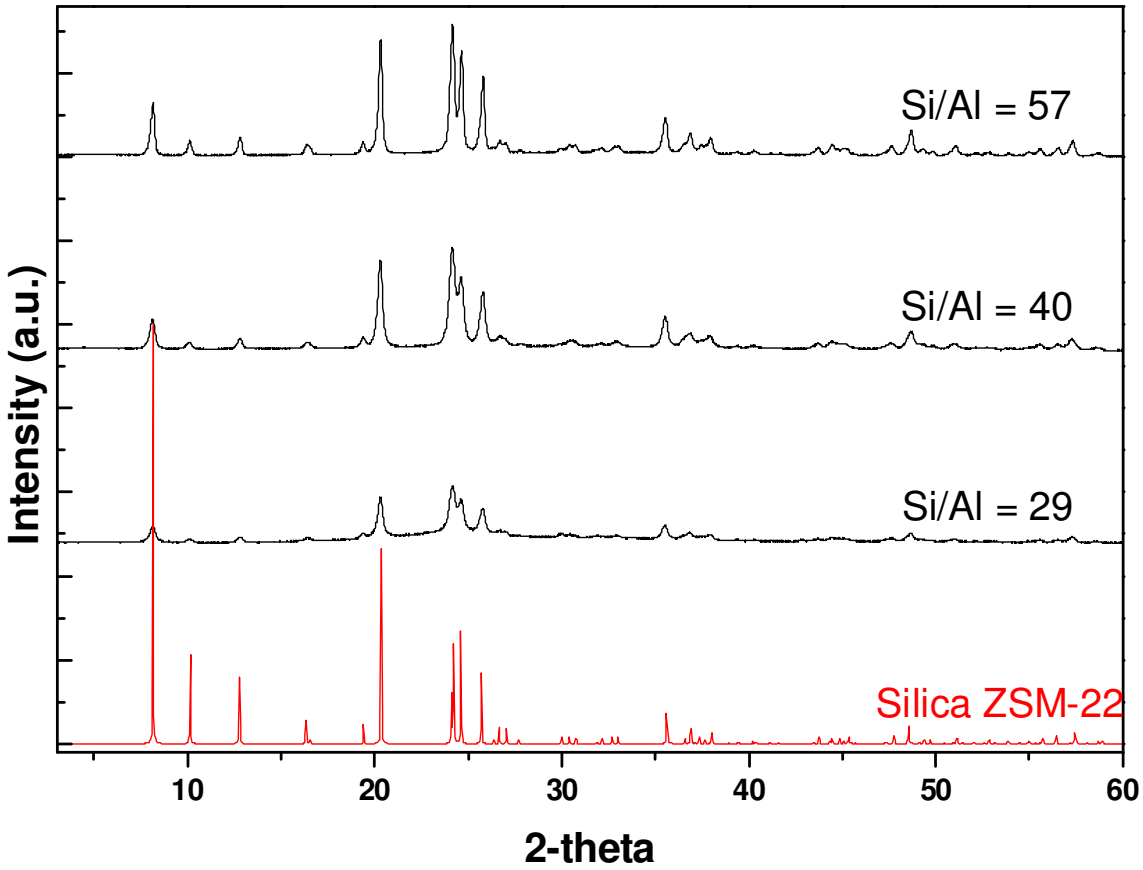

Figure 6.1 XRD diffraction profile of ZSM-22 catalysts having different Si/Al ratios in the synthesis gel, Appendix 3 synthesis number 1.2 to 1.4.

Figure 6.1 displays the XRD patterns of the products obtained after 4 days of crystallization under static conditions, Appendix 3 synthesis number 1.2 to 1.4. Calculated diffraction pattern for silica ZSM-22 is displayed for comparison with experimental results. Note that the intensities of the reflections (especially at low angels) are affected by preferred orientation of the crystals during data collection. The products having Si/Al = 29 was not fully crystalline, however, all of the products were free from structural impurities.

Figure 6.2 displays SEM images of the catalysts. The catalysts having Si/Al = 29 and 57 in the synthesis gel (Figure 6.2 a and b) were needle shaped crystals of 2-3 µm length. Needle shaped crystals are typical for ZSM-22 [56]. If the needles are too long, the zeolite can have a fibrous quality similar to asbestos and can be a health hazard, short crystals are less toxic [57].

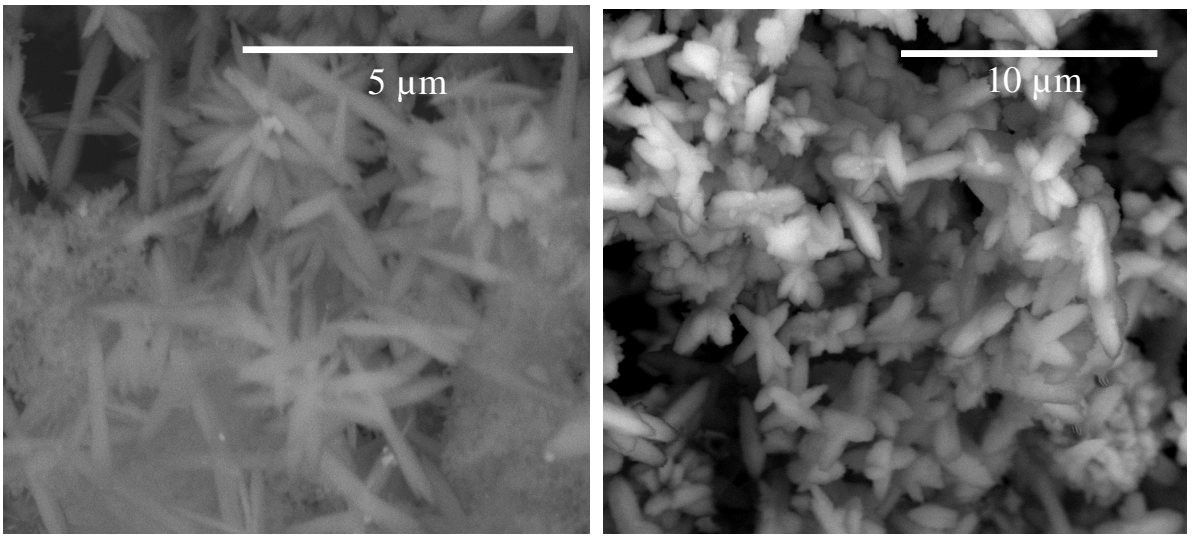

a) b)

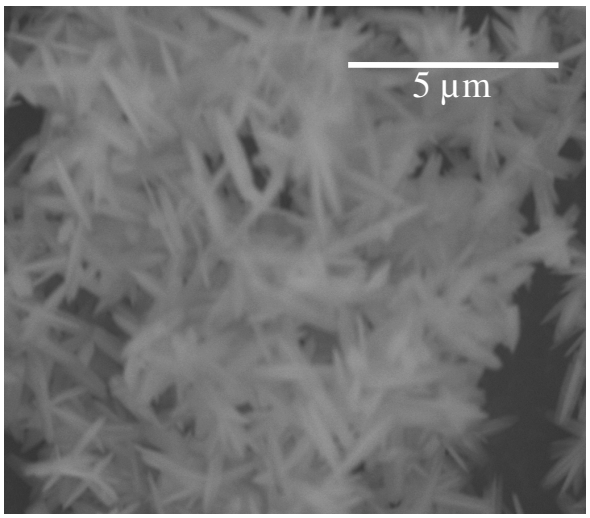

c)

Figure 6.2 SEM images of ZSM-22 catalyst having different Si/Al ratios in the synthesis gel a) Si/Al = 29, b) Si/Al = 40, and c) Si/Al = 57, Appendix 3 synthesis number 1.2 to 1.4.

The catalyst having Si/Al = 40 exhibits a different morphology. The crystals were rice-like in shape and 2-3 µm in length.

Synthesis Using Diethylamine As Structure Directing Agent

Figure 6.3 displays the X-ray diffraction patterns for ZSM-22 catalyst obtained after 2 days of crystallization in vertical rotation conditions, Appendix 3 synthesis number 2.1 and 2.2. Both

of the products having Si/Al = 15 and 30 were in a good crystallinity and free from structural impurities. The positions of the peaks are compared with calculated diffraction pattern for silica ZSM-22. SEM images reveled needle shaped crystals of 1-2 µm in length, displayed in Figure 6.4.

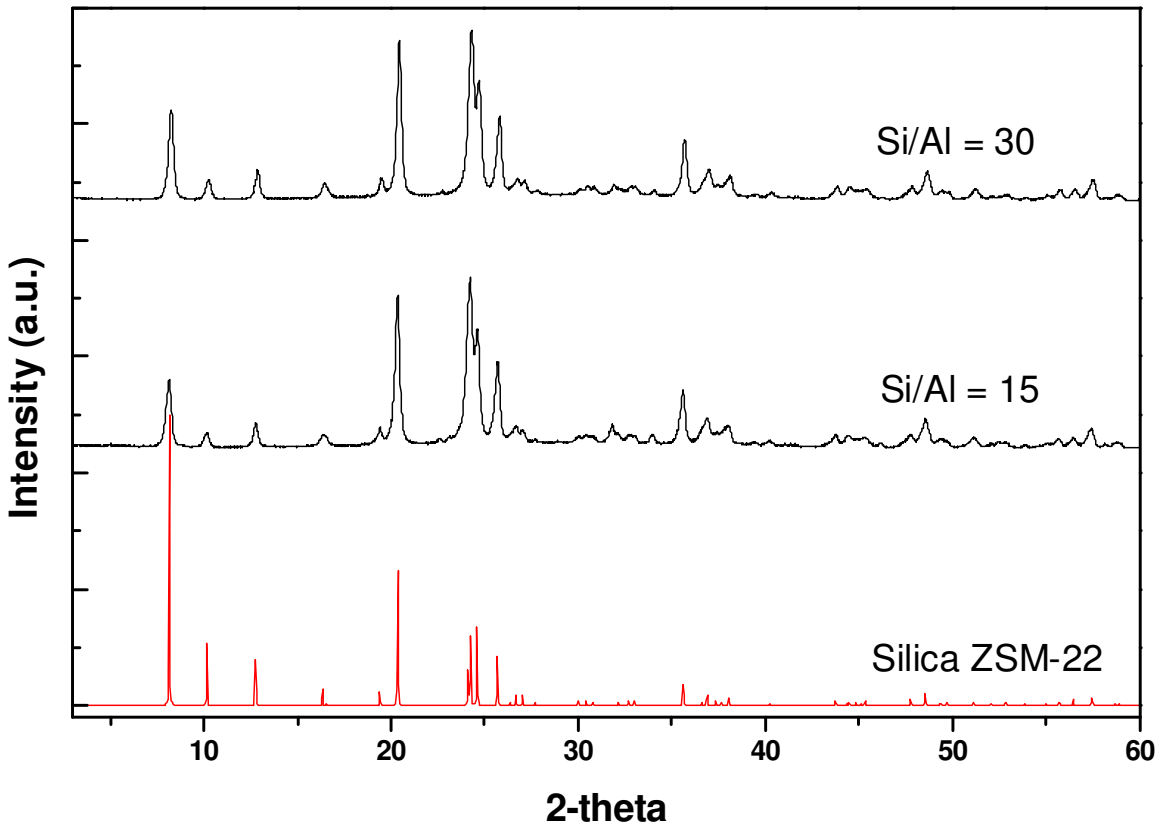

Figure 6.3 XRD profile of ZSM-22 catalysts with different silicon to aluminum ratios in the synthesis gel, Appendix 3 synthesis number 2.1 and 2.2.

From these observations, it is clear that short crystallization time is required when using Diethylamine as structure directing agent and it gives smaller crystals that the products obtained when using 1-Ethylpyridinum Bromide as structure directing agent.

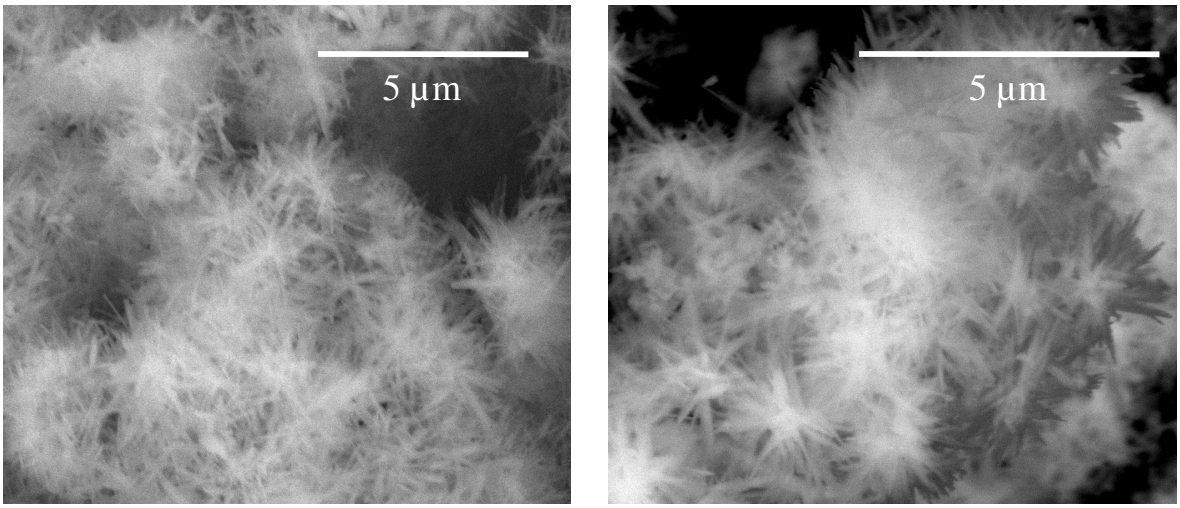

Figure 6.4 SEM images of ZSM-22 catalysts having Si/Al = 15 (left panel) and Si/Al = 30 (right panel) in the synthesis gel, Appendix 3 synthesis number 2.1 to 2.2.

Synthesis using 1, 8-diaminooctane as structure directing agent

A large volume of the synthesis gel (~120 ml) described in Section 3.1 was prepared and divided into 4 autoclaves (Appendix 3 synthesis number 3.1 to 3.4). Crystallization of the gel in two of the autoclaves was carried out under vertical rotation conditions in a tumbling oven (25 rpm), one of the autoclaves was kept under static condition and for the fourth autoclave crystallization occurred under horizontal stirring conditions using a Teflon coated bar magnet.

Figure 6.5 displays the XRD patterns of the products obtained from the different ovens. A calculated diffraction pattern of sililca ZSM-22 (bottom pattern) is also displayed for comparison with the experimental results. The XRD pattern of the product obtained from vertical rotation oven (25 rpm) was free from commonly incured structural impurities of ZSM-5 and cristobalite (a denser structure) [56], and no unreacted amorphase phase was observed which is evidenced by a flat baseline. The product obtained from horizontal stirring oven was also in a good crystallinity. However, a small peak at 2θ ~21.7°, appears to be as a result of structural impurity cristobalite. Several publications have reported the formation of impurities together with TON zeolites [11, 58], and it is usually associated with inhomogeneous mixing of the synthesis gel and from materails stuck on the wall of the Teflon liner during crystallization [56]. The synthesis carried out under static conditions resulted in formation of MEL type ZSM-11 zeolite. ZSM-11 is also a 10-ring zeolite having a three

dimensional 10-ring pore system [2]. The ZSM-11 product was not perfectly crystalline but no structural impurities were observed.

A possible explanation has been given by Derewinski, and Machowska [59] for the crystallization of ZSM-11 under static condition while rotating the autoclave led to formation of ZSM-22. According to the explanation, the formation of the TON unit cell requires structural rearrangement of 24-T atoms only, whereas the MEL unit cell consists of 96-T atoms. Thus, its formation and subsequent arrangement into large structures requires longer range of ordering of the reacting species, which is easier to achieve in a less perturbed, static system [59].

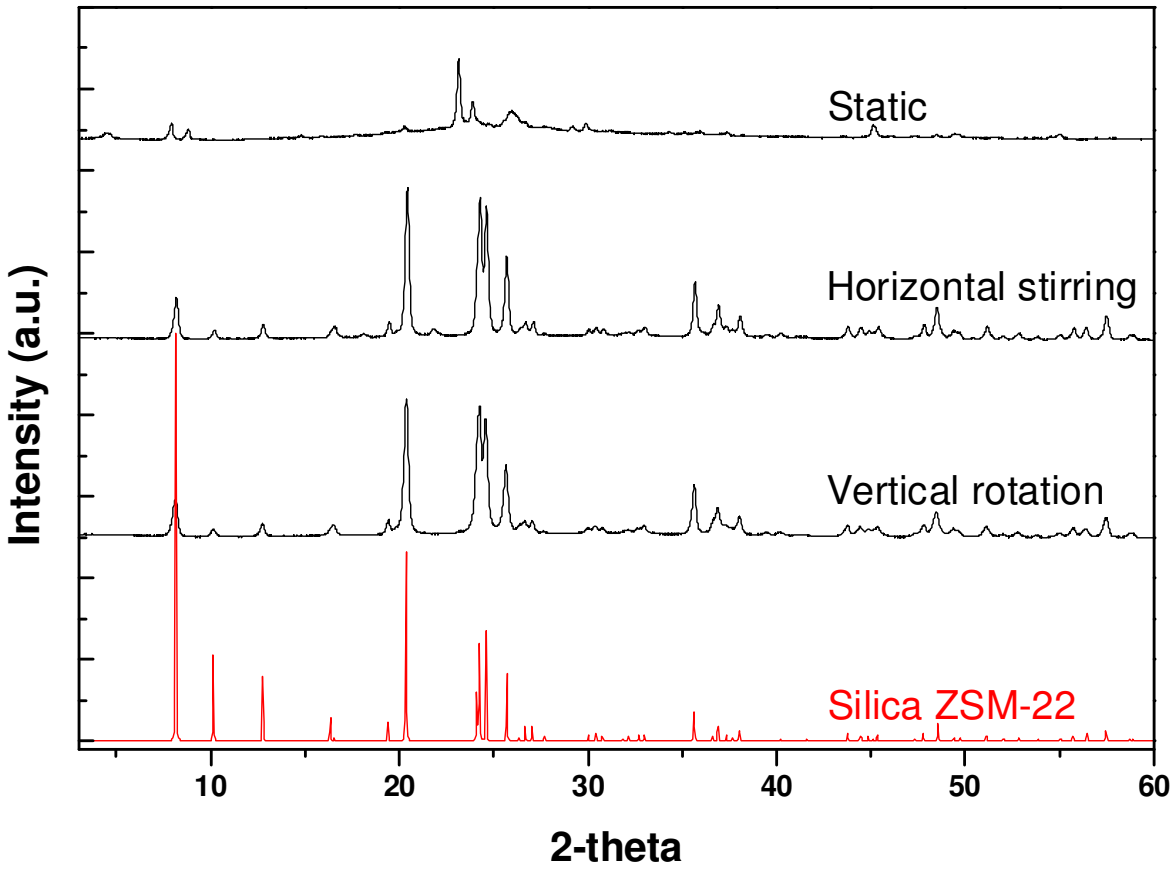

Figure 6.5 XRD pattern of synthesis products obtained from different ovens, identical synthesis gel was used, Appendix 3 synthesis number 3.1 to 3.3.

Figure 6.6 displays SEM images of the products the ZSM-11 and the pure ZSM-22 products, the SEM image of the synthesis that resulted in small amounts of impurity is similar to the image displayed in Figure 6.6 (left panel), the impurity phase was not observed in SEM. As

can be seen from the images the ZSM-11 crystals were ~20 µm in size and the size distribution was more or less uniform. Large size of crystals restricts the zeolite application in catalysis, as diffusion limitations appear during transport of reactant and product molecule in large crystals. The ZSM-22 crystals obtained from both the vertical rotation and horizontal stirring oven were needle shaped and 2-3 µm in length.

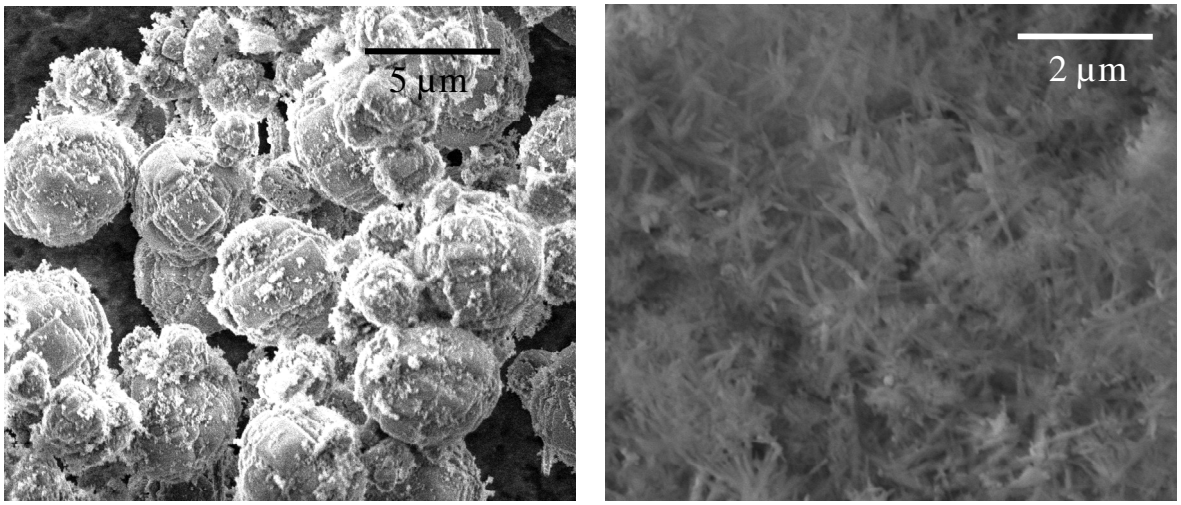

Figure 6.6 SEM micrographs of products obtained from different ovens, identical synthesis gel was used, Appendix 3 synthesis number 3.1 and 3.3.

From these results it is clear that pure ZSM-22 catalyst can be synthesized using 1, 8-diaminoocatane as structure directing agent. Homogenization of the synthesis gel during the crystallization step is required, which may be achieved by either high speed stirring of the synthesis gel using magnetic stirring (horizontal stirring) or under milder conditions by vertical rotation of the autoclave.

Figure 6.7 shows XRD patterns for ZSM-22 catalysts having a Si/Al = 20, 30 , 80 and 100 determined using ICP-AES (Appendix 3 synthesis number 3.9 to 3.12). The catalysts having Si/Al = 20, 30, and 80 were pure from structural impurities. The catalyst having Si/Al = 100 was found to contain cristobalite impurity, indicated by "+". The calculated XRD pattern for silica ZSM-22 is displayed for compering the experimetnal result with the theoretically calculated pattern.

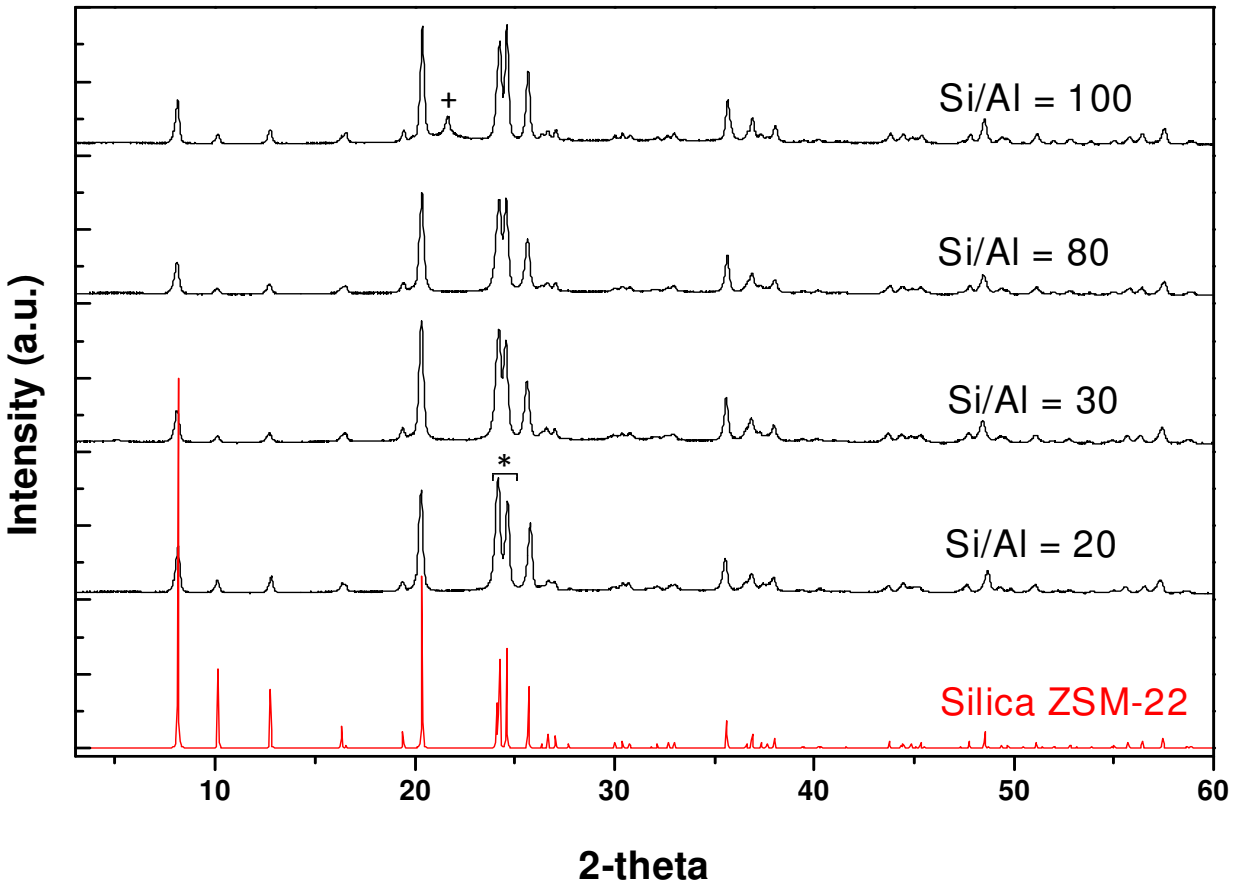

Figure 6.7 XRD diffraction profile of ZSM-22 catalysts with different silicon to aluminum ratios determined using ICP, (Si/Al = 20, synthesis number 3.9), (Si/Al = 30, synthesis number 3.8), (Si/Al = 80, synthesis number 3.20), (Si/Al = 100, synthesis number 3.21).

As can be seen from the diffraction pattern, the ratio between the intensities at reflections ~23 and ~24 ° (the peaks are indicated by *) seemed to be sensitive to the Si/Al ratio of the catalysts (Table 6.1).

Table 6.1 Intensity ratios between refelections at 2-theta = ~23 and ~24 ° at different Si/Al ratios

Si/Al	20	30	80	100
$I_{24^\circ}/ I_{23^\circ}$	0.8	0.9	1.0	1.2

As described in section 4.1.1, the observed intensities in a diffraction pattern are functions of the square of atomic scattering factor. This could mean that changing the composition of a unit cell would result in changes in observed intensities in a diffraction pattern. However, the atomic scattering factor for Si and Al is not significantly different (difference of one electron). This means that the observed variation in the relative intensities may not be directly related to the atomic scattering factor to Si and Al, instead it may be related to something else (unclear)

which is a function of Si/Al. Note that this intensity ratio between these peaks is also affected by alkali treatment of ZSM-22 (see Section 6.5.1). There was no noticeable intensity change on the intensities of the other reflections with changes in Si/Al ratios.

Figure 6.8 SEM Figure 6.8 displays SEM images of the catalysts having Si/Al = 20, 30, 80 and 100.

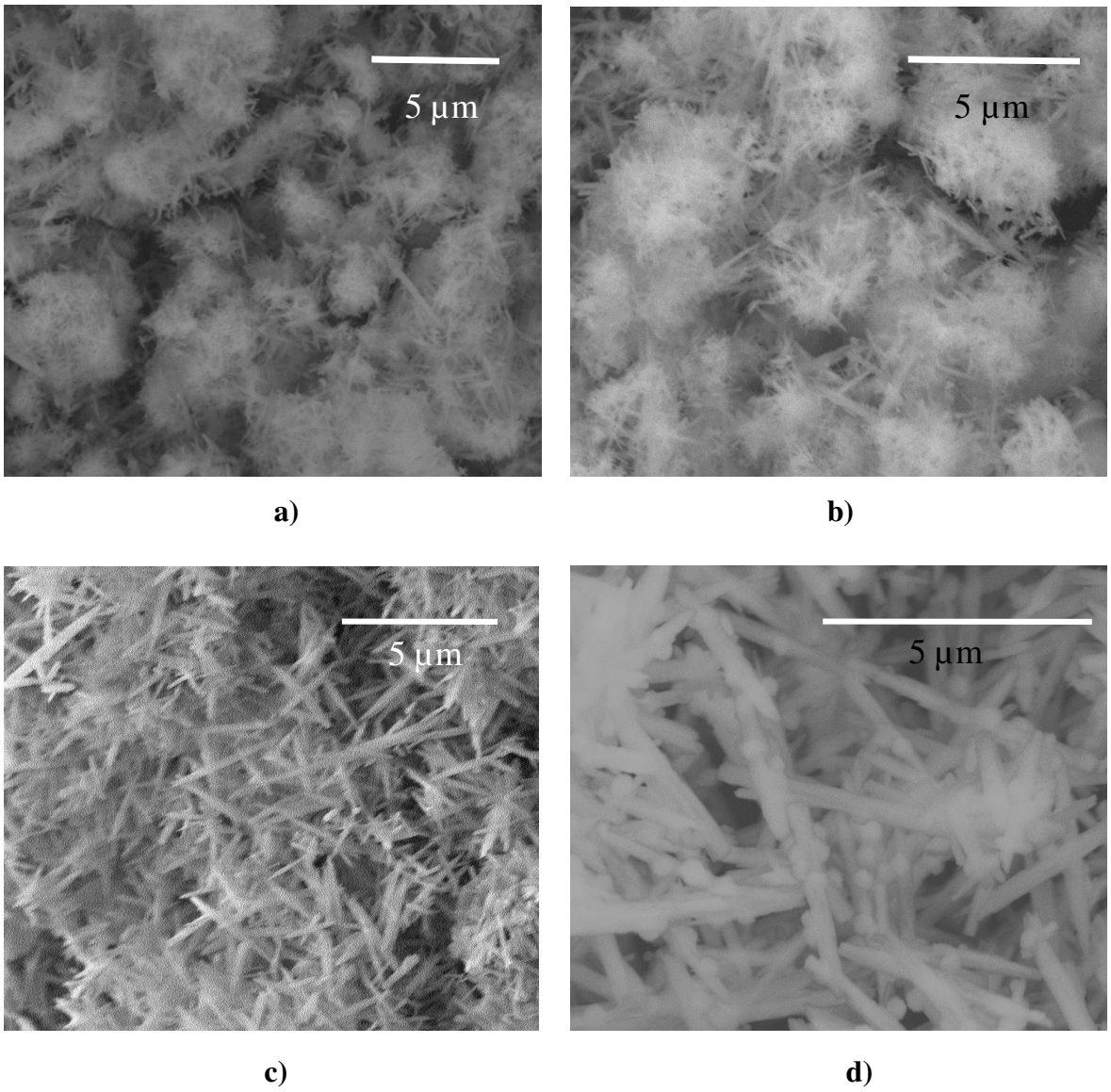

Figure 6.8 SEM of ZSM-22 catalysts having different Si/Al ratios determined using ICP, a) Si/Al = 20, b) Si/Al = 30, c) Si/Al = 80, d) Si/Al = 100

The catalysts having Si/Al = 20 and 30 were 1-3 µm in length and the catalyst having Si/Al = 80 and 100 were 2-4 µm in length. The cristobalite impurities in the catalyst having Si/Al = 100 are observed as a small round phase (Figure 6.8 d).

6.1.2 TEM

Figure 6.9 and displays TEM images of a ZSM-22 (Si/Al = 45 in the synthesis gel and 30 by ICP-AES, Appendix 3 synthesis number 3.3). TEM revealed broad particle size distribution between 50 nm to >1 µm (Figure 6.9 right panel), which is noticeably smaller that the crystal size investigated using SEM (2-3µm), and the crystals are irregular in shape. Based on this observation it is speculated that the high energy electron beam is breaking large crystals in to pieces of smaller crystals. This could mean that the actual crystal size is 2-3µm (SEM).

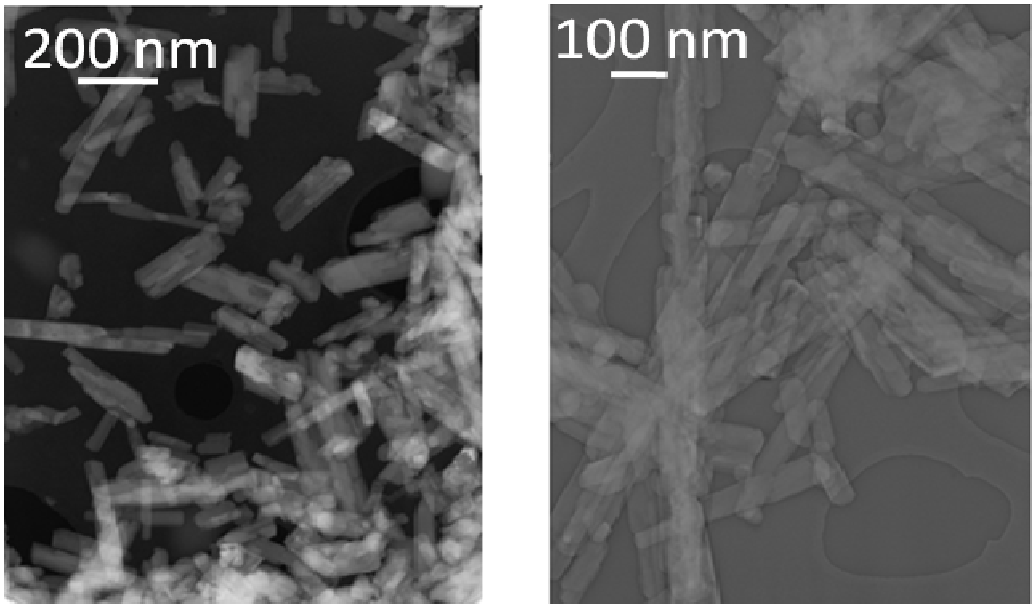

Figure 6.9 TEM images of ZSM-22 zeolite, Appendix 3 synthesis number 3.3.

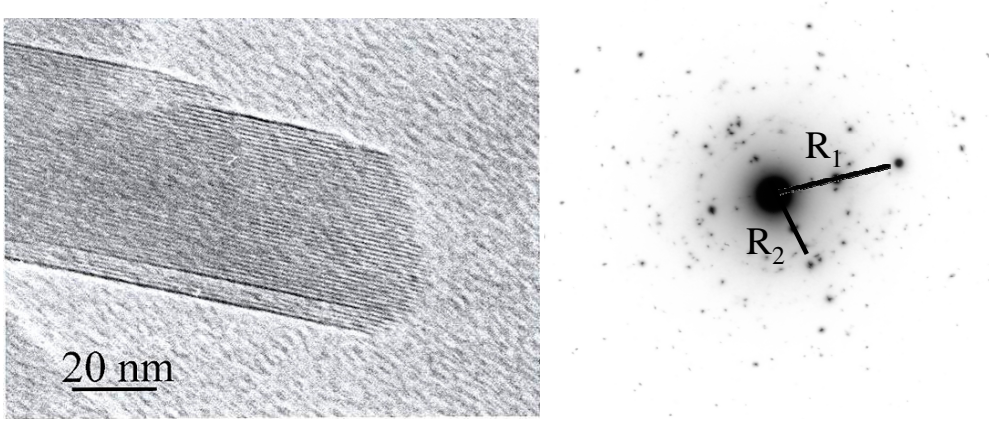

Figure 6.10 TEM images of ZSM-22 catalyst (left panel) and selected-area electron diffraction patent obtained from ZSM-22 catalyst (right panel), Appendix 3 synthesis number 3.3.

It has been reported that crystallization of ZSM-22 zeolite crystals are formed by aggregation of nanorods [60]. Massive formation of ZSM-22 nanocrystals (12±4 nm) was reported at the early stage of the reaction followed by sideway aligning and fusion of the nanorodes later in the carystalization process whereby the external surface is systematically converted into an internal micropore surface. Based on this statement, the crystals observed in SEM (1-3µm) could be agglomerates of nanorods.

Figure 6.10 (left panel) is sufficient to detect fine surface facets of the catalyst. These surface facets go along the fibers of the crystal and, they could seem to be the narrow channels of the catalyst. Note that the 10-ring channels of ZSM-22 crystals go along the fibers (the longest dimension of the crystals) [60, 61]. Analysis of the selected-area diffraction pattern (see Section 4.3) obtained from TEM (Figure 6.10 (right panel)) showed that distance between each surface facet was ~10 Å, which is much bigger than the channel dimensions of ZSM-22 (4.6 x 5.7 Å). Comparing this observation with XRD data, the distance between the facets (~10 Å) was matching the crystallographic *d*-spacing of the crystal. Thus, the surface facets observed in TEM are not channels of the material, instead they seem to be diffraction plans of the crystals.

6.1.3 BET

Table 6.2 presents BET surface area of several batches of catalysts. The observed surface area varies among catalysts synthesized from identical synthesis gel under the same crystallization conditions. This could be as a result of unidirectional narrow channels of the material in which any kind of extra framework species in the narrow channel can block a sizable fraction of the pores making them inaccessible for N_2 during BET measurement (discussion of this point can be seen in Section 6.1.6). Most of the catalytic tests were performed using the catalysts having surface areas of 173 and 207 m^2/g synthesis number 3.6 and 3.8), and hereafter they are denoted as ZSM-22(173) and ZSM-22(207) respectively (The surface area of ZSM-22 (TON framework) was theoretically calculated by simulating adsorption of nitrogen using Materials Studio 4.2, and a surface area 230 m^2g^{-1} was obtained. This indicates that some of the experimental results presented in Table 6.2 are not far from the expected theoretical BET surface area.

Table 6.2 surface area and micropore volume of several batches of ZSM-22 catalysts

Synthesis number	BET (m^2/g)	Langmuir (m^2/g)	Micro pore V ($cm^3\ g^{-1}$)
1.4	226	263	0,094
3.3	180	217	0,061
3.5	198	233	0,071
3.6	173	209	0,053
3.7	98	108	0,024
3.8	207	241	0,076
3.23	141	198	0,050
3.24	112	153	0,038

Figure 6.11 displays N_2 adsorption / desorption isotherms for representative ZSM-22(173) (left panel) and ZSM-22(207) (right panel) catalyts. These isotherms are representative for several batches of catalysts, and they are typical of microporous materials. Suface area in this range have been reported previously for the same structure [42, 60].

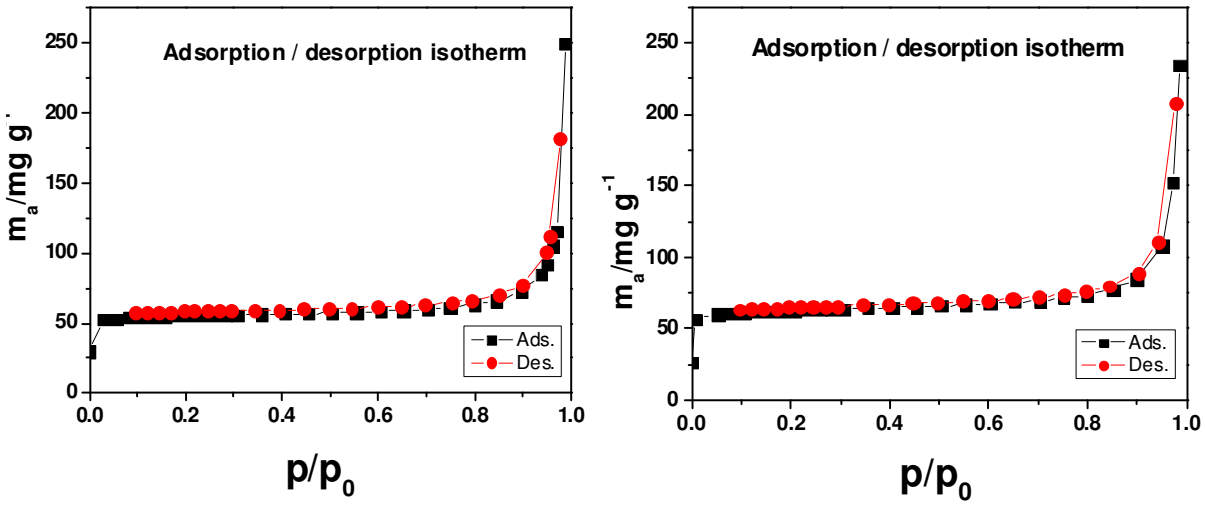

Figure 6.11: BET adsorption/ desorption isotherm of ZSM-22(173) (left panel) and ZSM-22(207) (right panel) catalysts, Appendix 3 synthesis number 3.6 and 3.8.

6.1.4 ^{27}Al-NMR

Figure 6.12 displays ^{27}Al-NMR spectra of ZSM-22(173) and ZSM-22(207) catalysts before and after calcinations/ion exchange. Clearly, only one peak at ~50 ppm is observed for both catalysts before calcination. After calcination and ion exchange, a very small peak at ~0 ppm was observed. For zeolites the peak at ~50 ppm is ascribed to framework Al (tetrahedral Al), and the peak at ~0 ppm is ascribed to non framework Al (octahedral Al) [62, 63].

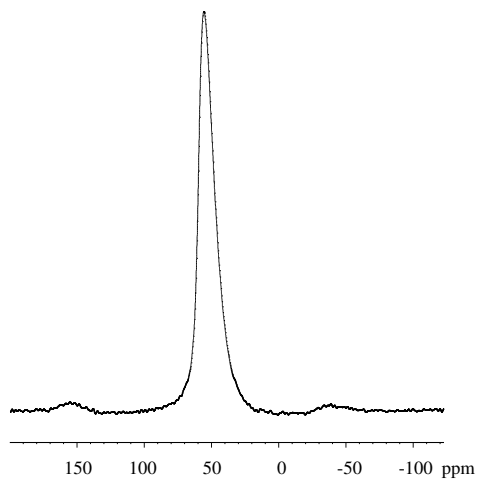

ZSM-22(173) before cacination / ion exchange

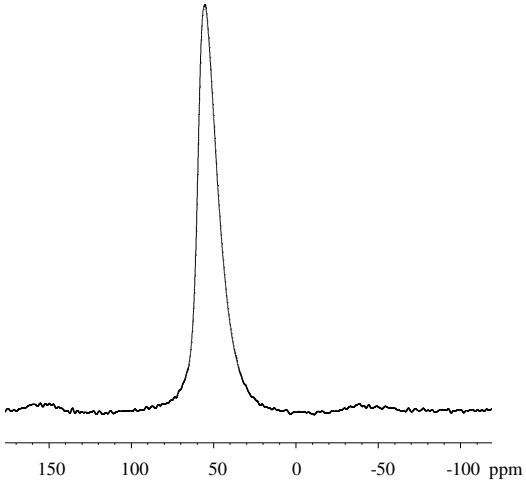

ZSM-22(207) before calcination /ion exchange

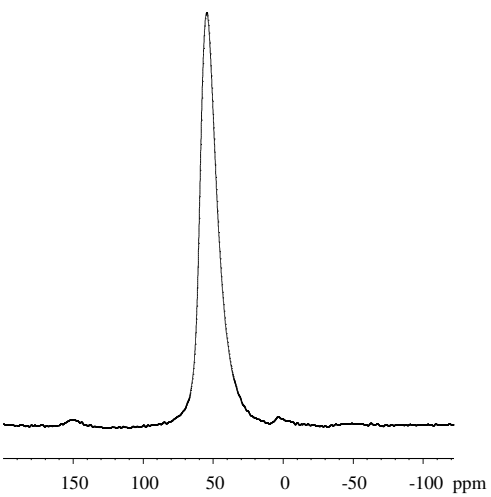

ZSM-22(173) after cacination / ion exchange

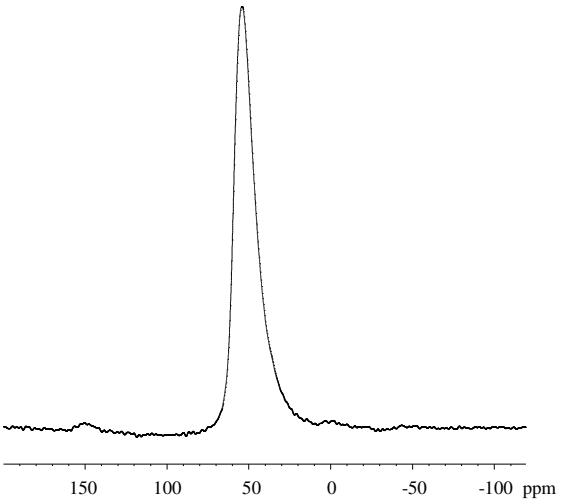

ZSM-22(207) after calcination /ion exchange

Figure 6.12 ^{27}Al-NMR spectra for ZSM-22(173) and ZSM-22(207) catalysts before and after cacination and ion exchage. The peak at 50 ppm corresponds to framework aluminum; the small peak at 0 ppm corresponds to extra framework aluminum.

This means that for the as-made ZSM-22 catalysts (before calcination) the entire Al was within the framework. After calcination and ion exchange, negligible amounts of extra framework Al were observed. Several batches of ZSM-22 catalysts were analyzed, and all of them were similar to the spectra displayed in Figure 6.12.

6.1.5 NH_3-TPD

The acidic property of ZSM-22(173) and ZSM-22(207) catalysts (Appendix 3 synthesis number 3.6 to 3.8) was investigated using NH_3-TPD. These catalysts were selected based on their stability in methanol conversion, see Section 6.2.1.

As shown in Figure 6.13, two weight loss regions at temperatures of ~230 and ~413 °C were observed. These regions are ascribed to desorption of weakly bound ammonia molecules and desorption of strongly bound ammonia molecules respectively [54]. Obviously, in both batches of catalysts heterogeneity in the acid sites is observed. The catalyst ZSM-22(173) desorbed a larger amount of ammonia molecules at a temperature of ~230 °C than ZSM-22(207), indicating that relatively more ammonia molecules are adsorbed weakly on this batch of catalyst than ZSM-22(207).

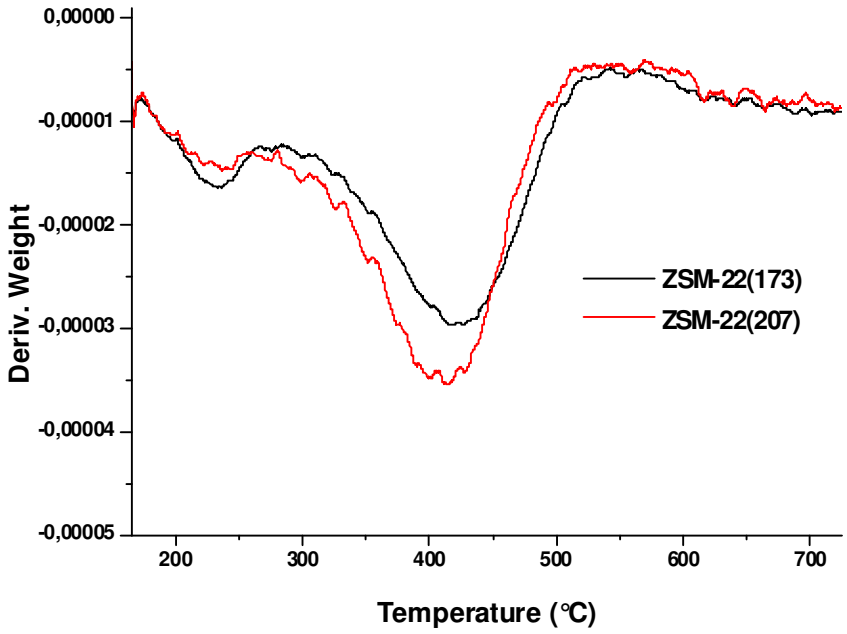

Figure 6.13: NH3-TPD derivative curves for the chemidesorption region for ZSM-22(173) and ZSM-22(207)

In addition, less ammonia molecules are adsorbed strongly on ZSM-22(173) than ZSM-22(207), evidenced by the greater weight loss of ZSM-22(207) catalyst at a temperature of ~413 °C.

Table 6.3 displays Si/Al ratio of the catalysts in the gel, determined using ICP-AES, determined using NH_3-TPD, and acidity investigated using NH_3-TPD. The catalysts were synthesized from the same synthesis gel, except that crystallization occurred in different autoclaves, and ICP-AES measurement showed that the catalysts have the same Si/Al ratios. However, NH_3-TPD analysis showed a slight variation in the Si/Al ratios of the samples. According to this measurement, the ZSM-22(173) catalyst showed a small amount of aluminum than the ZSM-22(207) catalyst. This could be as a result of part of the crystal not accessible for NH_3, or it could be due to some amorphous phase or lattice defects that can cause variation in adsorption of ammonia.

Table 6.3: Si/Al ratio of ZSM-22() and ZSM-22() catalysts, and their acidity determined using NH_3-TPD

catalyst	Si/Al gel	Si/Al-ICP	Si/Al-TPD	Acidity-TPD
ZSM-22(173)	45	30	45.9	0.35522
ZSM-22(207)	45	30	43.3	0.37542

The acidity measurement which is calculated based on the amount of ammonia desorbed (see Section 4.7) also showed that ZSM-22(173) desorbs a smaller amount of ammonia than ZSM-22(207). This observation is in agreement with the catalytic activity of the catalysts, ZSM-22(173) deactivated faster than ZSM-22(207) see Section 6.2.1. It is important to note that the acidity measurement in TPD is based on the amounts of ammonia desorbed from the catalysts, this means that if the pore of a given catalyst is easily accessible for ammonia, it will adsorb more ammonia giving rise to more acidity.

6.1.6 FTIR

The acidic property of ZSM-22(173) and ZSM-22(207) catalysts was investigated using FTIR. Figure 6.14 shows the OH stretching region for ZSM-22(173) and ZSM-22(207) catalysts before adsorption of CO and after saturation with CO. Before the adsorption of CO, two bands at ~3749 and at ~3604 cm^{-1} are observed, corresponding to the $\bar{\nu}$(OH) mode of isolated silanol and the $\bar{\nu}$(OH) mode of Brønsted acid sites respectively [64].

For both batches of catalysts, no band at ~3664 cm^{-1} associated with extra framework Al was observed. However there are differences that could possibly explain the difference in methanol conversion capacity of the catalysts. One noticeable difference is that, the ratio between the intensities of silanol to Brønsted bands of the catalysts is different. For the ZSM-22(173) catalyst, which has less methanol conversion capacity, this ratio is ~1.012, and for the ZSM-22(207) catalyst the ratio is ~0.875. Silanols are weak acid sites [65], this means that ZSM-22(173) has more weak acid sites than ZSM-22(207) catalyst. This could be the reason for the difference in the methanol conversion capacity of the catalysts.

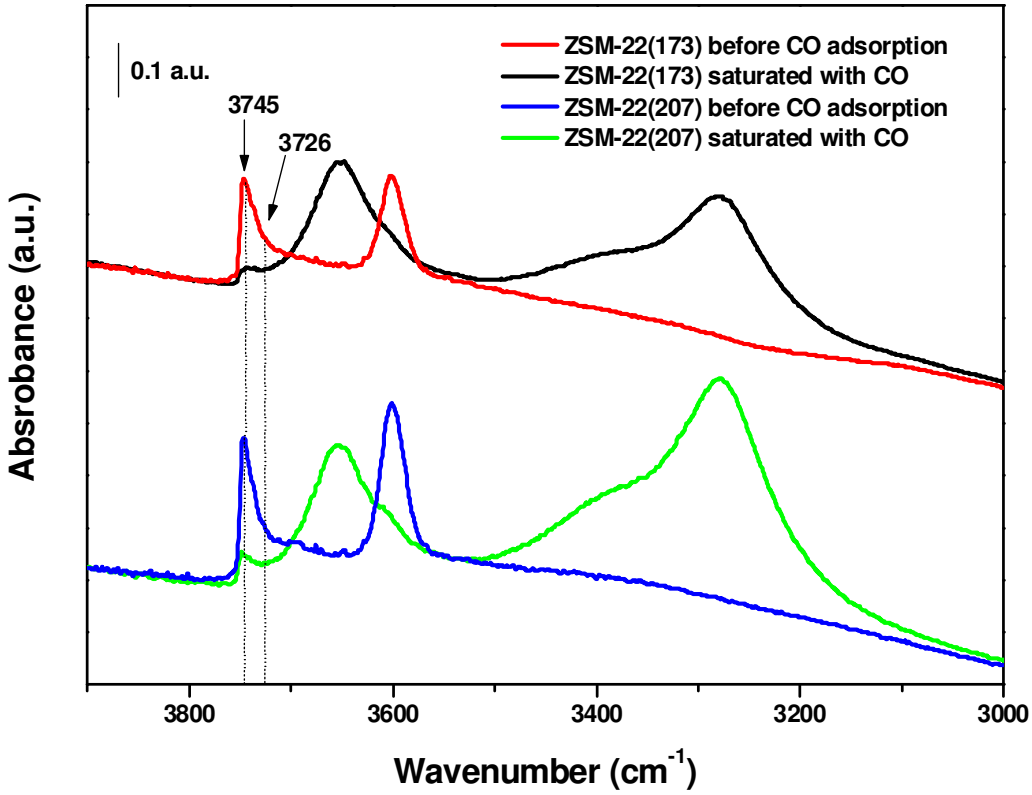

Figure 6.14: IR spectra in the OH region of ZSM-22(173) and ZSM-22(207) before adsorption of CO and after maximum saturation with CO.

Figure 6.15 and Figure 6.16 display the effects of CO adsorption of on the ZSM-22(173) and ZSM-22(207) catalysts. The bands at 3749 and 3604 cm^{-1} are gradually decreased and new bands at ~3651 and ~3282 cm^{-1} are observed. The observed shift in the position of the bands is due to the formation of hydrogen-bonded OH····CO species on Brønsted acid sites and isolated silanols, illustrated in Figure 6.17 a) and b). The value of frequency shift is a measure of the strength of the hydrogen bond [64]. The observed frequency shift ~320 cm^{-1}

for ZSM-22 catalysts (Table 6.4) indicates that the acid strength of ZSM-22 is comparable with acid strength of other known zeolites, a frequency shift ~307 cm^{-1} have been reported for ZSM-5 catalyst [66].

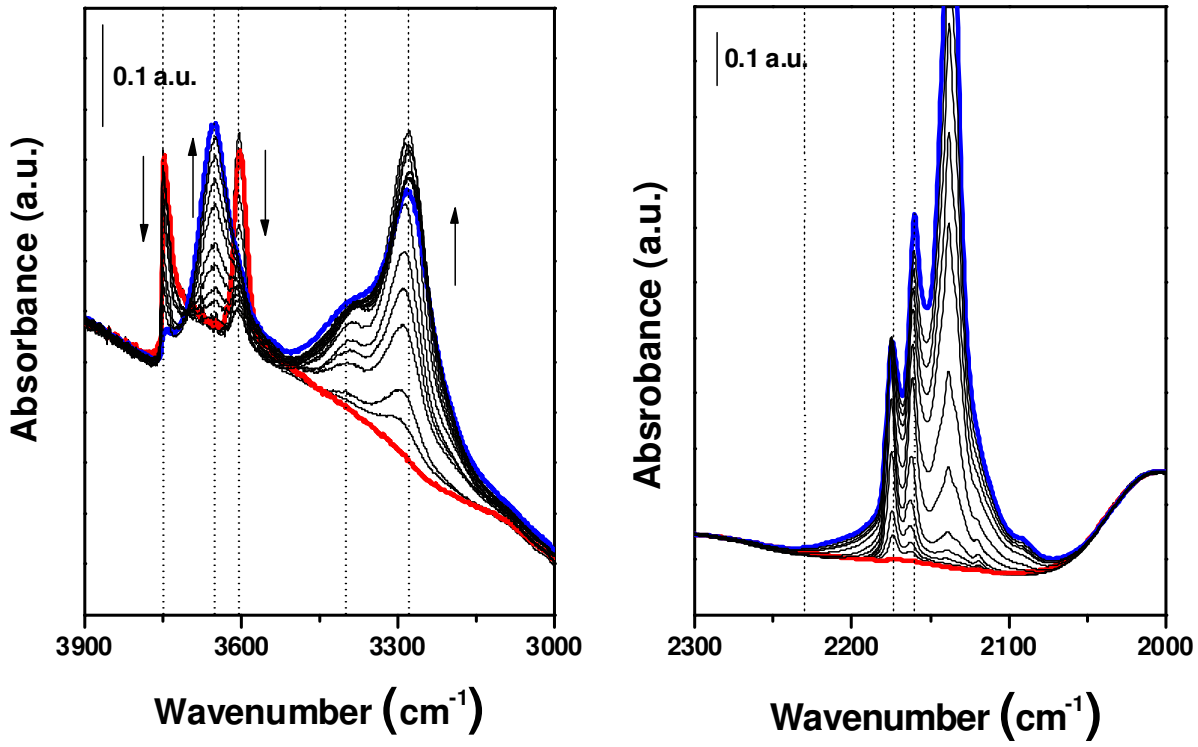

Figure 6.15: Adsorption of CO at 77K on ZSM-22(173) catalyst, IR spectra in the OH (right panel) and CO (left panel) stretching regions.

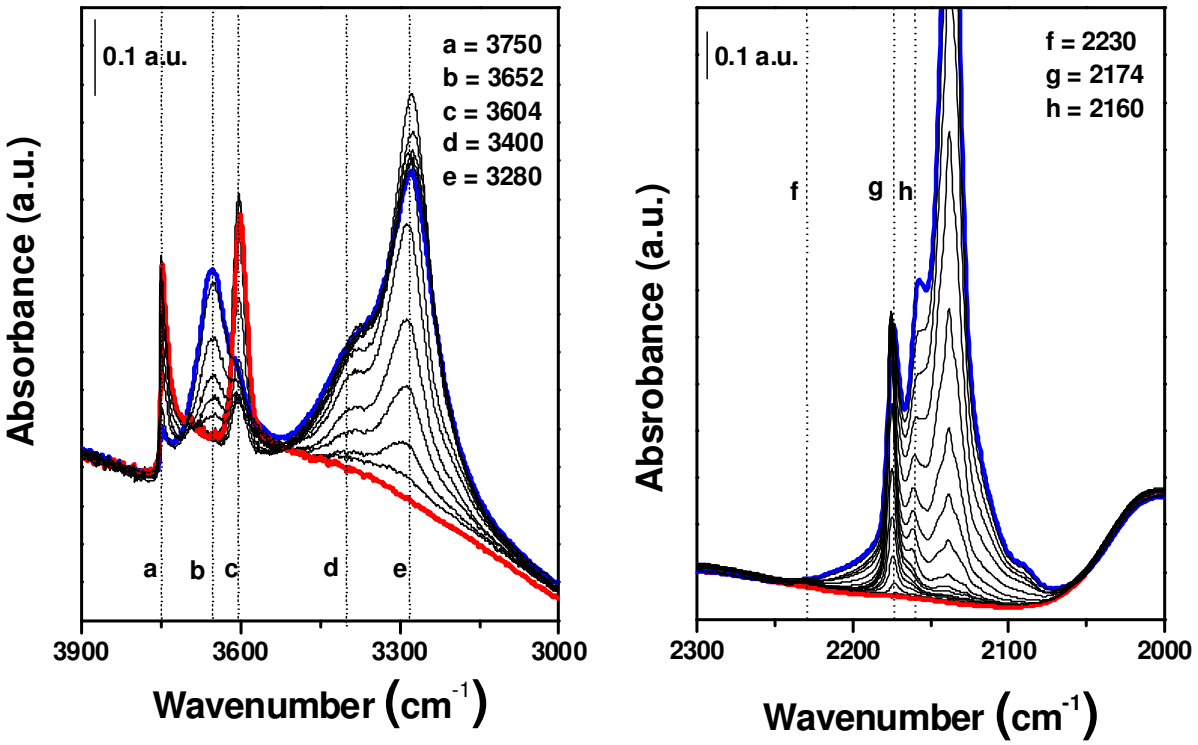

Figure 6.16: Adsorption of CO at 77K on ZSM-22(207) catalyst, IR spectra in the OH (right panel) and CO (left panel) stretching regions.

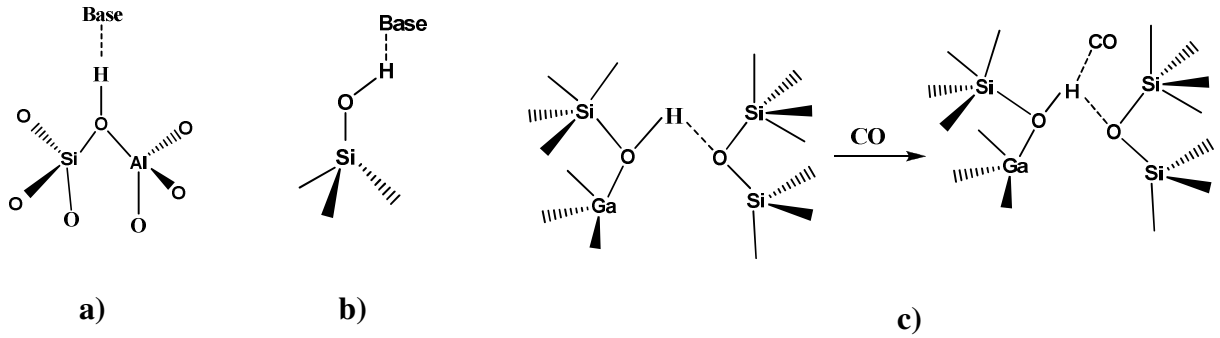

Figure 6.17 schematic illustration of adsorption of probe molecule on (a) Brønsted acid site, (b) isolated silanol, and hydrogen bonded interactions between bridged OH groups and oxygen atoms, and illustration for the interaction of Brønsted site with oxygen, illustration adopted from [67]

Table 6.4: shift (in cm^{-1}) of the OH and CO stretching mode of ZSM-22(173) and ZSM-22(207) catalysts, using CO as a probe molecule.

Catalyst	$\bar{\nu}$(OH)	$\bar{\nu}$(OH···CO)	$\Delta\bar{\nu}$(OH)	$\bar{\nu}$(CO)	$\bar{\nu}$(CO···OH)	$\Delta\bar{\nu}$(CO)
ZSM-22(173)	3604 cm^{-1}	3280 cm^{-1}	320 cm^{-1}	2138 cm^{-1}	2174 cm^{-1}	-22 cm^{-1}
ZSM-22(207)	3604 cm^{-1}	328o cm^{-1}	320 cm^{-1}	2138 cm^{-1}	2174 cm^{-1}	-22 cm^{-1}

As can be seen from Figure 6.15 (left panel) and Figure 6.16 (left panel), even substantial amount of CO does not deplete the 3604 cm^{-1} completely. This indicates that some of the Brønested sites are not accessed by the probe molecule. The same observation was reported for isostructural Theta-1 (TON) by using N_2 and CO as probe molecules [68], and a possible explanation has been given this material by taking into account the needle shaped crystals and the non-interacting unidirectional channels of the material. A remarkable fraction of the channels may be blocked by a relatively small amount of extra framework species in the channels, which can in turn isolate a sizable fraction of Brønsted sites from the probing molecules, as illustrated in Figure 6.18. The extra framework species in the channels could be unburned templates or cations. This observation is in agreement with the result obtained from TPD investigations, in which the slight variation in the Si/Al ratio was speculated to be a result of inaccessibility of part of the crystal for ammonia.

In addition to the already mentioned differences in the OH stretching regions of the catalysts before the adsorption of CO, two differences were observed after the adsorption of CO. These are (i) the shoulder of the band at ~3282 cm^{-1}, observed at ~3400 cm^{-1}, is broader for ZSM-22(173) catalyst than ZSM-22(207). (ii) the ratios between the intensity of silanol to Brønsted in CO stretching is also regions are different as in OH region, Table 6.5.

Catalyst	S/B* (OH)	S/B* (CO)
ZSM-22(173)	1.012	1.22
ZSM-22(207)	0.875	1.11

Table 6.5: ratio between intensity of silanol to Brønsted in the OH and CO stretching region. (* S/B = silanol to Brønsted ratio)

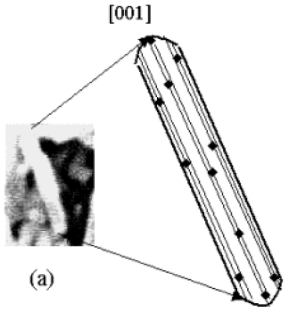

Figure 6.18: sketch of the blocking of monodimensional pores by extra framework debris (■). Illustration adopted from [68]

Apparently, the broadness and non symmetric nature of the band at ~3282 cm^{-1} indicates heterogeneity of Brønsted acid sites for both catalysts. Different interpretations have been given for the shoulder at ~3282 cm^{-1}, some of them are discussed here. FTIR study on desilicated ZSM-5 catalyst have reported the formation of extra lattice Al-OH groups upon NaOH treatment [46, 69], and the shoulder band at around 3450-3400 cm^{-1} was ascribed to OH groups of the extra framework aluminum. However, for both ZSM-22 catalysts no band was observed in the regions 3664 and 2220 cm^{-1} associated with extra framework aluminum. This indicates that there is no extra framework aluminum at a detectable lavel, in agreement with ^{27}Al-NMR. Thus, the solder band at ~3400 cm^{-1} may not be related to extra framework Al. Characterization of ZSM-5 zeolite by IR spectroscopy using N_2 and CO as probe molecules [67] showed that probing of the catalyst with CO resulted in asymmetric and broad band due to OH····CO adduct and probing with N_2 molecule resulted in nearly symmetric band due to OH····N_2. Moreover, N_2 was found to probe only a fraction of the Brønsted acid sites probed by CO. The result was rationalized by assuming hydrogen intersection between bridged OH groups and oxygen atom, as illustrated in Figure 6.17 c). Since N_2 is weaker base it will only probe isolated bridged OH groups giving rise to nearly symmetric band, but CO can probe both isolated and hydrogen bonded with oxygen OH groups giving rise to asymmetric and broad band [67]. Based on this statement, the observed differences in the methanol conversion capacity of ZSM-22 catalysts could be due to variation in the interaction of the Brønsted acid sites with oxygen atoms of the framework. Another alternative interpretation of the shoulder band at ~3282 cm^{-1} suggested heterogeneity of OH groups in the framework [70], this has been rationalized by assuming inhomogeneous distribution of Al^{3+}

ions in the framework. Obviously, inhomogeneous distribution of Al^{3+} ions will cause difference in local and nominal (average) Si/Al ratios, and this could lead to slight distortion and variation in TOT bond angle giving rise to variations in the Brønested acid site [70].

6.1.7 TGA

The as-made ZSM-22(173) catalyst showed ~10% weight loss during oxidation of the organic template, and after testing for 510 minutes on stream, the catalyst showed ~5% weight loss during coke oxidation. The amount of coke and organic template is comparable for other ZSM-22 catalyst batches.

6.2 Catalyst testing

6.2.1 Catalytic activity H-ZSM-22

As mentioned in Section 2.3, ZSM-22 has been reported as an inactive catalyst for the MTO reaction [39-42], ZSM-22 catalyst was reported as an inactive catalyst for the MTH reaction. Thus, it is worth showing that ZSM-22 has been investigated as an active catalyst for the MTH reaction using several batches of the catalyst. Figure 6.19 displays methanol conversion (%) as a function time on stream (TOS) for several batches of catalysts. The experiments were performed at 400 °C and WHSV = 2.05 $gg^{-1}h^{-1}$.

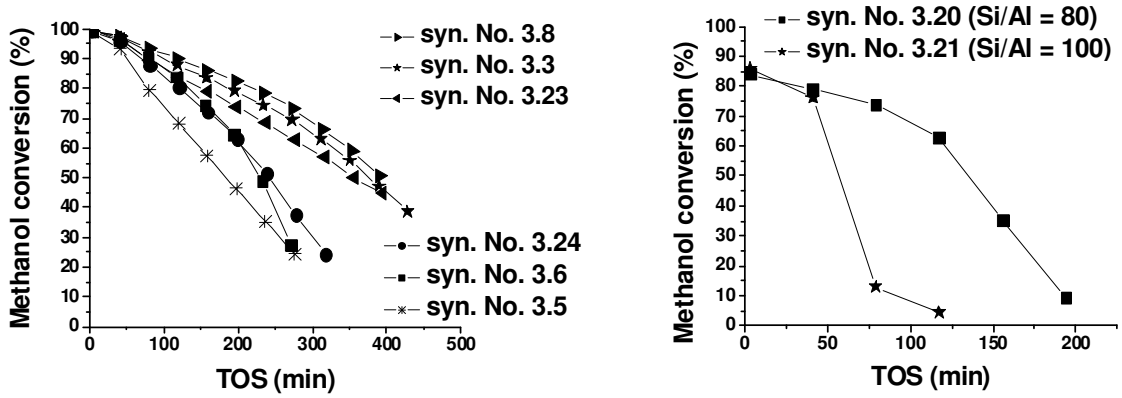

Figure 6.19 : **Methanol conversion (%) for several batches of catalysts as a function of TOS Si/Al = 30 (left panel) and Si/Al = 80 and 100 (right panel). Reaction carried out at 400 °C, WHSV = 2.05g $g^{-1}h^{-1}$.**

Figure 6.19 shows methanol conversion (%) as a function of TOS for ZSM-22 catalysts having Si/Al = 30 (left panel) and Si/Al = 80 and 100 (right panel). At suitable reaction conditions the catalyst converted appreciable amounts of methanol to hydrocarbons for several hours. This means that the previous conclusions [39-42] are not universally valid.

Clearly, the ZSM-22 catalysts having Si/Al = 30 fall in two groups of different conversion capacities (Figure 6.19 (left panel)). A representative ZSM-22 catalyst for each group was selected. Most of the catalyst testing results included in this report was performed using these representative ZSM-22 catalysts, the synthesis of the catalyst can be seen in Appendix 3 synthesis number 3.6 to 3.8. The catalysts having a BET surface areas 173 and 207 m^2g^{-1}, and denoted as ZSM-22(173) and ZSM-22(207) respectively. The product selectivities for these selected catalysts are presented in the following sections, selectivities for the other conversion covers in Figure 6.19 is presented in Appendix 6.

6.2.2 Catalyst life time

The application of a catalyst can be limited by its stability during the reaction. Coking is the major challenge in the MTH processes and the rate of coke formation varies among the various zeotype catalysts [12]. For the MTH reaction over zeolite and zeotype materials it has become clear that the reaction proceeds through active reaction centers trapped in the pores of the framework (see Section 2.1.1). The amount of trapped hydrocarbons increases with reaction time and eventually leads to the accumulation of coke, which causes catalyst deactivation. Thus, catalyst stability (life time) is an important parameter for its application.

The stability of the ZSM-22(173) catalyst towards deactivation was investigated at different reaction temperatures, WHSV = 2.05 $gg^{-1}h^{-1}$. Figure 6.20 (left panel) summarizes the percentage conversion of methanol to hydrocarbon at various reaction temperatures as a function of time on stream.

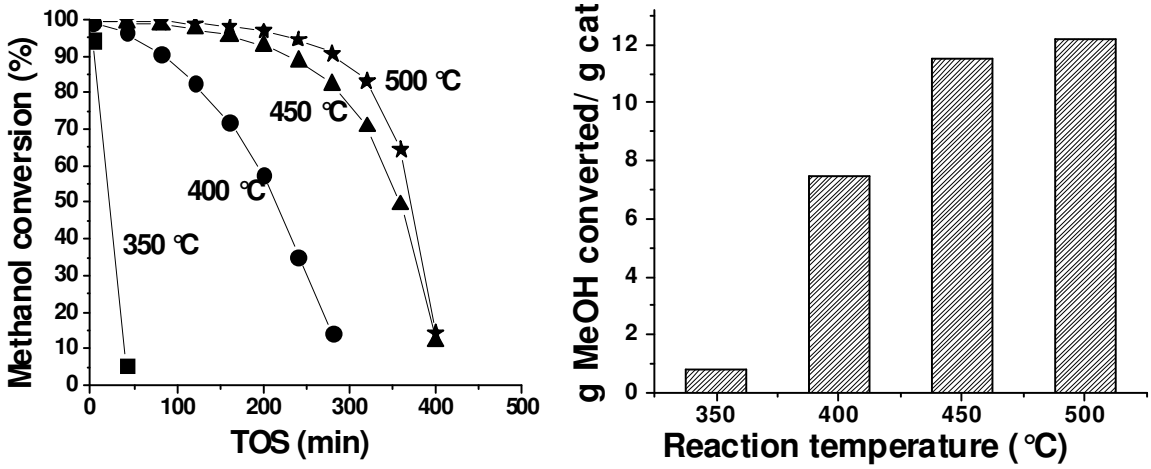

Figure 6.20: **Effect of temperature on the conversion of the methanol as a function of time on stream (left) and total amount of gram methanol converted/ gram catalyst before totally deactivated of the catalyst at various reaction temperatures. Reaction carried out over ZSM-22(173), WHSV = 2.05 $gg^{-1}h^{-1}$.**

At temperatures above 350 °C, the initial conversion is 100% and appreciable conversion is observed for several hours. Methanol conversion at 350 °C was 94% on the fresh catalyst and became 5.4% on the second sampling which was taken after 42 minutes on stream.

Figure 6.20 (right panel) displays total conversion capacity of ZSM-22(173) at different reaction temperatures. Total conversion capacity is defined as the total amount of methanol (in gram) that may be converted to hydrocarbon product per gram catalyst before complete deactivation [71, 72]. At 450 and 500 °C the total conversion capacities are ~12 gg^{-1}. Bleken et. al. [73] have studied the MTH reaction over SAPO-34 and SSZ-13 (the zeolite analogue) catalysts with an acid site density corresponding to Si/Al = 11, and found a maximum conversion capacity of ~25 gg^{-1}. Thus, if the difference in acid site concentration (a factor of 3) is considered, the amount of methanol converted to hydrocarbons over ZSM-22 catalyst is slightly larger than the amount of methanol converted over H-SAPO-34 and H-SSZ-13 per acid site before deactivation [73]. As mentioned in Section 6.2.1 catalysts having Si/Al = 30 fall in two groups of different conversion capacities and ZSM-22(173) is one of the catalysts that showed less conversion capacity. ZSM-22(207) catalyst which is in the group that showed longer displays even a higher conversion capacity (~12 gg^{-1}) than ZSM-22(173) (~7 gg^{-1}) at 400 °C (see Section 6.2.4, Figure 6.27), thereby outperforming SAPO-34 in this respect.

6.2.3 Product selectivity

Figure 6.21 to Figure 6.24 shows the product selectivities as a function of time on stream at reaction temperatures ranging from 350 to 500 °C, reaction carried over ZSM-22(173) catalyst.

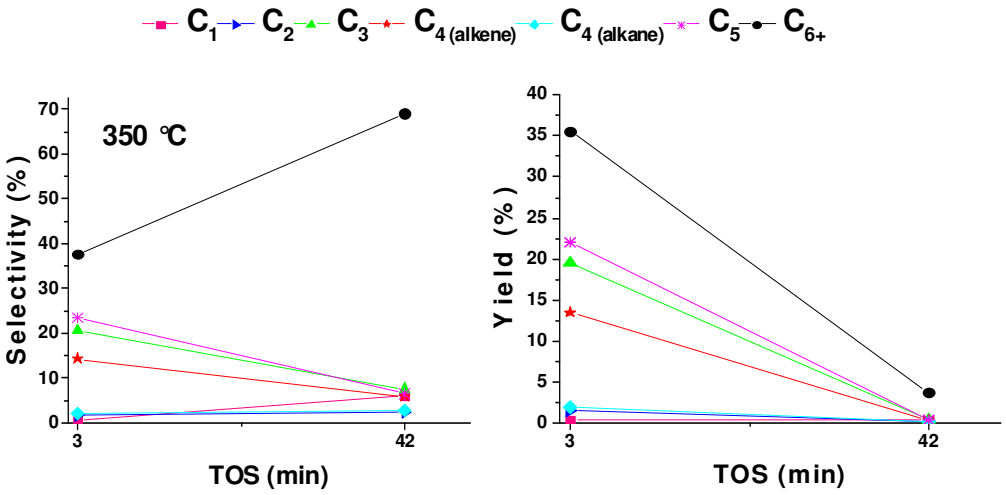

Figure 6.21 Product selectivity (left panel) and yield (right panel) at 350 °C, WHSV = 2.05 $gg^{-1}h^{-1}$ over ZSM-22(173) catalyst. Note the x-axis.

At 350 °C the selectivity for C_1 and C_{6+} increased with TOS, while the selectivities for the rest of the hydrocarbons (C_2-C_5) decreased with TOS. At 400 °C there was a noticeable decrease in C_3 selectivity, and slight decrease in C_1, C_2, C_4 and C_5 selectivities with progressive deactivation of the catalyst.

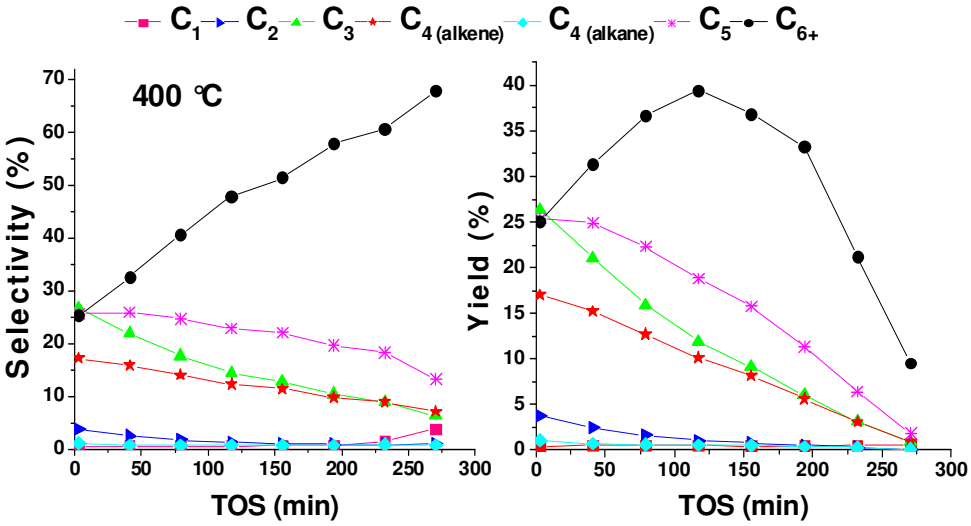

Figure 6.22 Product selectivity (left panel) and yield (right panel) at 400 °C, WHSV = 2.05 $gg^{-1}h^{-1}$ over ZSM-22(173) catalyst.

The product selectivity for C_{6+} fraction increased markedly with progressive deactivation of the catalyst. Note that the yield of C_{6+} fraction at 400 °C also increased for certain time non stream then started to decrease.

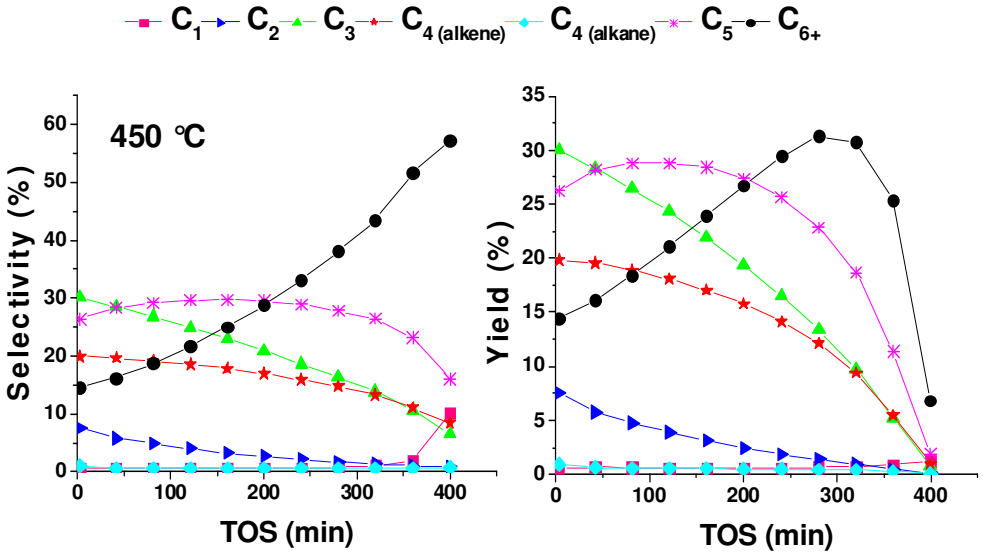

Figure 6.23 Product selectivity (left panel) and yield (right panel) at 450 °C, WHSV = 2.05 $gg^{-1}h^{-1}$ over ZSM-22(173) catalyst.

At 450 and 500 °C the observed selectivity and yield is different from the one observed at 400 °C. At 450 and 500 °C, in addition to the C_{6+} fraction the selectivity and yield for C_5 hydrocarbons also increases for certain time on stream before it starts decreasing.

Note that the initial selectivities over the fresh catalyst is affected by temperature. Increasing the reaction temperature resulted in an increase in the initial selectivities for light hydrocarbons (C_2-C_3, mainly C_3).

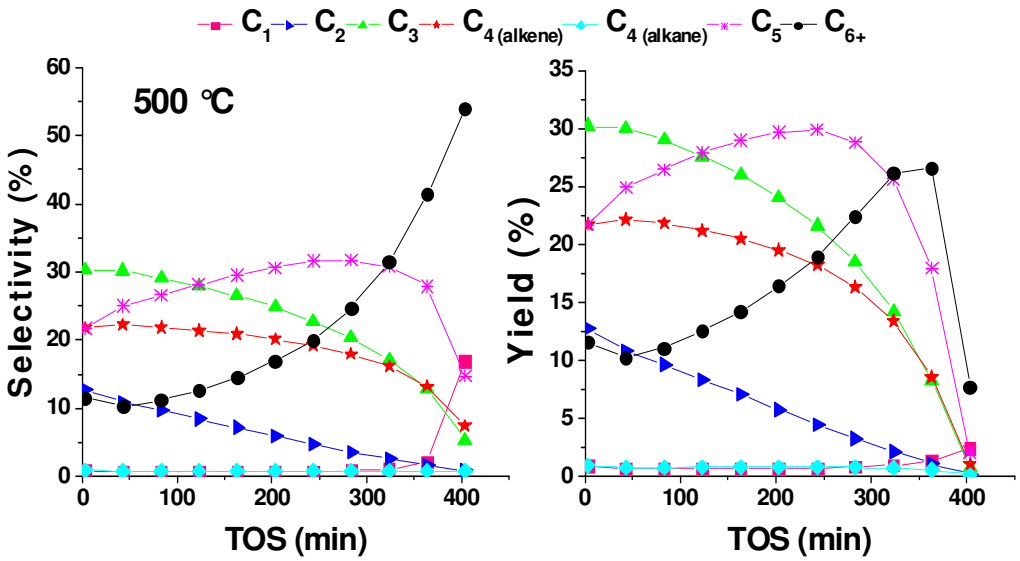

Figure 6.24: Product selectivity (left panel) and yield (right panel) at 500 °C, WHSV = 2.05 $gg^{-1}h^{-1}$ over ZSM-22(173) catalyst.

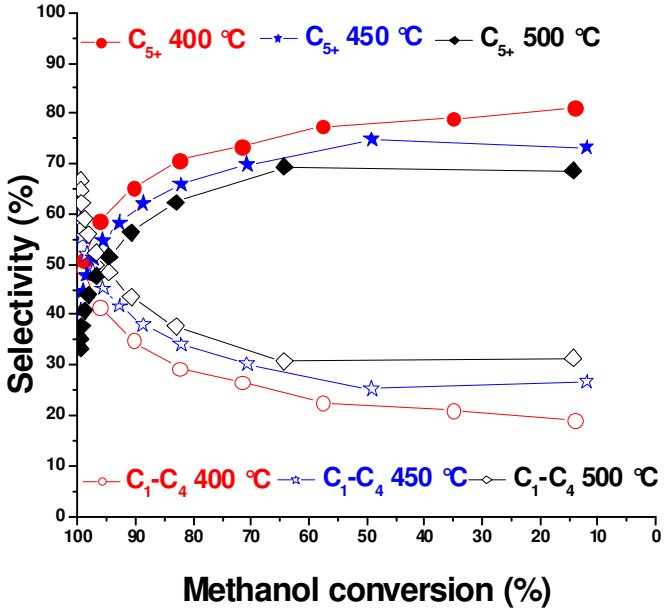

Figure 6.25: Product selectivity for C_1-C_4 hydrocarbons Vs. C_{5+} at different methanol convertions.

Figure 6.25 displays selectivities for lighter against heavier hydrocarbon fractions as a function of time on stream at different reaction temperatures. The product selectivity for C_{5+} hydrocarbons decreased with increasing reaction temperature. This shows that high temperatures favor the formation of lighter hydrocarbons.

Figure 6.26 shows product selectivity and yield for the ZSM-22(207) catalyst at 400 °C. The trend in both selectivity and yield of ZSM-22(207) catalyst is the same as that of ZSM-22(173) (Figure 6.22)

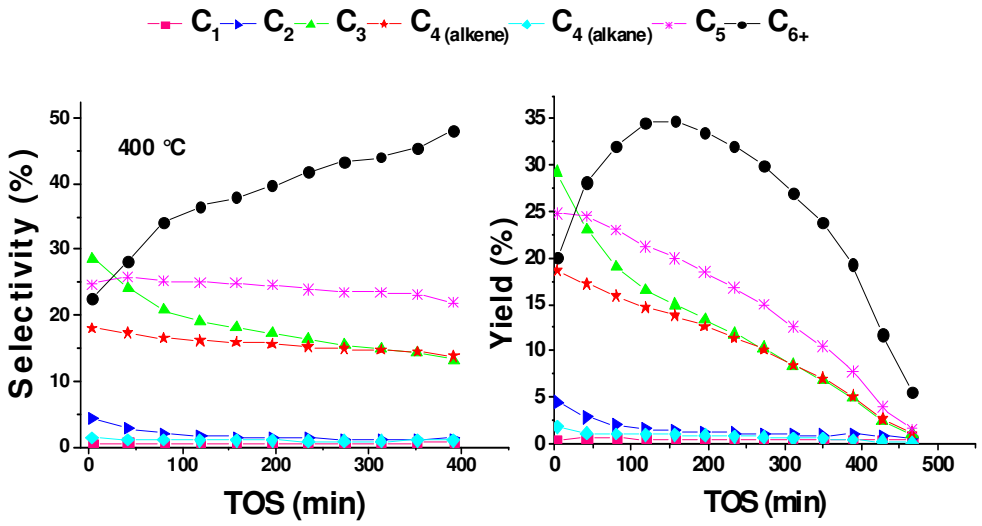

Figure 6.26: Methanol conversion/ product selectivity of ZSM-22(207) at 400 °C, WHSV = 2.05 $gg^{-1}h^{-1}$

6.2.4 Effect of methanol feed rate (contact time)

Figure 6.27 (left panel) displays the effect of feed rate on methanol conversion as a function of time on stream, over ZSM-22(207) catalyst. The feed rate was varied by adjusting the flow of the carrier gas (He). WHSV = 2.05, 3.03 and 4.05 $gg^{-1}h^{-1}$ were used for this investigation. These feed rates correspond to a contact time (1/WHSV) = 0.49, 0.33 and 0.25h respectively.

The catalysts were deactivated more rapidly with an increase in feed rates. Especially at a feed rate WHSV = 4.05 $gg^{-1}h^{-1}$, the methanol conversion dropped to less than 50% in about 40 minutes on stream compared to more than 70% conversion at a feed rate of WHSV = 2.05 $gg^{-1}h^{-1}$ after ~275 minutes on stream. Svelle et al. had investigated the methylation of alkenes over ZSM-5 catalyst using very high feed rates in which the hydrocarbon pool reactions responsible for methanol conversion were suppressed [36, 37].

It should be emphasized that at high feed rates in addition to hydrocarbon pool reactions, back diffusion of the product in the catalyst bed and complex secondary reactions may be suppressed Cui et al. studied MTO reaction over ZSM-22 at a high feed rate WHSV = 48 $gg^{-1}h^{-1}$ [41] which is probably high enough to suppress hydrocarbon pool formation and secondary reactions for this catalyst.

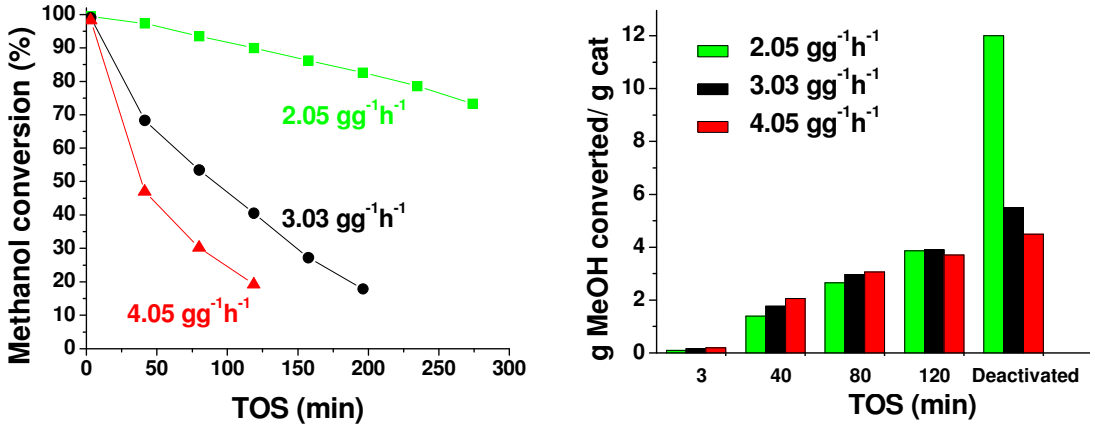

Figure 6.27 Methanol conversation as a function of TOS at different feed rates over ZSM-22(207) at 400 °C (left panel) and effect of feed rates on total amounts of gram methanol converted to products per gram of catalyst at different times on stream and before complete deactivation of the catalyst (right panel).

The total amount (gram) of methanol converted to hydrocarbon product per gram of catalyst during the first 2 hours is comparable in all the feed rates, as shown in Figure 6.27. However, the total amount (gram) of methanol converted to hydrocarbons before complete deactivation of the catalyst was remarkably decreased with increasing feed rate.

6.3 Detailed analysis of the composition of the product

Figure 6.28 displays the GC-MS Total ion chromatograms of effluent at various TOS. The effluent was mainly composed of hydrocarbons in the range C_3-C_{6+}. Very little amounts of C_2 and negligible amounts of aromatics were observed.

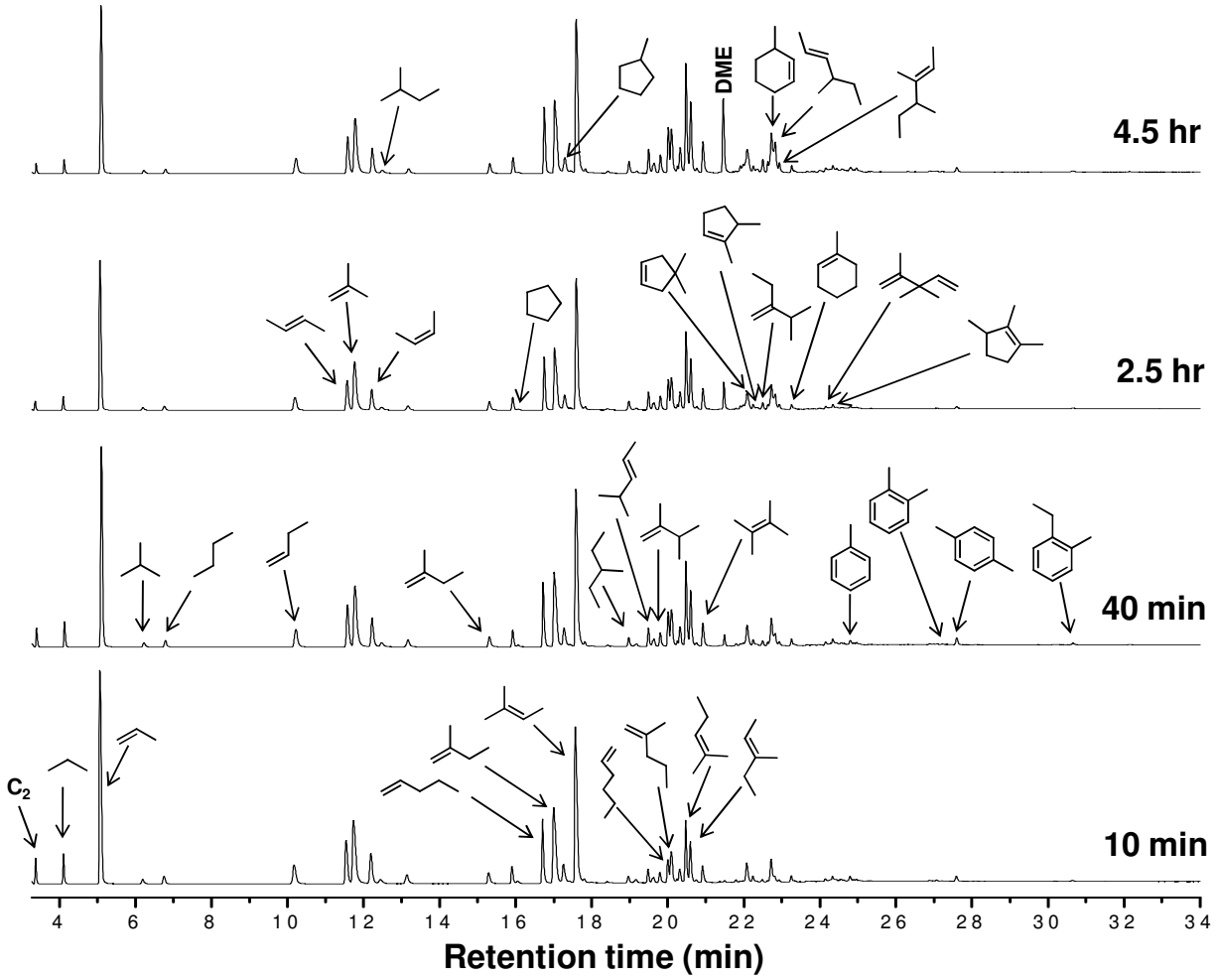

Figure 6.28: **GCMS total ion chromatogram of the effluent after different time on stream (TOS). The experiment was carried out at 400°C over ZSM-22(207). WHSV = 2.05 $gg^{-1}h^{-1}$.**

The product spectrum of the MTH reaction over ZSM-22 is intermediate between to those found in MTO (mainly ethene and propene over SAPO-34 catalyst) and MTG (aromatic rich product spectrum over ZSM-5 catalyst). Brown et al. [74] and Haw et al. [75] have reported similar product spectrum for ZSM-48 and FER (H-Ferrierite) zeolites respectively. Both these zeolties have 10-ring non-interacting channels. Thus, the observed product spectrum can be

ascribed to the unique shape selectivity induced by the non-interacting 10-rings of the zeolites.

As can be seen from Figure 6.29 (right panel), the catalyst showed appreciable selectivities for both light olefins (C_1-C_4, MTO) and gasoline (C_{5+}, MTG) fraction. In the following sections the composition these fractions is presented.

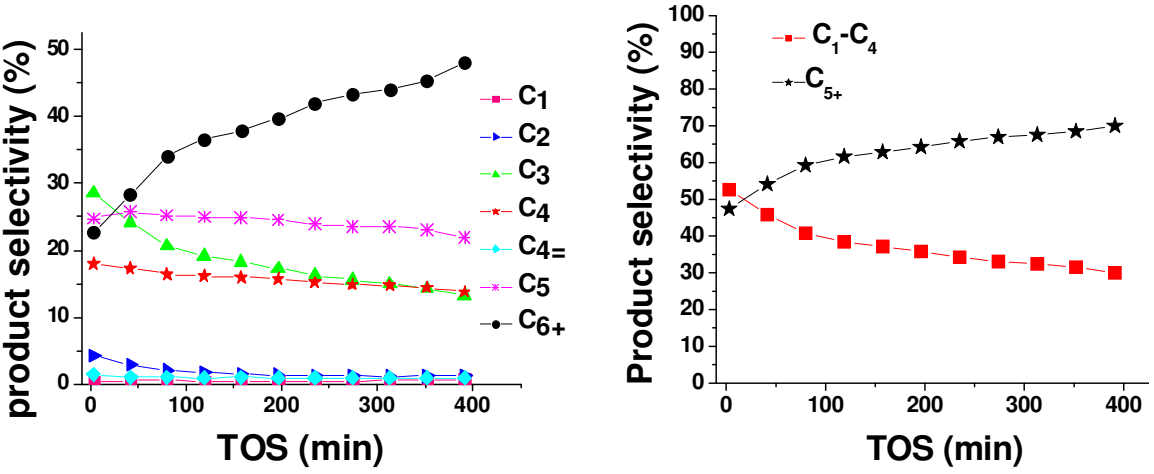

Figure 6.29: **Product selectivity as a function of TOS for various hydrocarbons (left) and selectivity for light products (C_1-C_4) versus C_{5+} (right). Reaction carried out at 400 °C over ZSM-22(207), WHSV = 2.05 $gg^{l}h^{l}$.**

6.3.1 Composition of C_1-C_4 fraction

Table 6.6 presents composition (%) of C_1-C_4 fraction. C_3 (mainly propene, see Figure 6.28) was the most abundant in this fraction. Isobutene and trans-butene were the second and third abundant species. Note that the amount of alkanes in the fraction is very small.

Table 6.6: Composition of C_1-C_4 fraction as a function of time on stream, experiment was carried out at 400 °C over ZSM-22(207), WHSV = 2.05 $gg^{-1}h^{-1}$.

TOS (min)	C_1	C_2	C_3	C_4 alkanes	C_4 alkenes
3	0.7	8.1	53.6	3.3	34.1
42	1.2	6.3	51.6	2.4	38.4
120	1.3	4.6	48.3	2.9	42.9
234	1.4	4.4	46.4	3.0	44.8
350	2.1	5.6	44.1	3.1	45.0
438	3.2	8.2	41.7	3.2	43.7
500	5.8	12.7	37.5	3.8	40.3

6.3.2 Composition of C_{5+} fraction

The catalyst showed high selectivity for C_{5+} hydrocarbons. This fraction of hydrocarbon is in the acceptable range for the production of gasoline fuel [76]. The C_{5+} fraction is closely inspected and the composition is presented in Table 6.7.

Table 6.7 Composition of C_{5+} fraction as a function of time on stream , experiment was carried out at 400 °C over ZSM-22(207),WHSV = 2.05 $gg^{-1}h^{-1}$.

TOS		Alkanes (C%)			Alkenes (C%)		Aromatics
(hour)	Linear	Branched	Cyclic	Linear	Branched	Cyclic	(C%)
0.08	0.40	1.93	5.16	10.83	70.21	10.10	1.36
0.67	0.33	1.86	3.81	11.48	71.23	9.55	1.75
1.55	0.34	1.79	3.36	11.68	73.59	8.39	0.84
2.50	0.31	1.88	3.40	11.46	73.18	8.93	0.84
3.50	0.33	1.66	3.20	11.73	72.92	9.04	1.11
4.50	0.28	1.68	2.94	11.53	72.99	9.79	0.80

C_{5+} Alkanes

Alkanes constituted between ~5-7.5% of the C_{5+} fraction. Cyclic alkanes were the most abundant, branched and linear alkanes were the second and third most abundant species respectively. The percentage amount of cyclic alkanes decreases with progressive deactivation of the catalyst (from ~5% to ~3%). Very small amounts of branched and linear alkanes were observed, on average ~1.8 and ~0.3% respectively. There was no remarkable change in the amounts of branched and linear alkenes with catalyst deactivation.

C_{5+} Alkenes and aromatics

Alkenes are the most abundant in the C_{5+} fraction, constituting 91-94% of the fraction. Branched alkenes were the most abundant (~72%) followed by linear (~11%) and cyclic (~9%) alkenes. There was no remarkable change in alkene selectivities with TOS. Interestingly, very little aromatics (~1%) were observed, and there was no remarkable change in aromatic selectivities with TOS.

The high selectivity for C_{5+} fraction especially for branched hydrocarbons could be used as a valuable product. Since the late 1980's [76] current and future developments in oil refining have been mainly concerned to develop cleaner products [76-78]. Concerns about air quality and pollution involves careful control of the chemical composition of fuels, unburned hydrocarbons and other pollutants [77]. The environmentally most favorable gasoline consists of highly branched alkanes with mainly five to ten carbon atoms, and there are limits on aromatic contents [76]. The ZSM-22 MTH product meets these requirements and might be used for the production of low-aromatic gasoline after hydrogenation. Alternatively, the alkene rich product might be utilized as an alkylation feedstock, where it is further reacted with other alkanes to form higher branched alkanes. In this case hydrogenation is not required.

6.4 Retained hydrocarbons

6.4.1 Qualitative analysis

Figure 6.30 displays the Total ion chromatogram obtained for a series of ZSM-22(207) catalysts after various methanol reaction times 400 °C. In the first few minutes of methanol reaction, dimethylbenzene and trimethylbenzene were the dominant retained hydrocarbons but as the time on stream was increased methylnaphthalene became the most abundant species.

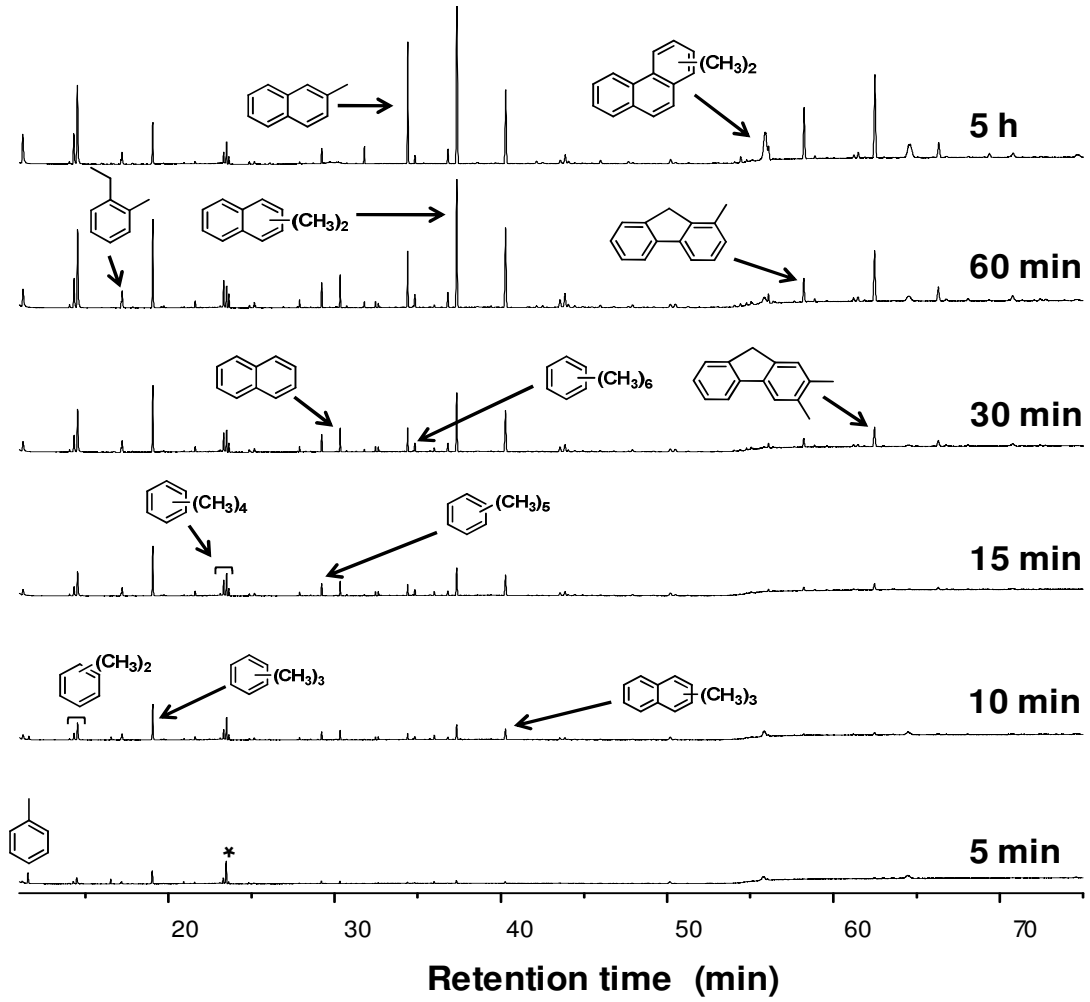

Figure 6.30: **GC-MS total ion chromatogram of hydrocarbon extracts at different time on stream. Reaction carried out at 400 °C over ZSM-22(207). Flow of methanol (WHSV) = 2.05 gg^{-1} h^{-1}. (NB: all the peaks are normalized with the standard peak indicated by * in the chromatogram, HP-Inno vax column is used)**

Polymethylbenzenes as small as trimethylbenzene are linked to alkene formation [79]. The presence of these organic indicates that hydrocarbon pool reaction mechanism is operative over the ZSM-22 catalyst. Small amounts of ethylbenzene and ethyltoluene were also observed. This is may be related to intermediates in the synthesis of ethene, although

ehtylbenzenes could also from by back reaction of ethylene with aromatics [80]. The retained hydrocarbons can sustain alkene formation. Once alkenes are produced, they can undergo further methylation and cracking, leading to net methanol conversion, and also to coking reactions [33, 34].

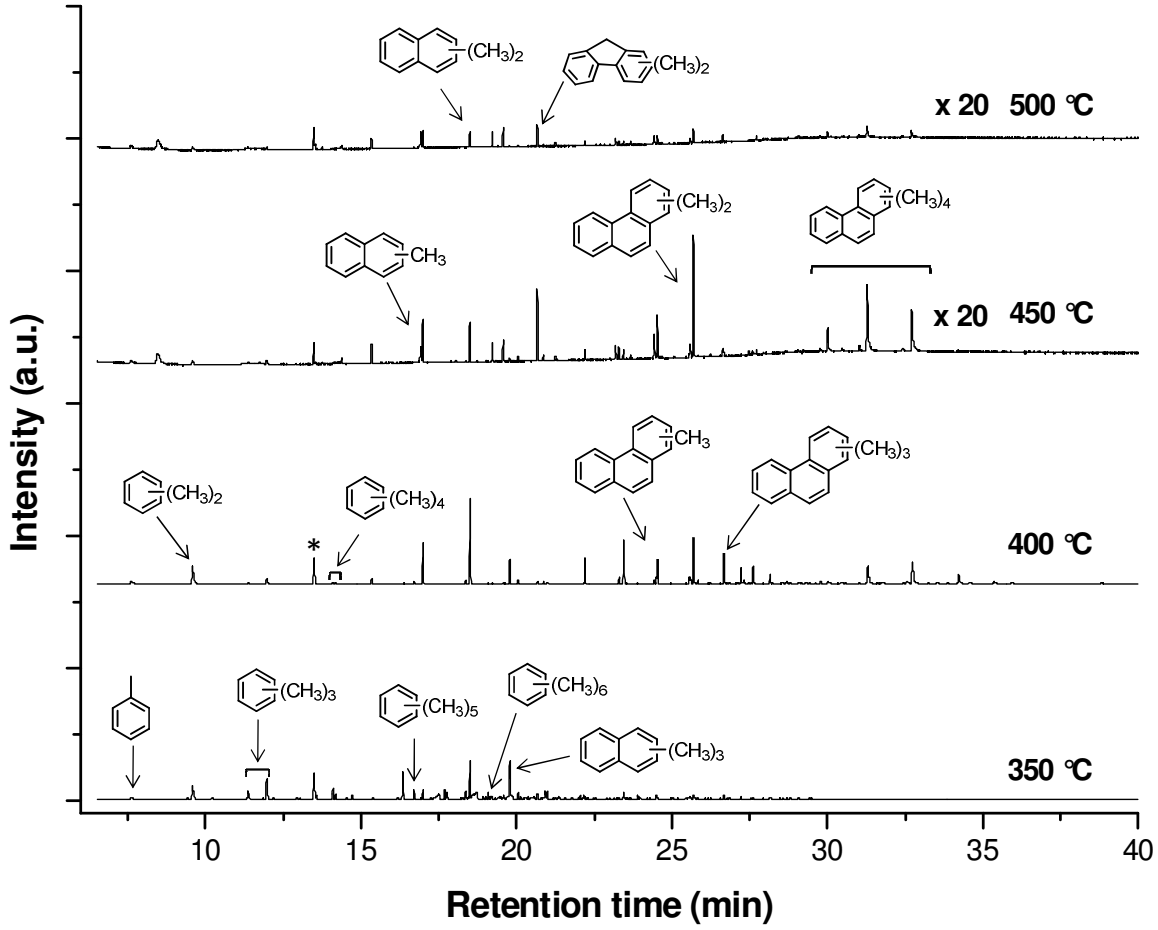

Figure 6.31: **GC-MS total ion chromatogram of hydrocarbon extracts of deactivated catalyst at at 350, 400, 450 and 500 °C, the catalysts were dissolved after 75, 550, 550, and 550 minutes of methanol reaction. Reaction carried out at 400 °C over ZSM-22(173). Flow of methanol (WHSV) = 2.05 gg^{-1} h^{-1}. (the standard peak C_2Cl_6 is indicated by * in the chromatogram, HP-5MS column is used)**

Figure 6.31 displays retained hydrocarbons in the deactivated ZSM-22(173) catalyst at different reaction temperatures. Note that, all the intensities are normalized to the standard C_2Cl_6 peak, and the Total ion chromatogram of the catalysts deactivated at 450 and 500 °C are 20 times magnified. The catalyst deactivated at 350 °C was under methanol flow for 75 minutes on stream, the catalysts deactivated at 400, 450, and 500 °C were under methanol flow for, 550, 540, and 550 minutes on stream respectively.

Coke selectivity for slim hydrocarbons was observed, especially at lower reaction temperatures. This finding agrees well with the pore geometry of ZSM-22, evidenced by the absence of pyrene which must be too big to fit into the channels. Clearly, the coke selectivity shifts towards heavier hydrocarbons with increasing reaction temperature. The catalysts had different colors when deactivated, at 350 °C gray, at 400 °C dark green and at 450 and 500 °C black. The catalyst deactivated at 450 and 500 °C had very little amounts of detectable hydrocarbons (note the magnification). This could mean that the coke is mainly graphitic species, deactivation due to graphitic coke has been reported for ZSM-5 catalyst [35]. It is likely that deactivation has occurred when unidirectional narrow parallel pores of the material were filled with the mentioned slim retained hydrocarbons, making the sites inaccessible by the incoming methanol molecules. It could also due to graphitic coke deposited on the external surface of the crystal, as it is observed for other zeolites.

6.4.2 Indications for the residing of organics in the channels of ZSM-22

Because ZSM-22 was reported as an inactive catalyst for the MTH reaction due to its narrow channels, and some of the retained hydrocarbons displayed in Figure 6.30 and Figure 6.31 seemed to be bigger than the pore size of ZSM-22 catalyst, we thought that the reaction might have occurred on the external surface of the catalyst. One approach to investigate external surface reactions was to see if there are any removable retained hydrocarbons on the external surface of the catalyst after methanol conversion.

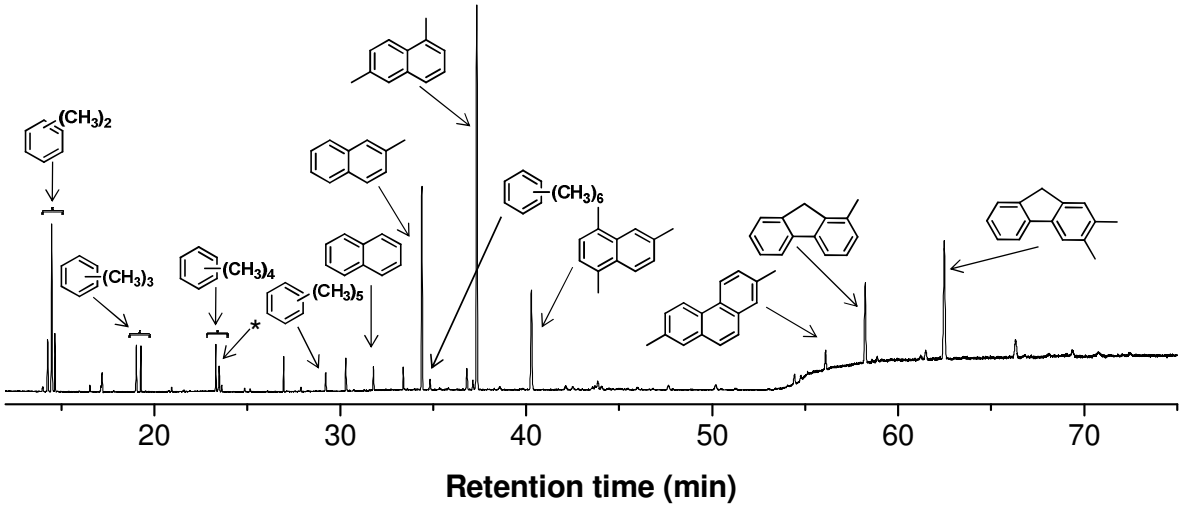

Figure 6.32: **GC-MS total ion chromatogram of hydrocarbon extract of washed catalyst. The experiment was carried out at 400 °C over ZSM-22(207). Flow of methanol (WHSV) = 2.05 gg^{-1} h^{-1}. (the standard peak C_2Cl_6 is indicated by * in the chromatogram, HP-Inno vax column is used)**

As mentioned in section 5.3.2, the spent catalysts were washed thoroughly and both the washing (CH_2Cl_2) and the catalysts (after washing) were analyzed using GC-MS. Analysis of the washing (CH_2Cl_2) using GC-MS showed that no removable hydrocarbons (by washing) were present on the surface of the catalyst. Figure 6.32 displays the Total ion chromatogram of ZSM-22 catalyst after washing its external surface with CH_2Cl_2. All the hydrocarbons including hexaMB were found to be retained in the catalyst after the washing. This is one indication that the catalytic reactions had occurred in the channel of ZSM-22 and as a result of this the hydrocarbons were retained in the channels.

The effect of the residing of hydrocarbons in the channels of ZSM-22 on the crystallinity of the material was studied using XRD. Capillary X-ray diffractograms were recorded for the catalysts after feeding methanol for various times, displayed in Figure 6.33. Clearly, crystallinity of the catalyst is retained. The low angle (2θ) reflection peak intensities were decreased slightly as a function of TOS, indicated by the numbers on the diffractogram.

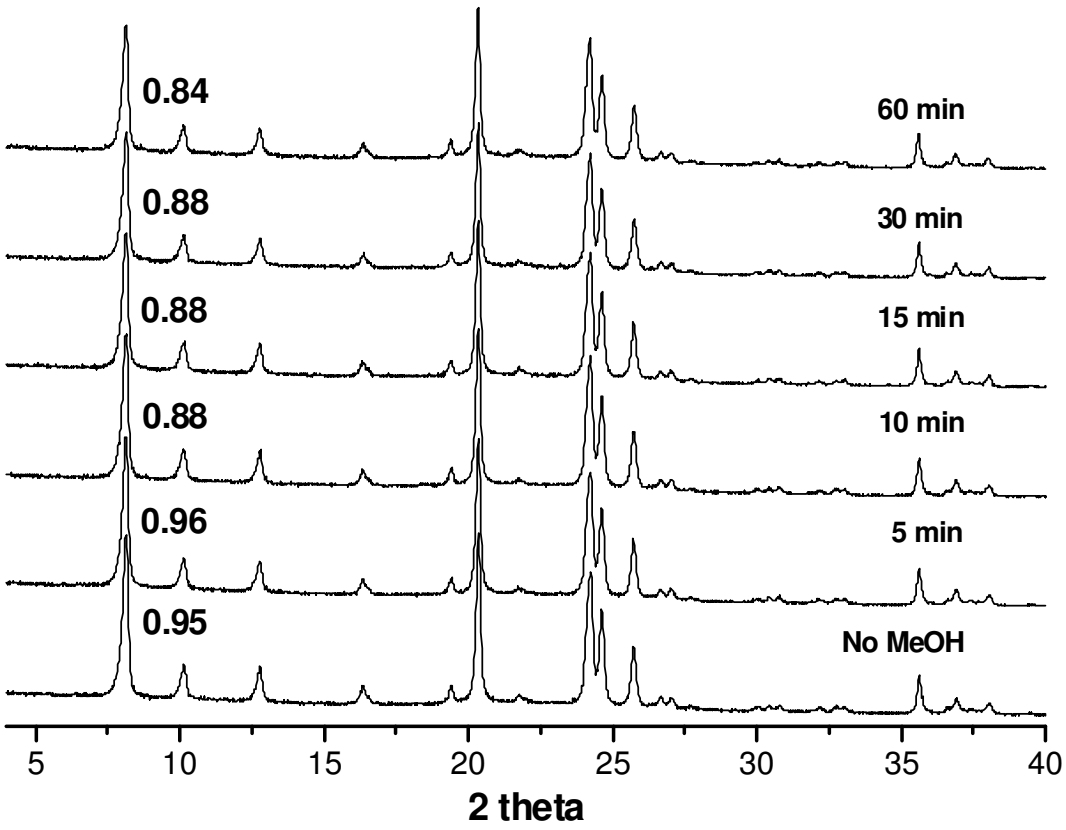

Figure 6.33: **capillary XRD profile of ZSM-22(207) after methanol feed for various times at 400 °C. WHSV = 2.05 $gg^{-1}h^{-1+}$. The numbers are the ratios between the reflection at ~7 and ~20 °**

For zeolites, the low angle reflection intensities are particularly sensitive to non framework species in the pores, whereas the high angle reflection intensities are determined primarily by the atoms of the framework [50]. Thus the slight decrease in low angle intensities can be explained by the formation of hydrocarbons in the channels of the catalyst.

From both surface washing experiment and XRD findings, it is clear that the hydrocarbons are retained in the channels of ZSM-22. Keeping in mind the flexibility of molecules and the breathing motion of zeolites at high temperature, there could be possibilities for the adsorption of hydrocarbons which seemed to be bigger than the channels of ZSM-22 inside the channels. The hydrocarbons could be adsorbed at the pore openings or at crystal defects.

6.4.3 Quantitative analysis

The retained hydrocarbons were quantified and the result is presented in Table 6.8.

Table 6.8 concentrations of retained hydrocarbons per acid sties and unit cells as a function of time one stream.

TOS	[mol] of HC / mol acid site	One hydrocarbon per	One hydrocarbon per
5 min	4.7×10^{-3}	214 acid sites	171 unit cells
10 min	14.1×10^{-3}	71 acid sites	57 unit cells
15 min	20.0×10^{-3}	50 acid sites	40 unit cells
30 min	30.3×10^{-3}	33 acid sites	26 unit cells
60 min	62.5×10^{-3}	16 acid sites	13 unit cells
300 min	90.9×10^{-3}	11 acid sites	9 unit cells

As can be seen from Table 6.8, after 300 minutes on stream the catalyst had one retained hydrocarbon per 9 unit cells. Along the crystallographic *c-axis* (unit cell of ZSM-22 is displayed in Figure 6.34), 9 unit cells are ~45 Å in length. There are two channels per unit cell, this means that ~45 Å unit cell length corresponds to ~90 Å channel length. From these relations it is clear that the distance between the retained hydrocarbons is ~90 Å.

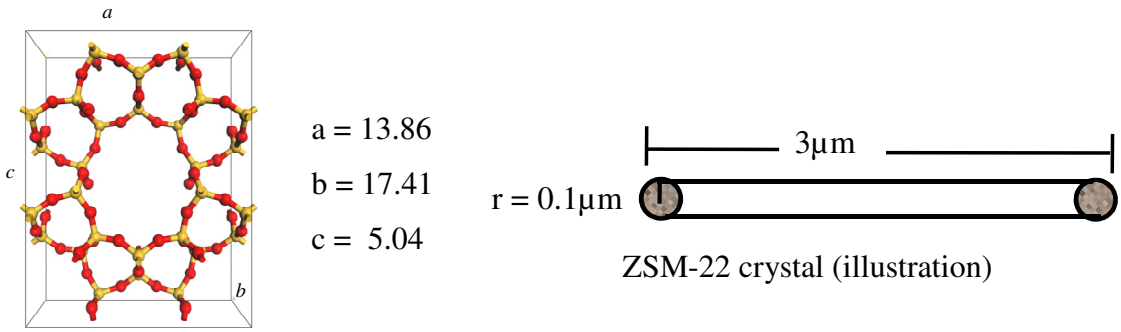

Figure 6.34 ZSM-22 unit cell and illustration of the crystal used for calculations

From the length of the crystal (3µm = 30000 Å) (Figure 6.34) and the distance between the retained hydrocarbons ~90 Å it was found that there were ~333 molecules in a channels of ZSM-22. Note that it was assumed that all the hydrocarbons were retained in the channels, the assumption was based on the external surface washing experiment presented in Section 6.4.2.

To calculate the number of retained hydrocarbons in a crystal of ZSM-22, the crystal was assumed to be cylindrical in shape having 0.1µm radius and 3µm length, which gave an area of 3.14 x 10^6 $Å^2$. This area corresponds to the area of ~13 x 10^3 unit cells (the area of a unit cell a product of *a*- and *b axis* = 242 $Å^2$). This means that there are ~26 x 10^3 channels in a crystal (one unit cell = two 10-ring channels). As mentioned above, each channel had ~333 molecules meaning that there were ~8.64 x 10^6 molecules a crystal of ZSM-22.

The important finding in this quantification of the retained hydrocarbons is that, the channel is found to contain a large number of retained hydrocarbons, which is in agreement with the decrease in low angel reflections observed in XRD. If the channels were too narrow to accommodate the hydrocarbon pool species, the quantification could have resulted in small number of retained hydrocarbon per channel, as small as 2 retained hydrocarbons per channel one at each pore opening.

From the surface washing experiment, XRD results and the quantification, it can be concluded that the hydrocarbon pool species are residing in the channels of ZSM-22 catalyst.

6.5 Desilication

As mentioned in Section 3.3, two bathes of ZSM-22 catalyst were subjected to post synthesis treatment, PARENT-1 and PARENT-2 catalysts. Figure 6.35 displays the XRD diffraction patterns of the catalysts. PARENT-1 refers to ZSM-22 catalyst synthesized according to append Appendix 3 synthesis number 1.7. PARENT-2 is not a single batch, several batches of ZSM-22 catalyst synthesized in a same way as that of PARENT-1 were mixed to form large batch. This large batch is denoted as, and it has small amount of structural impurities ZSM-5 and cristobalite, indicated by '*' and '+' in the diffraction pattern respectively.

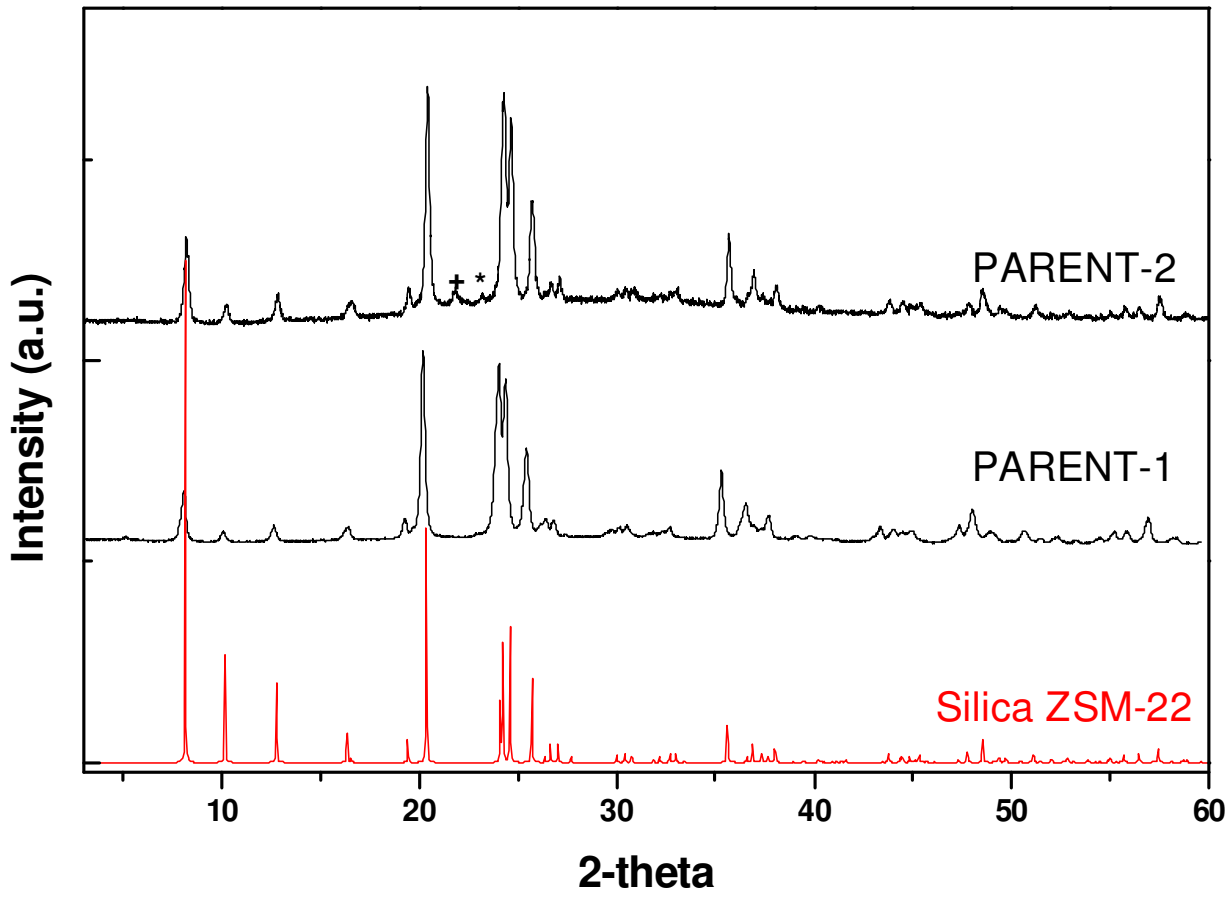

Figure 6.35 X-ray diffractograms of PARENT-1 and PARENT-2 catalyst, the amorphous baseline for PARENT-2 catalyst is due to glass sample cells used during XRD analysis.

6.5.1 Characterization

Characterization PARENT-1 catalyst

The pH of the NaOH solution was measured during the treatment. For the 0.05M NaOH solution the pH was 13.1 and it deceased to 9.7 upon treating the zeolite. For the 0.2M and 0.5M NaOH solutions the initial pH was 13.6 and 13.9, and it deceased to 13.1 and 13.6 upon treating the zeolite respectively.

Table 6.9 displays the treatment conditions used during desilication process and the resulting weight loss of PARENT-1 catalyst. There was a considerable weight loss upon the treatment, and the weight loss increases with the severity of the treatment and reaches 47% for the sample treated with 0.5M NaOH solution. The BET surface area of the PARENT-1 sample is considerably low in comparison with other ZSM-22 catalyst batches. The PARENT-1 sample was in a good crystallinity and no unreacted amorphous phase was observed in XRD, evidenced by a flat base line in the diffractogram, Figure 6.35. This batch of catalyst was synthesized form an identical gel as that of ZSM-22(173) and ZSM-22(207) catalysts, except crystallization occurred in a different autoclave. The reason for its very low surface area is unclear.

Table 6.9: NaOH treatment conditions, weight loss, and BET surface area of PARENT-1 catalyst before and after alkali treatment at different concentrations.

Sample	Treated with	T °C	Time	Weight loss(%)	BET (m^2/g)
PARENT-1	-	-	-	-	96
PARENT-1-0.05M	1.5 mmol NaOH /g	75	30 min	34	177
PARENT-1-0.2M	6 mmol NaOH /g	75	30 min	39	229
PARENT-1-0.5M	15 mmol NaOH /g	75	30 min	47	257

Appreciable increase in BET surface area was observed upon alkali treatment. The most severely treated sample (PARENT-1-0.5M) has the highest surface area = 257 m^2/g, it is important to note that this is the highest surface area obtained in this thesis. The surface area of TON framework was calculated theoretically by simulating the adsorption of nitrogen over the framework and a surface area of 230 m^2/g was obtained. This means that the surface area

obtained after desilication of PARENT-1 using 0.5M NaOH is slightly higher than the simulated surface area.

The isotherms obtained were typical for micropous materials (Figure 6.36), mesopore distribution BJH plot is presented in Appendix 6. For ZSM-5 catalyst, it was reported that alkali treatment of the catalyst resulted in an increase in surface area of the catalyst and formation of mesopores [46].

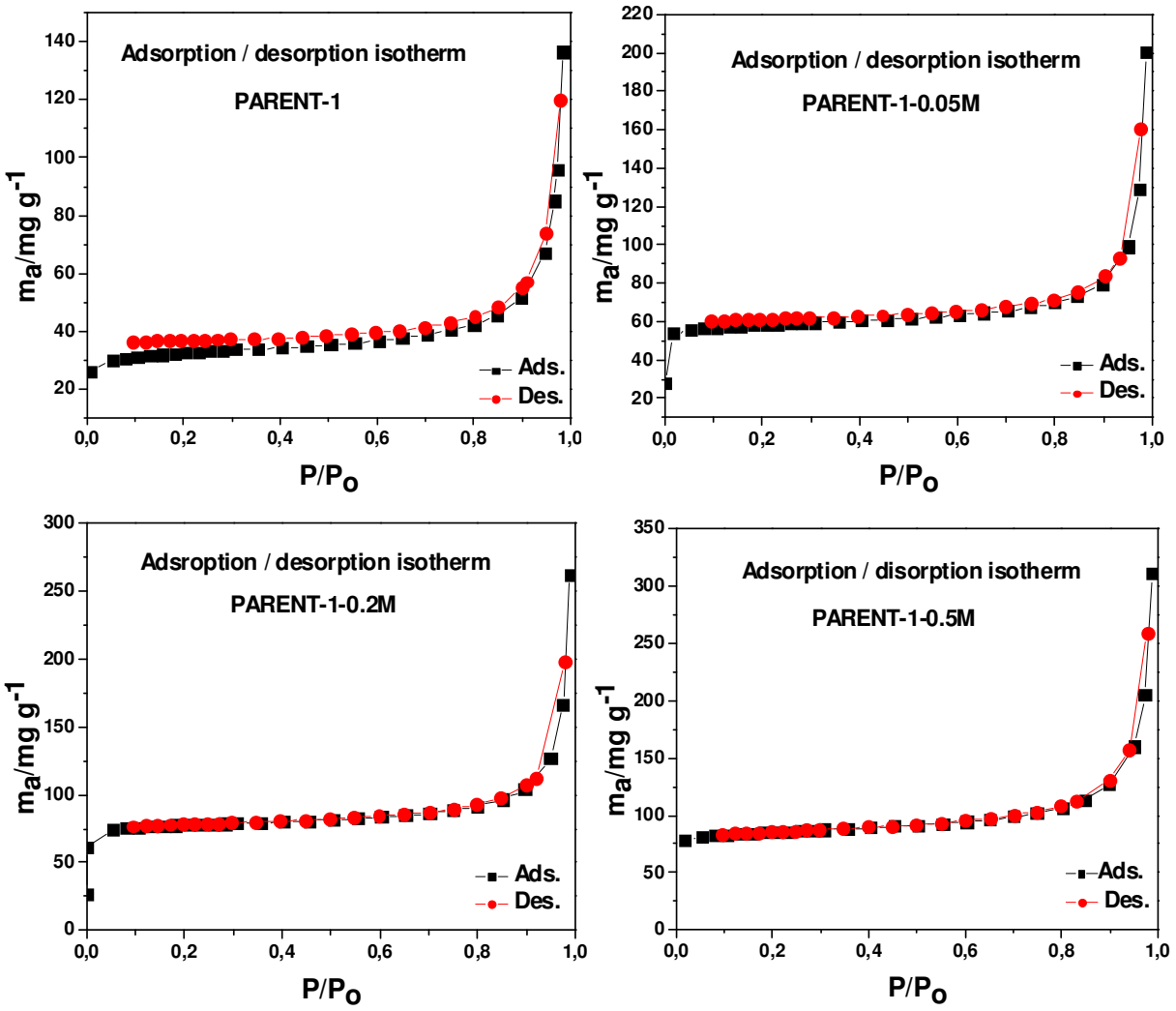

Figure 6.36 Nitrogen adsorption/desorption isotherms at 77 K for the PARENR-1 and NaOH treated ZSM-22 catalyst.

This means that the increase in surface area of ZSM-5 catalyst with alkali treatment can be ascribed to the formation of mesopores. However, in ZSM-22 catalyst, no mesopores were observed. The increase in surface area could be as a result of dissolving imperfect ZSM-22

crystals, or it could be due to removing of silicon from the framework without creating mesopores.

Figure 6.37 displays X-ray diffractograms of the PARENT-1 and NaOH treated sample. The crystallinity of the material is retained after the treatments.

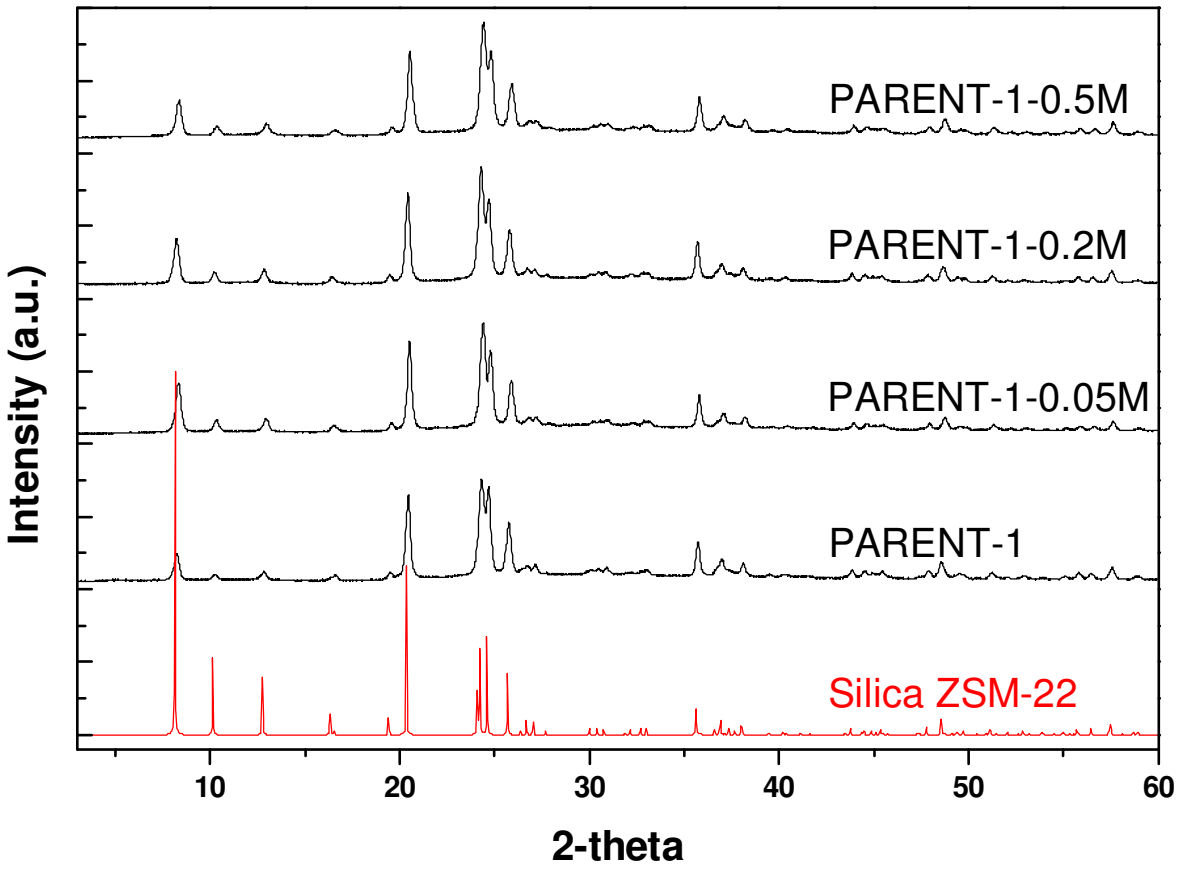

Figure 6.37 X-ray diffractograms of PARENT-1 and NaOH treated ZSM-22 catalyst.

Note the relative intensities of the peaks at about 23 and 24 °, the ratio between these peaks seemed to be sensitive to Si/Al ratios of ZSM-22 catalyst. (see Section 6.1.1 Figure 6.7 and Table 6.1). The ratio between these peaks decreased with increasing severity of the treatment, displayed in Table 6.10.

Table 6.10 Intensity rations between reflections at 2-theta = ~23 and ~24 ° (* = the ICP results are not the absolute Si/Al ratio but the can be used for comparing the relative Si/Al ratios of the catalysts (problem with our ICP standard)).

Catalyst	PARENT-1	PARENT-1-0.005M	PARENT-1-0.2M	PARENT-1-0.5M
Si/Al *	16.3	16.3	15.3	15.5
$I_{24^\circ}/ I_{23^\circ}$	0.92	0.75	0.73	0.73

Comparing this finding with the one presented in Section 6.1.1, it looks like alkali treatment is decreasing the Si/Al ratio, which is expected to happen as NaOH removes Si from the framework. However, ICP-AES analysis showed more or less similar Si/Al ratio before and after the treatment. These findings might happen if the Si atom leaves their framework positions but stay in the catalyst as an amorphous phase. If this is the case, XDR which is based on atoms in their framework position can show changes in the relative intensities of the 'sensitive peaks', while the Si/Al determined using ICP, which doesn't distinguish between framework and extra framework Si atoms, might not be affected. Based on the speculation stated above, amorphous phase retained in the channel could be the reason for the absence of visible mesopores in BET.

The effect of the treatment on the different sites of the catalysts was investigated using FTIR spectroscopy. Figure 6.38 displays the OH stretching regions of PARENT-1, PARENT-1-0.2, and PARENT-1-0.5 catalysts before the adsorption of CO.

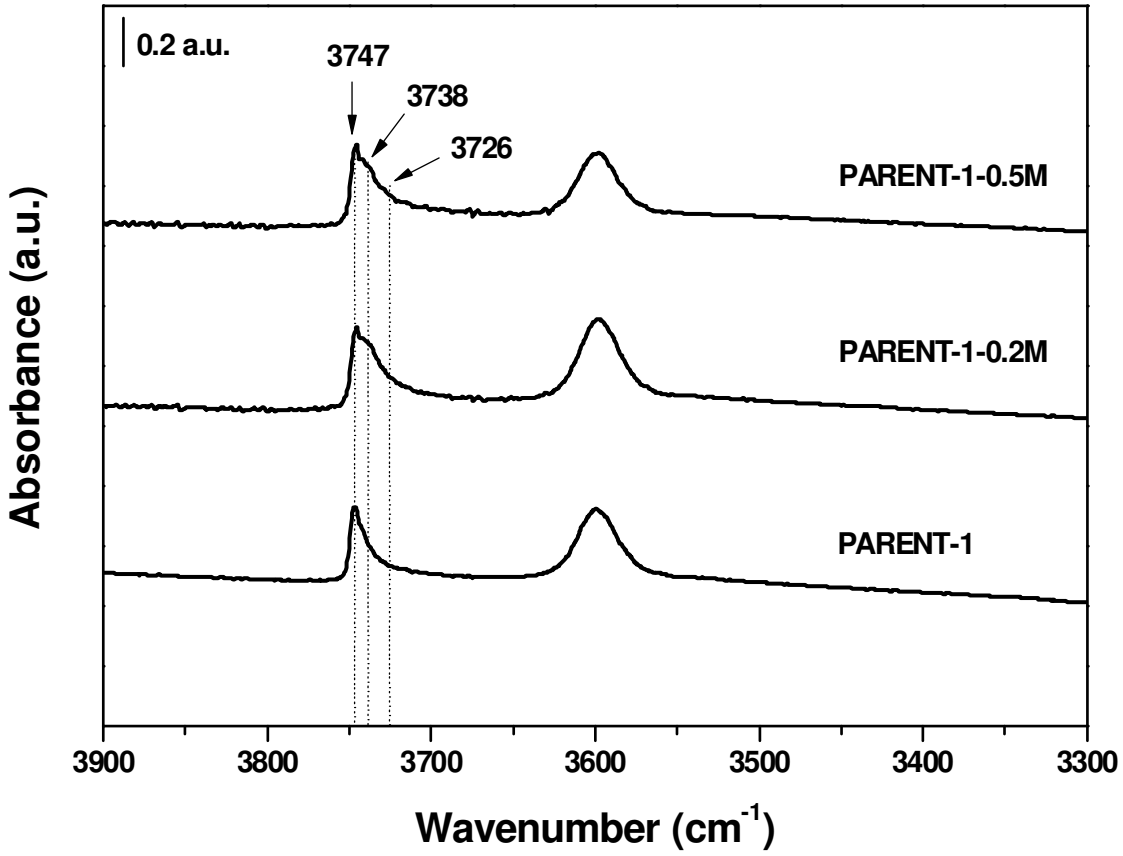

Figure 6.38 OH stratching region of PARENT-1, PARENT-1-0.2M and PARENT-1-0.5M catalysts.

Clearly, for all the catalysts two bands associated with OH stretching of silanols (~3747) and Brønested sites (~3604 cm^{-1}) were observed. There is no visible change in the Brønested bands, however, there is a clear change in silanol bands due to alkali treatment. A new band at ~3738 cm^{-1} is formed (or the intensity of the band at ~3738 cm^{-1} was increased) with alkali treatment of PARENT-1 catalyst. The observed band at ~3738 cm^{-1} is unclear, for alkali treated ZSM-5 catalysts this band is not reported [46, 69].

Figure 6.39 to Figure 6.41 displays the OH and CO stretching regions of the catalysts. The Brønested bands are consumed first with CO adsorption, however, the Brønested bands are not depleted completely even with substantial amounts of CO, the possible explanation for this observation is given in Section 6.1.6.

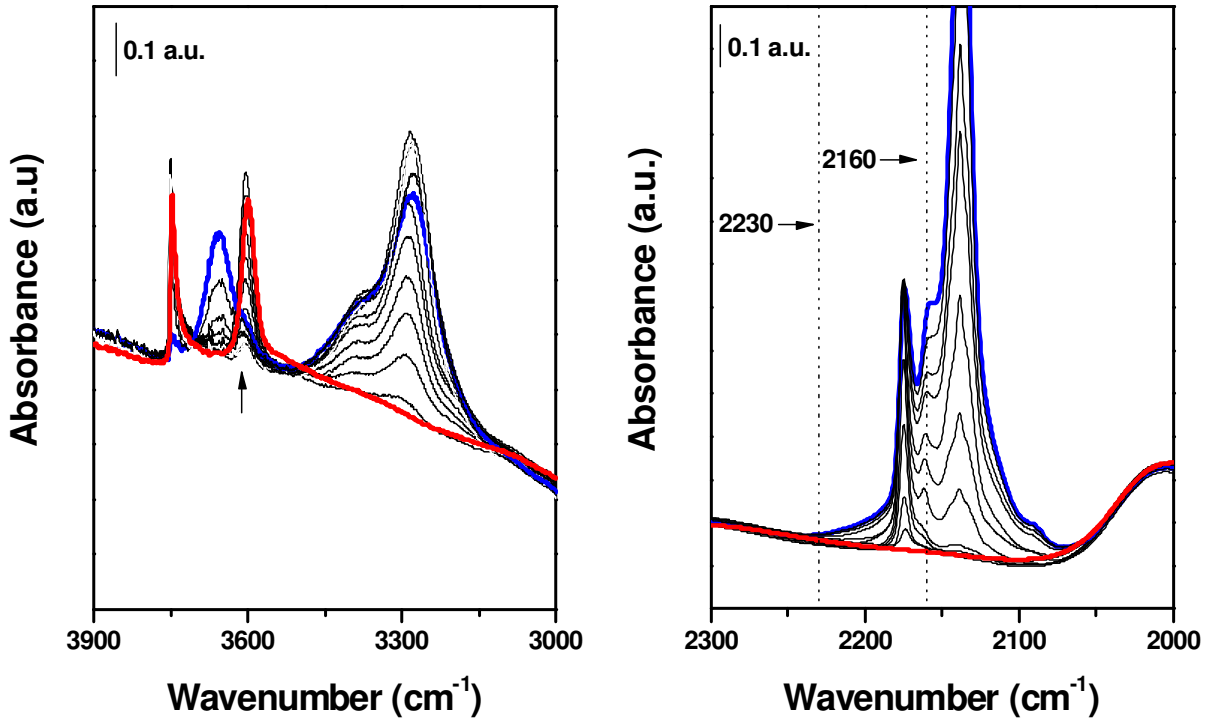

Figure 6.39 Adsorption of CO at 77K on PARENT-1 catalyst, IR spectra in the OH (left panel) and CO (right panel) stretching regions.

As can be seen from Figure 6.39 (left panel), the band associated to CO adsorption on silanols (max at ~2160 cm^{-1}) is more or less symmetrical at low CO coverage, and no band at 2230 cm^{-1} attributed to CO adsorption on extra framework Al (Lewis site) is observed. Clearly, the band at ~2160 cm^{-1} is no longer symmetrical after alkali treatment of the catalyst, even at lower CO coverage (Figure 6.40 and Figure 6.41). The same observation can be seen for alkali treated ZSM-5 catalyst [69].

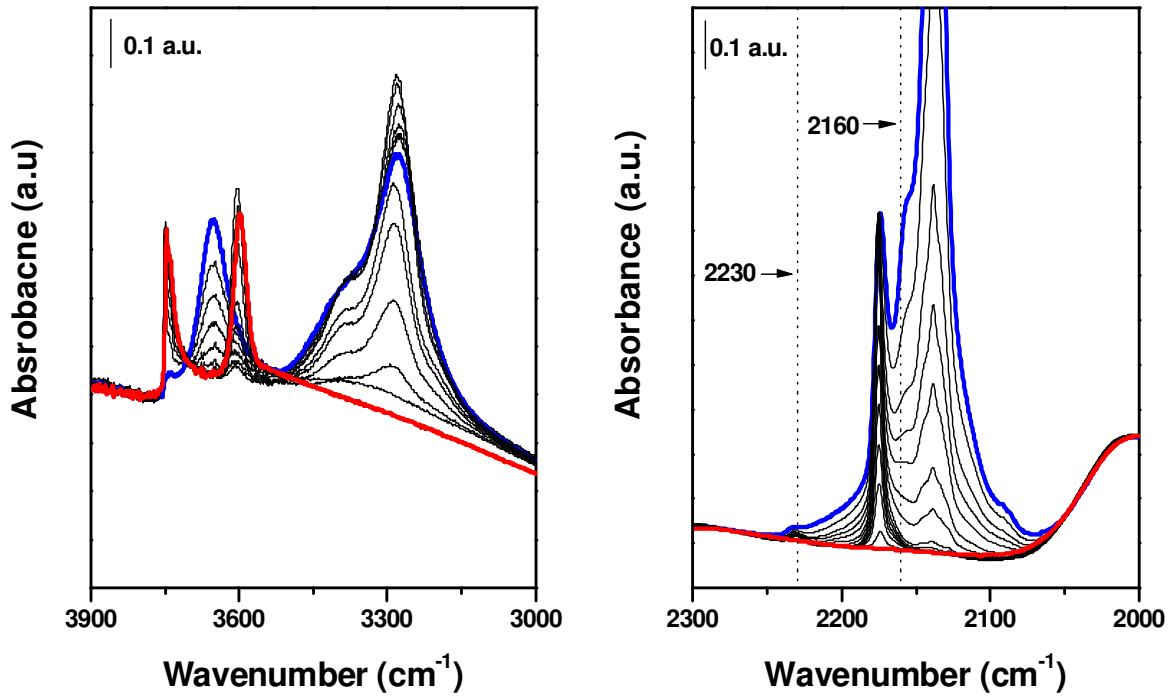

Figure 6.40 Adsorption of CO at 77K on PARENT-1-0.2M catalyst, IR spectra in the OH (left panel) and CO (right panel) stretching regions.

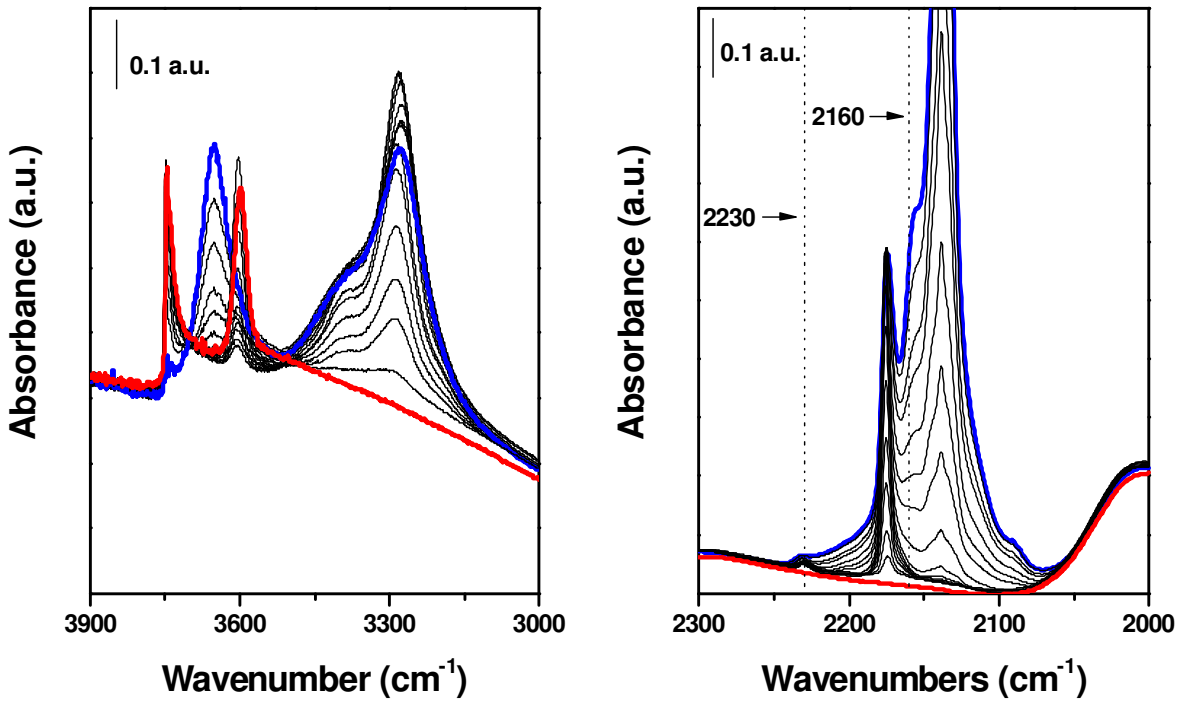

Figure 6.41 Adsorption of CO at 77K on PARENT-1-0.5M catalyst, IR spectra in the OH (left panel) and CO (right panel) stretching regions.

In addition to this, alkali treatment resulted in formation of extra framework Al, evidenced by the adsorption of CO on Lewis acid site at ~2230 cm^{-1}.From the IR observations, it is clear that the desilication is affecting the silanols, and Al leaves the framework.

Characterization PARENT-2 catalyst

The pH of the alkali solutions was measured during the treatment, and unlike PARENT-1 catalyst, in all of the treatments performed on PARENT-2 there was no change in the pH as a result of the treatment

Table 6.11 displays the treatment conditions used during desilication process and the resulting weight loss of PARENT-2 catalyst. The surface area of the catalyst was an affected by the treatment. Some of the treatment conditions are even tougher than the conditions used for PARENT-1 catalyst. However, PARENT-2 catalyst is found to be resistant to the treatment.

Table 6.11: Post synthesis treatment conditions, weight loss, and BET surface area of PARENT-2 and treated samples

Sample	Treated with	T °C	Time	Weight loss(%)	BET (m^2/g)
PARENT-2	-	-	-		205
PARENT-2-1	6 mmol/g NaOH/ g	75	30 min	8.2	210
PARENT-2-2*	6 mmol/g NaOH/ g (x4)	75	30 min	21.5	215
PARENT-2-3	6 mmol/g NaOH/ g	85	30 min	9.8	--
PARENT-2-4	6 mmol/g NaOH/ g	85	30 min	13.5	210
PARENT-2-5	6 mmol/g NaOH/ g	100	30 min	19.5	200
PARENT-2-6	15 mmol/g NaOH/ g	85	30 min	31.3	205
PARENT-2-7	6 mmol/g TMAOH/ g	75	30 min	4.9	--
PARENT-2-8	6 mmol/g NaOH/ g in 1 M NaCl	75	120 min	11.0	--

Figure 6.42 displays X-ray diffractograms of the PARENT-2 and NaOH treated sample. The crystallinity of the material is retained after the various treatments.

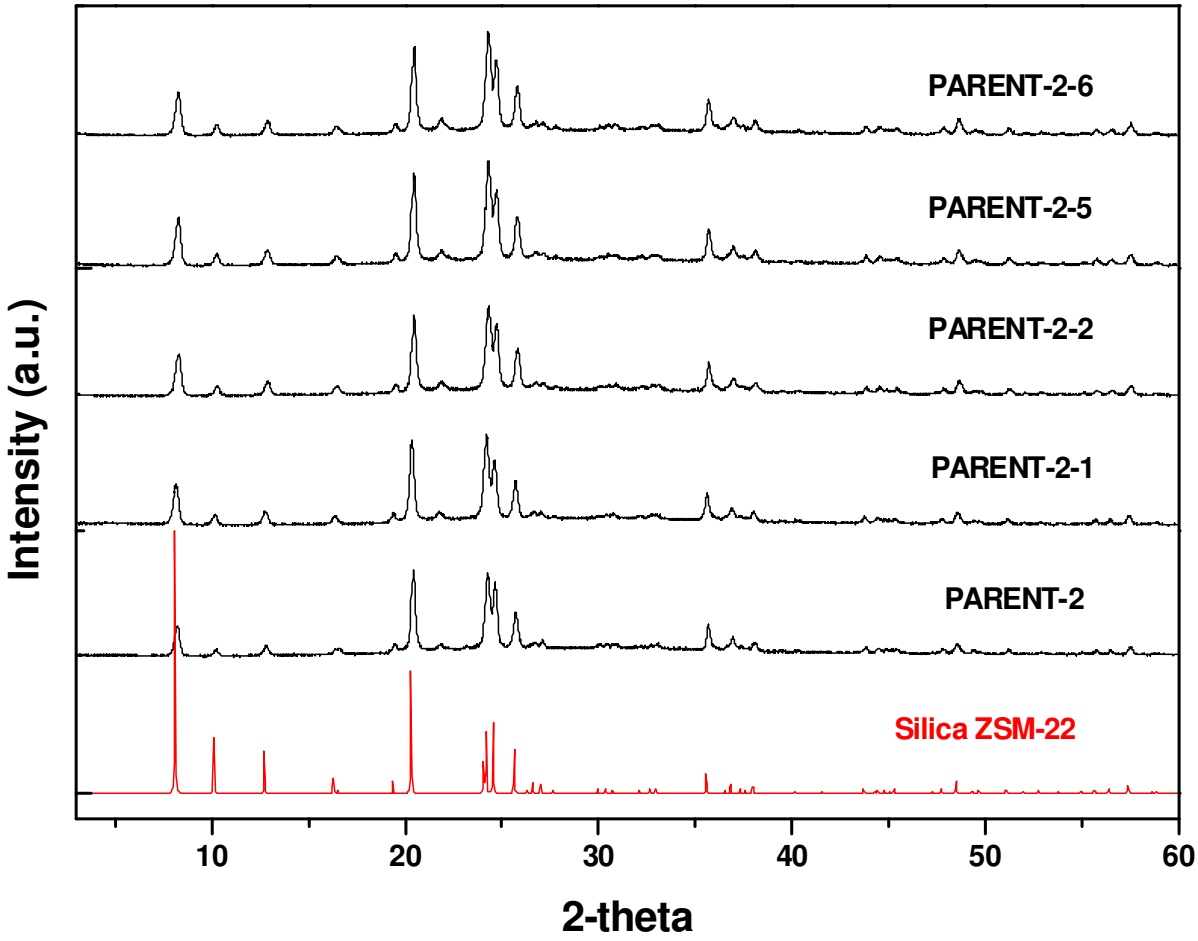

Figure 6.42 X-ray diffractograms of PARENT-2 catalyst treated alkali treated samples

6.5.2 Catalytic tests

Catalytic tests of PARENT-1

Figure 6.43 displays methanol conversion (%) as a function of time on stream (left panel) and total conversion capacity (right panel) of PARENT-1 and alkali treated samples. For all the samples the initial conversion was ~100%. The PARENT-1 catalyst showed rapid deactivation. The life time of the catalyst and their total methanol conversion capacities increased with increasing severity of the treatment. The conversion curve for the most severely treated samples was stable for several hours at high conversion of methanol. 0.05M, 0.2M, and 0.5M NaOH treatment of the PARENT-1 sample improved the total methanol conversion of the catalyst by a factor of 1.2, 2.2, and 2.8 respectively.

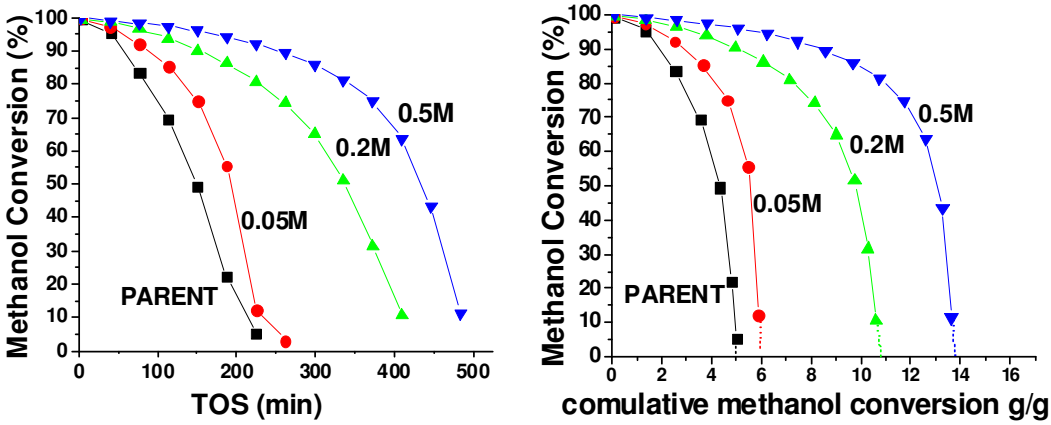

Figure 6.43 methanol conversion (%) as a function of time on stream (left panel) and cumulative amount of methanol that has been converted to hydrocarbons (right panel) over PARENT and NaOH treated ZSM-22 catalyst. Extrapolation to zero conversion (right panel) gives the total conversion capacity of the samples.

Figure 6.44 to Figure 6.47 displays the selectivity and yield plots of PARENT-1 and alkali treated catalyst at various treatment conditions. The trends in the selectivities are the same for all the samples. The selectivity for C_{6+} fraction increases with deactivation of the catalysts, which is faster for PARENT-1 catalyst than the others.

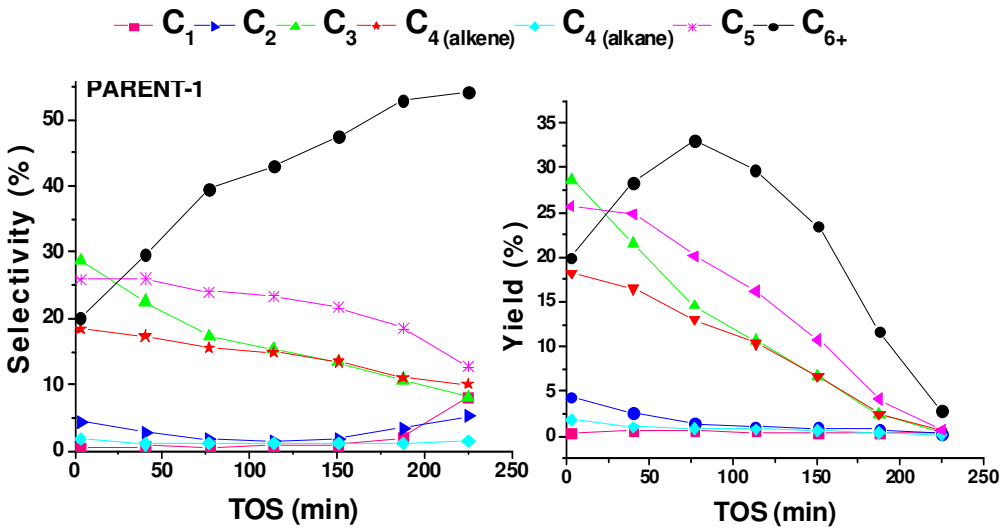

Figure 6.44 Product selectivity (left panel) and yield (right panel) at 400 °C, WHSV = 2.05 $gg^{-1}h^{-1}$ over PARENT-1 catalyst.

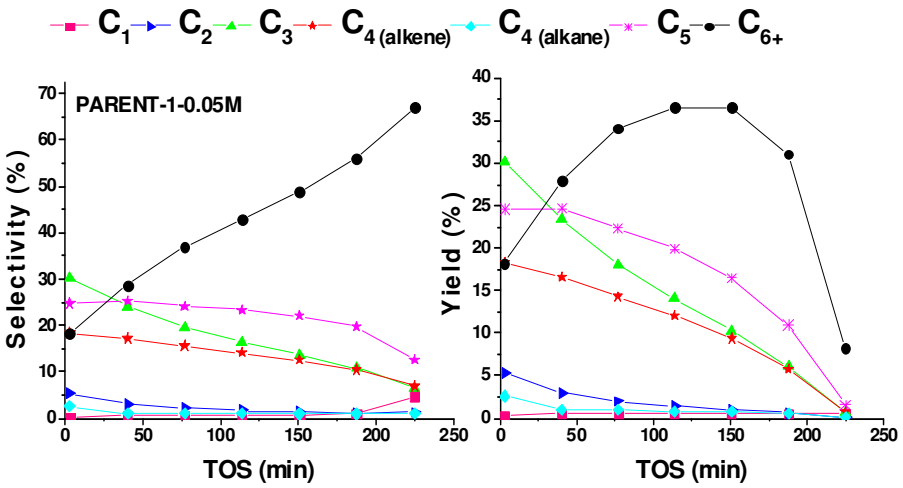

Figure 6.45 Product selectivity (left panel) and yield (right panel) at 400 °C, WHSV = 2.05 $gg^{-1}h^{-1}$ over PARENT-1-0.05M catalyst.

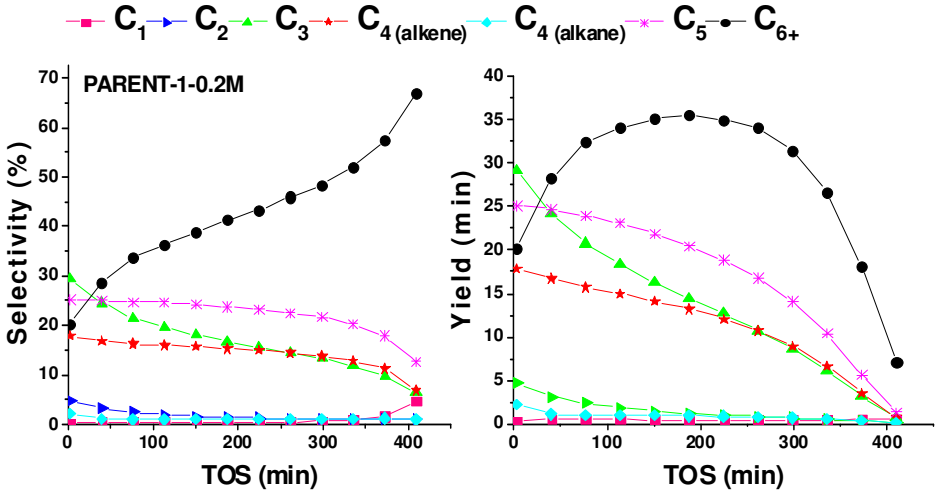

Figure 6.46 Product selectivity (left panel) and yield (right panel) at 400 °C, WHSV = 2.05 $gg^{-1}h^{-1}$ over PARENT-1-0.2M catalyst.

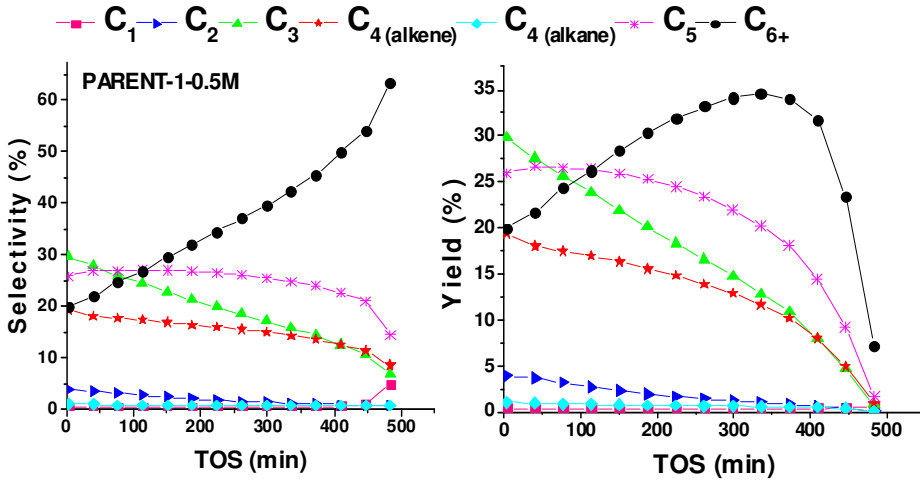

Figure 6.47 Product selectivity (left panel) and yield (right panel) at 400 °C, WHSV = 2.05 $gg^{-1}h^{-1}$ over PARENT-1-0.5M catalyst.

Catalytic tests of PARENT-2

Figure 6.48 displays methanol conversion capacity as a function of time on stream for PARENT-2 and alkali treated samples. Clearly, tough treatments have decrease the life time of the catalyst. The catalyst deactivated faster when treated at 100 °C (PARENT-2-5) and at high concentration of NaOH (15milmol/g catalyst, PARENT-2-6). The other treatments slightly improved the activity of the catalyst. However, comparing to PARENT-1 catalyst, the improvement in catalytic activity of PAREN-2 catalyst is much lower. This is in agreement with the stability of the catalyst during the alkali treatment.

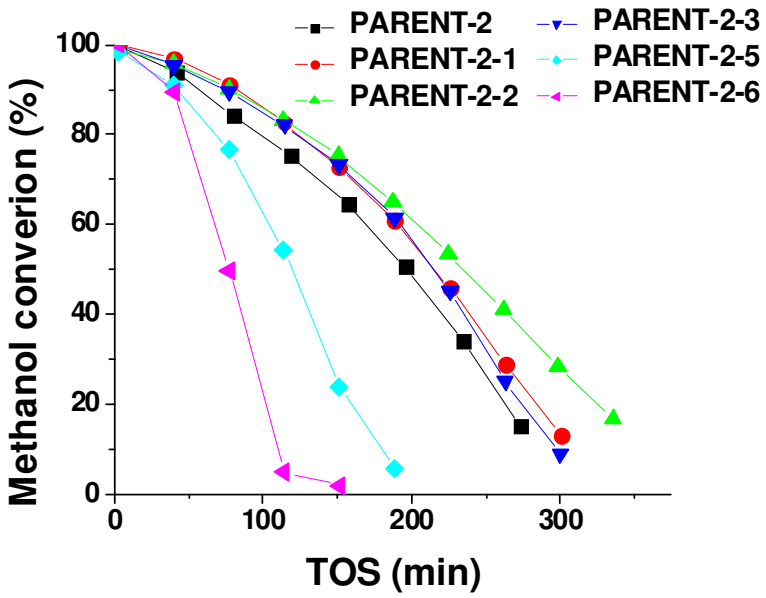

Figure 6.48 methanol conversion as a function of time on stream for PARENT-2 catalyst before and after the various alkali treatments.

Figure 6.49 displays the product selectivity of PARENT-2 catalyst before and after the various alkali treatments. The initial selectivities over the fresh catalyst for some of the plots is missing, due to problems with injection system of the online GC instrument. The trend in the selectivities are similar.

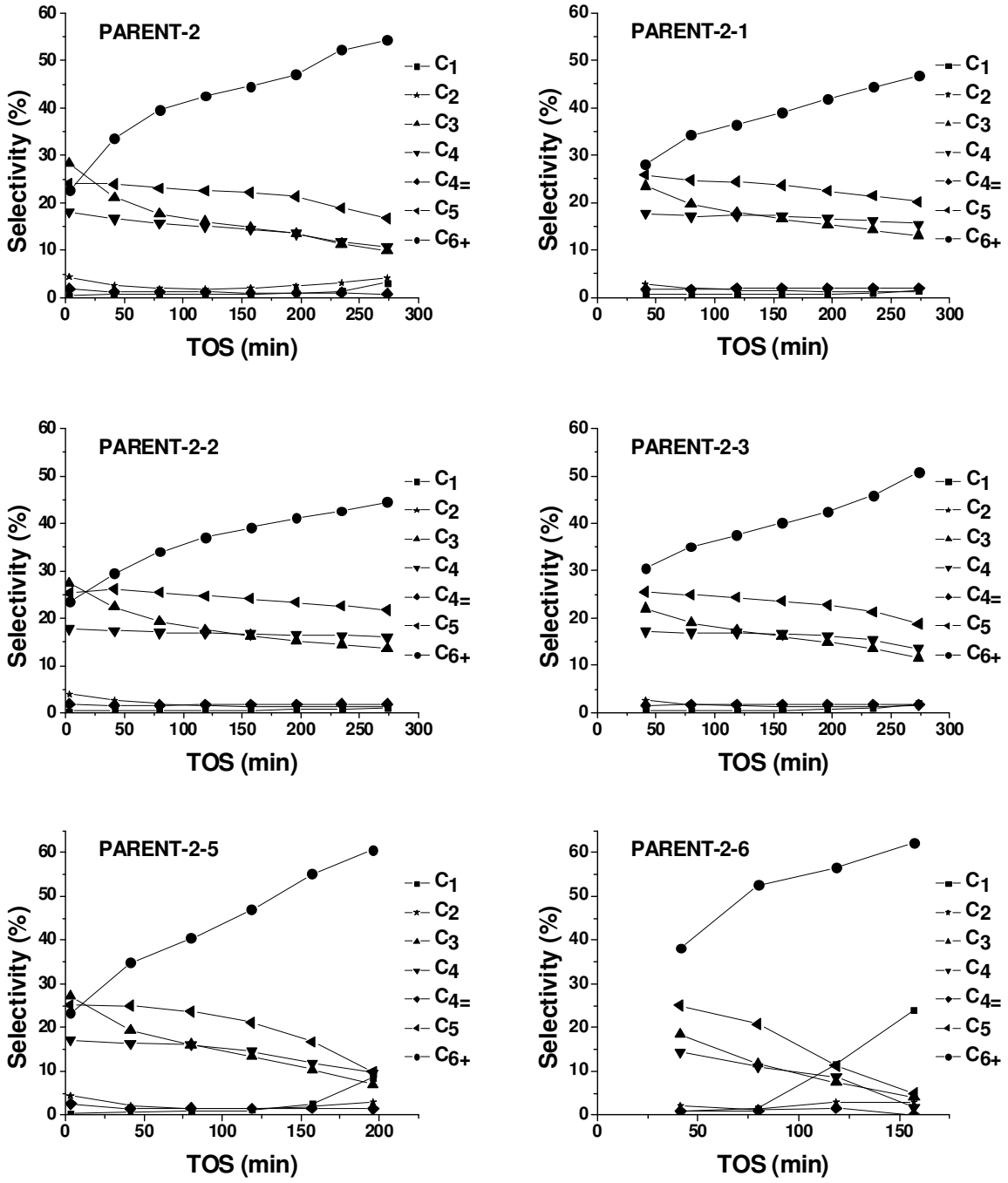

Figure 6.50 Product selectivities as a function of time on stream for PARENT-2 catalyst before and after alkali treated samples.

6.6 Isotopic labeling

The isotopic composition of the alkene effluent and the retained organics during the MTH reaction over ZSM-22 catalyst was investigated by $^{12}C/^{13}C$ methanol switch experiments as described in Section 5.4. Figure 6.51 shows the total ^{13}C content (%) in effluents and the retained hydrocarbons after 5 minutes of ^{12}C methanol reaction (left panel) and after 18 minutes of ^{12}C methanol reaction (right panel) followed by a switch to ^{13}C methanol and further reaction for 0.5, 1 and 2 min at 400 °C over ZSM-22(207) catalyst, WHSV = 2,05 h^{-1}. In both 5 and 18 minutes on stream the catalyst shows full methanol conversion.

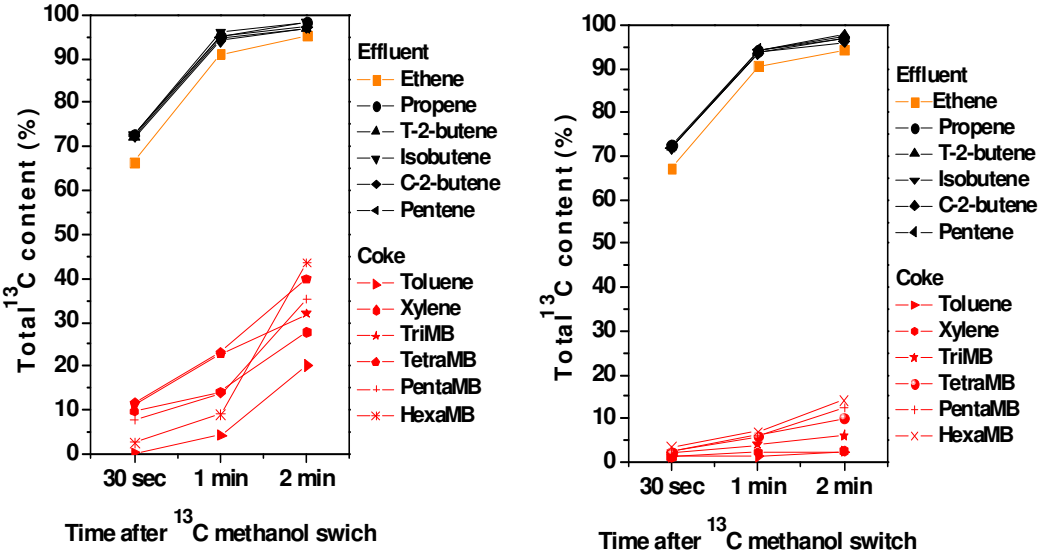

Figure 6.51 Total ^{13}C content (%) in the effluent and the retained hydrocarbons after 5 minutes ^{12}C methanol reaction followed by a switch to ^{13}C methanol and further reaction for different times at 400 °C over ZSM-22 catalyst. (the catalyst obtained after 5 minutes ^{12}C methanol reaction followed by a switch to ^{13}C methanol was kept 1 month after it is coked prior to the dissolution experiment)

The total ^{13}C content in ethene is slightly lower than the other alkenes (C_3-C_5), indicating that the rate of ^{13}C incorporation in ethene is slightly slower. The total ^{13}C contents in all the other alkenes are quite similar. Slower ^{13}C incorporation in ethene has been reported previously for MTH reaction over H-ZSM-5 catalyst [35, 38]. This observation could be ascribed to its rate of methylaion . Svelle et al. studied lower methylation rate of ethene Methylation of ^{12}C-ethene, ^{12}C-propene and ^{12}C-butene with ^{13}C-methanol showed that for all olefins studied the methylation rate is first order in the olefin and zero order in methanol, and the methylation rate increases in the order ethene, propene, butene,

The rate of incorporation of ^{13}C in the retained materials, which are believed to be reaction centers in hydrocarbon pool reaction mechanism, is significantly slower in comparison to the rate of incorporation into the gas phase alkenes. As can be seen in Figure 6.51(left panel), rate of incorporation of ^{13}C in the retained materials after 5 minutes on stream is relatively faster than the ^{13}C incorporation after 18 minutes on stream (right panel). For a SAPO-34 catalyst, $^{12}C/^{13}C$ switching experiments performed after 3, 25 and 80 minutes on stream has shown that the rate of incorporation of ^{13}C in the retained hydrocarbons is faster when switching after 3 minutes ^{12}C methanol reaction than when switching after 25 and 80 minutes ^{12}C methanol reaction [81]. Part of the catalyst crystals was assumed to be deactivated to rationalize this observation. This means that the retained hydrocarbons in the deactivated crystals will not be accessed by the incoming ^{13}C methanol, which will result in less ^{13}C content in the retained hydrocarbons. For ZSM-22 catalyst the slower incorporation of ^{13}C when switching after 18 minutes than when switching after 5 minutes could be explained as that of SAPO-34. The ZSM-22 crystals are needle shaped, and retained hydrocarbons can block part of the channel form the incoming ^{13}C. Hydrocarbons trapped in the blocked channels will not undergo reactions involving ^{13}C incorporation, and as the retained hydrocarbons and blocked channels increase with time on stream, switching after 18 minutes will give rise to less ^{13}C than switching after 5 min. The ^{13}C content in the retained hydrocarbons after 5 minutes is significantly less than the ^{13}C content in the effluent, this could mean that already after 5 minutes most of the retained hydrocarbons are mainly coke and they do not participate in alkene formation. This in turn could mean that already after 5 minutes only part of the crystals are involved in hydrocarbon pool reactions.

Figure 6.52 displays the total ^{13}C content in the retained hydrocarbons after different times of ^{13}C methanol reaction. When switching after 5 minutes ^{12}C methanol reaction, the rate of incorporation of ^{13}C in the retained hydrocarbons increases with increasing the number of methyl group on the aromatic ring of the methylbenzenes up to tetramethyl benzene. The ^{13}C content in pentaMB and hexaMB was ~7 and ~2% respectively after 0.5 min ^{13}C methanol reaction, and with increasing the ^{13}C methanol reaction the total ^{13}C of pentaMB and hexaMB increased much faster in comparison with the other methylbenzenes. This rapid increase in unusual and it could be due to keeping of the coked catalyst for 1 month prior to the dissolution experiment.

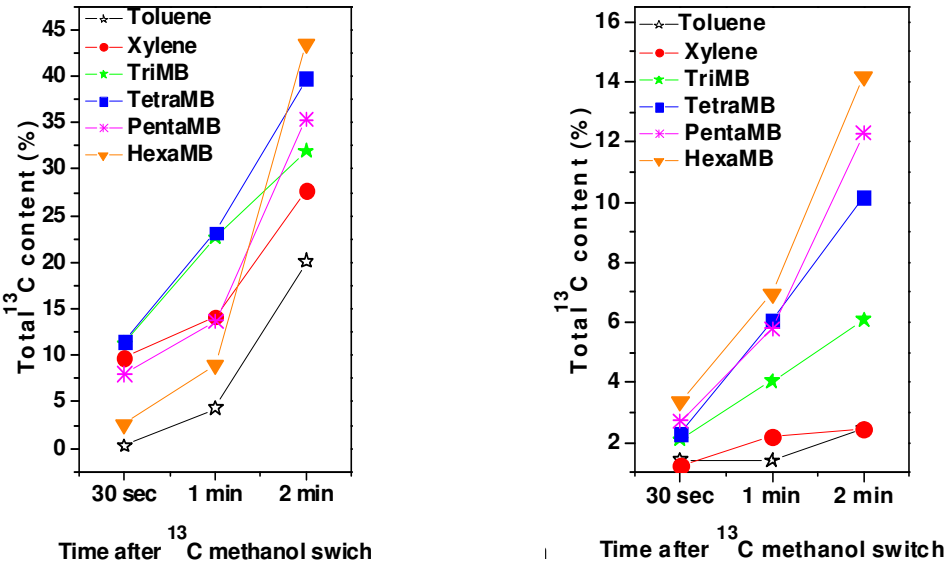

Figure 6.52 Total ^{13}C content after 5 min ^{12}C methanol reaction (left panel) and after 18 min ^{12}C methanol reaction (right panel) followed by a switch to ^{13}C methanol and further reaction for 0.5, 1 and 2 min at 400 °C over ZSM-22 catalyst.

When switching after 18 minutes ^{12}C reaction, the rate of incorporation of ^{13}C in the retained hydrocarbons increased with increasing the number of methyl group on the aromatic ring. At all analysis times (0.5, 1 and 2 min), toluene and haxaMB had the lowest and the highest ^{13}C contents respectively. This indicates that hexaMB is the most active species among the methylbenzenes. This in turn could mean that the hydrocarbon pool reaction mechanism in ZSM-22 catalyst proceeds via higher methylbenzenes as in SAPO-34 [81] and zeolite beta [82] catalysts.

In comparison to other known zeolites [35, 38, 81, 82], ZSM-22 shows very low ^{13}C incorporation in the retained hydrocarbons. Clearly, after few minutes on stream the retained hydrocarbons are inactive coke. This means that in addition to the hydrocarbon pool mechanism which is responsible for the initial alkene formation, the olefin methylation-cracking reaction mechanism (see Section 2.1.2) in occurring. The olefin methylation-cracking reaction mechanism is thus, the main reaction mechanism and responsible for the net methanol conversion.

Figure 6.53 displays the distribution of ^{13}C in the effluent compounds after 5 minutes ^{12}C methanol reaction followed by a switch to ^{13}C methanol and further reaction for 0.5, 1 and 2 minutes.

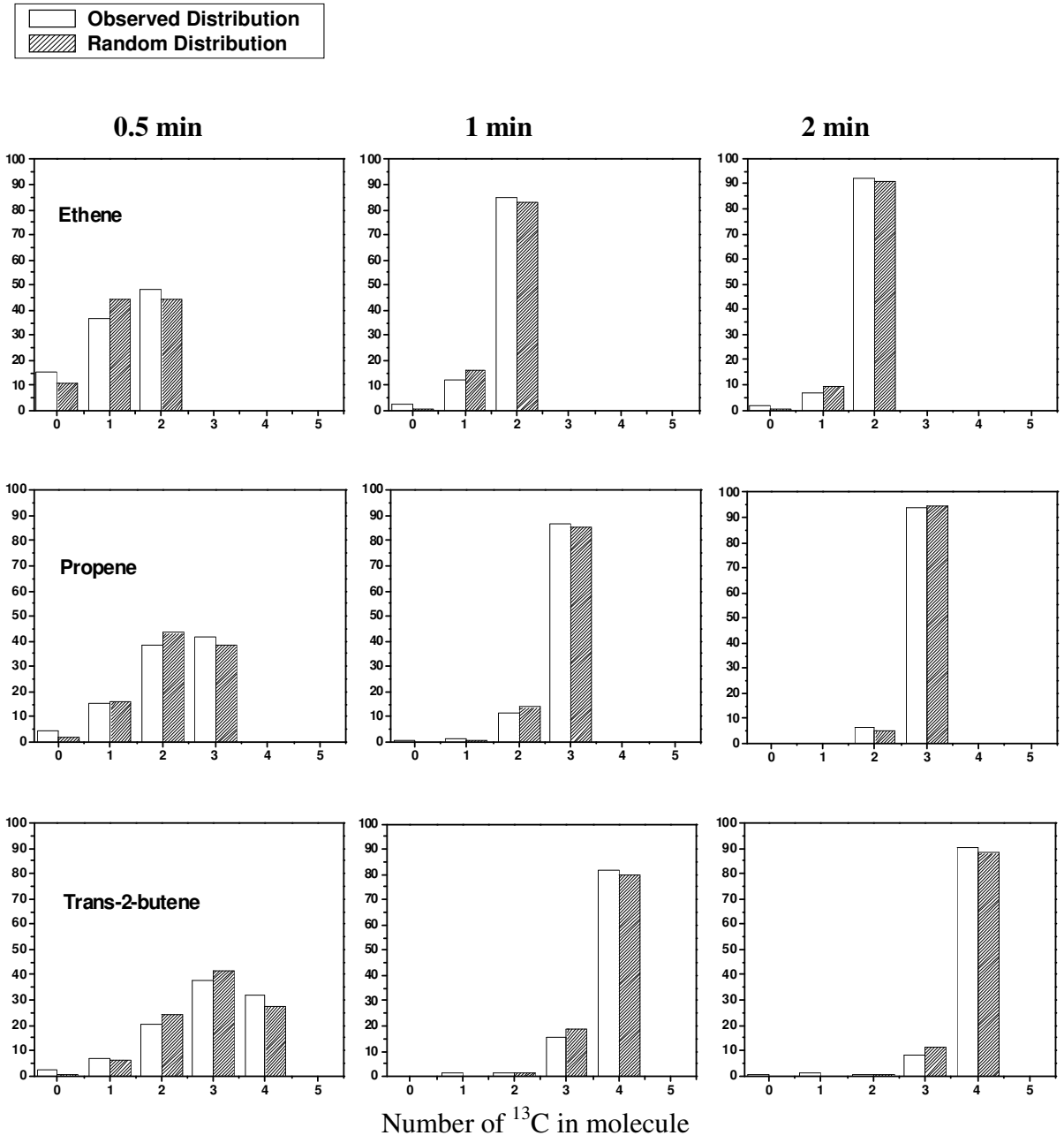

Figure 6.53 distribution of ^{13}C in the effluent compounds after 5 minutes ^{12}C methanol reaction followed by a switch to ^{13}C methanol over ZSM-22(207) catalyst

The observed distribution (white bar) resembles the random distribution (gray bar). After 2 minutes of ^{13}C reaction, most of the carbons in the molecules are labeled.

Figure 6.53 continued

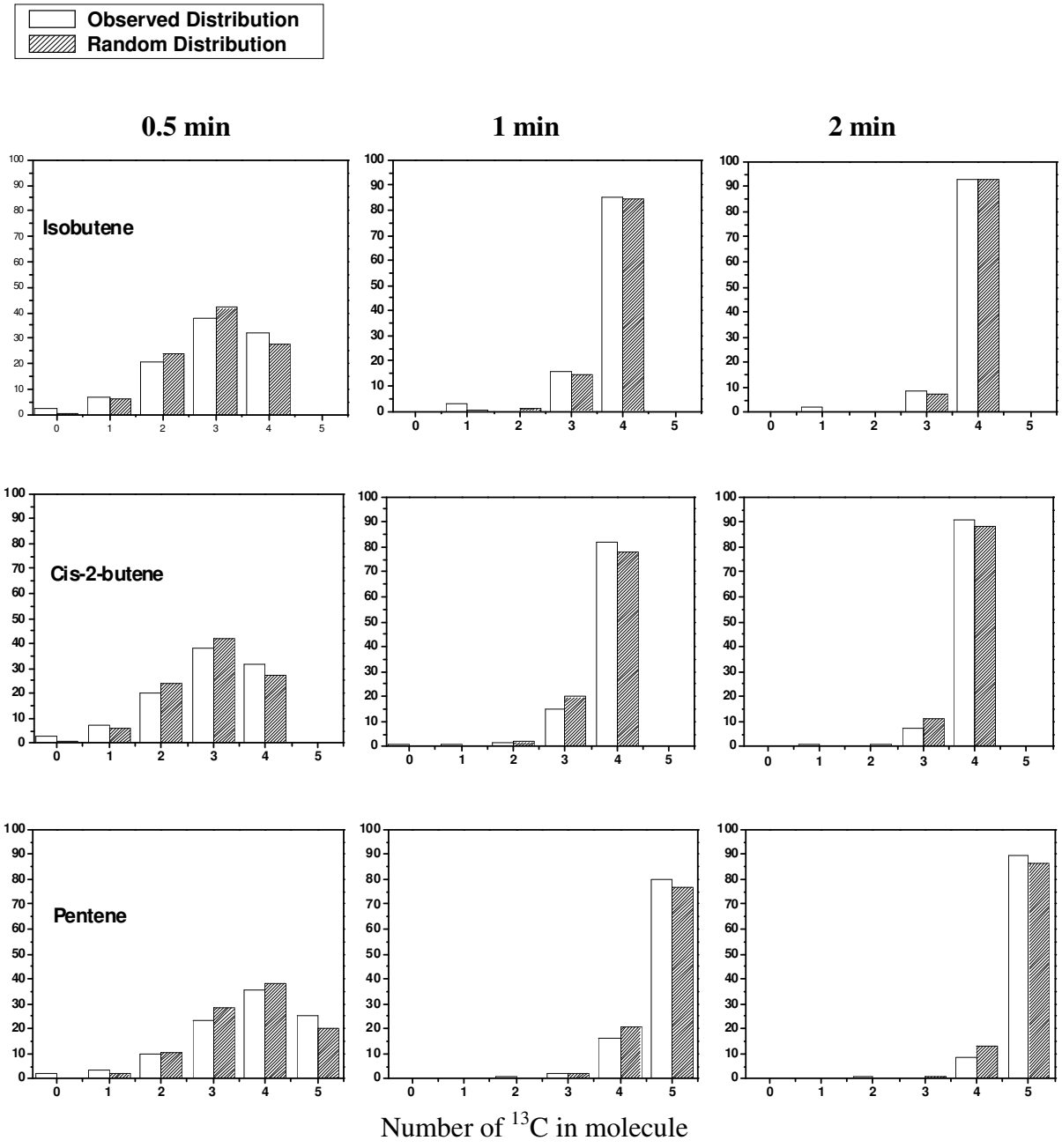

Figure 6.53 distribution of ^{13}C in the effluent compounds after 5 minutes ^{12}C methanol reaction followed by a switch to ^{13}C methanol over ZSM-22(207) catalyst.

Figure 6.54 displays the distribution of ^{13}C in the effluent compounds after 18 minutes ^{12}C methanol reaction followed by a switch to ^{13}C methanol and further reaction for 0.5, 1 and 2 minutes.

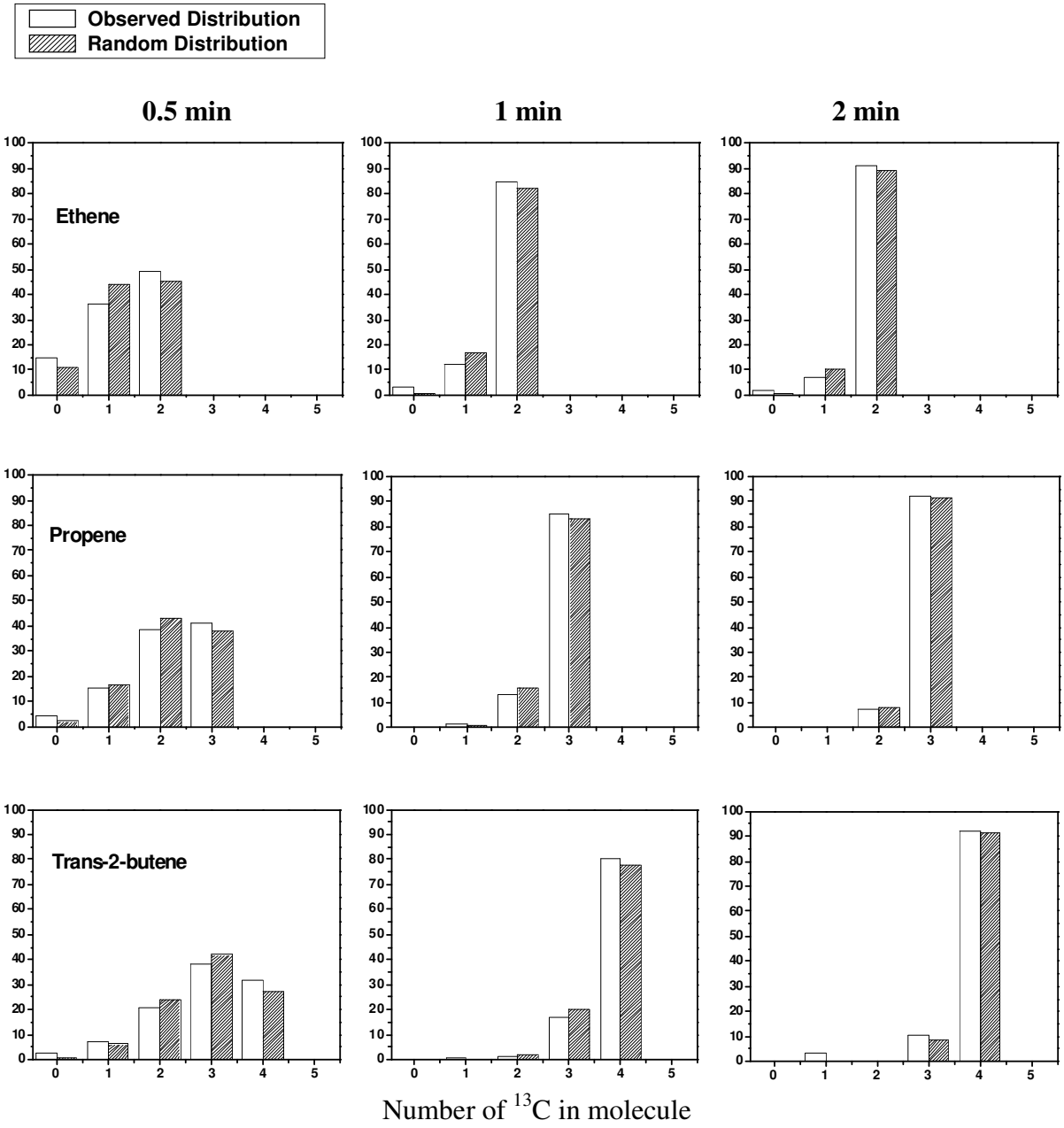

Figure 6.54: distribution of ^{13}C in the effluent compounds after 18 minutes ^{12}C methanol reaction for followed by a switch to ^{13}C methanol over ZSM-22(207) catalyst.

The observed distribution (white bar) resembles the random distribution (gray bar).). After 2 minutes of ^{13}C reaction, most of the carbons in the molecules are labeled.

Figure 6.54 continued

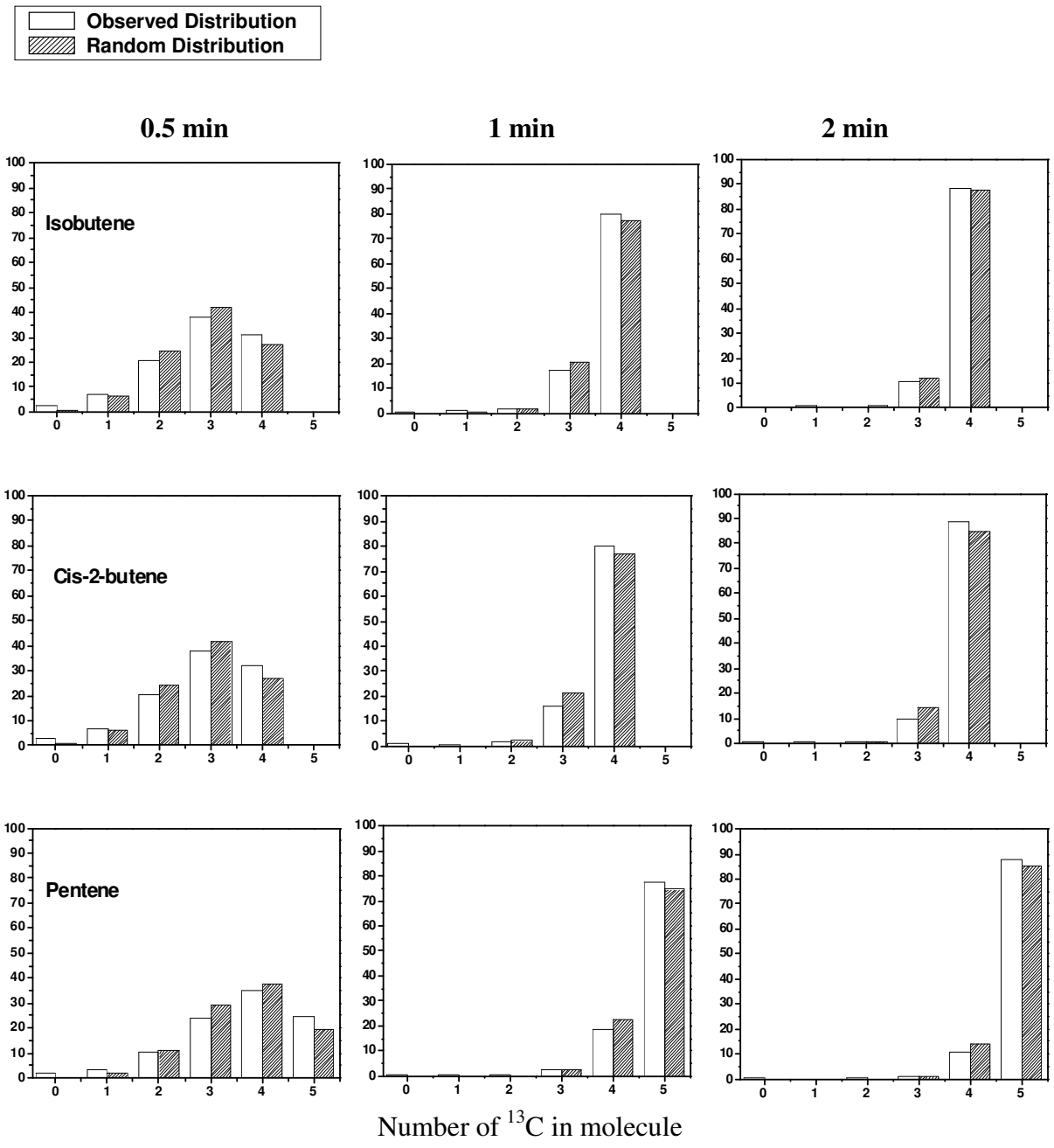

Figure 6.54 distribution of ^{13}C in the effluent compounds after 5 minutes ^{12}C methanol reaction followed by a switch to ^{13}C methanol over ZSM-22(207) catalyst.

Figure 6.55 displays the distribution of ^{13}C in the retained hydrocarbons after 5 minutes ^{12}C methanol reaction followed by a switch to ^{13}C methanol and further reaction for 0.5, 1 and 2 minutes.

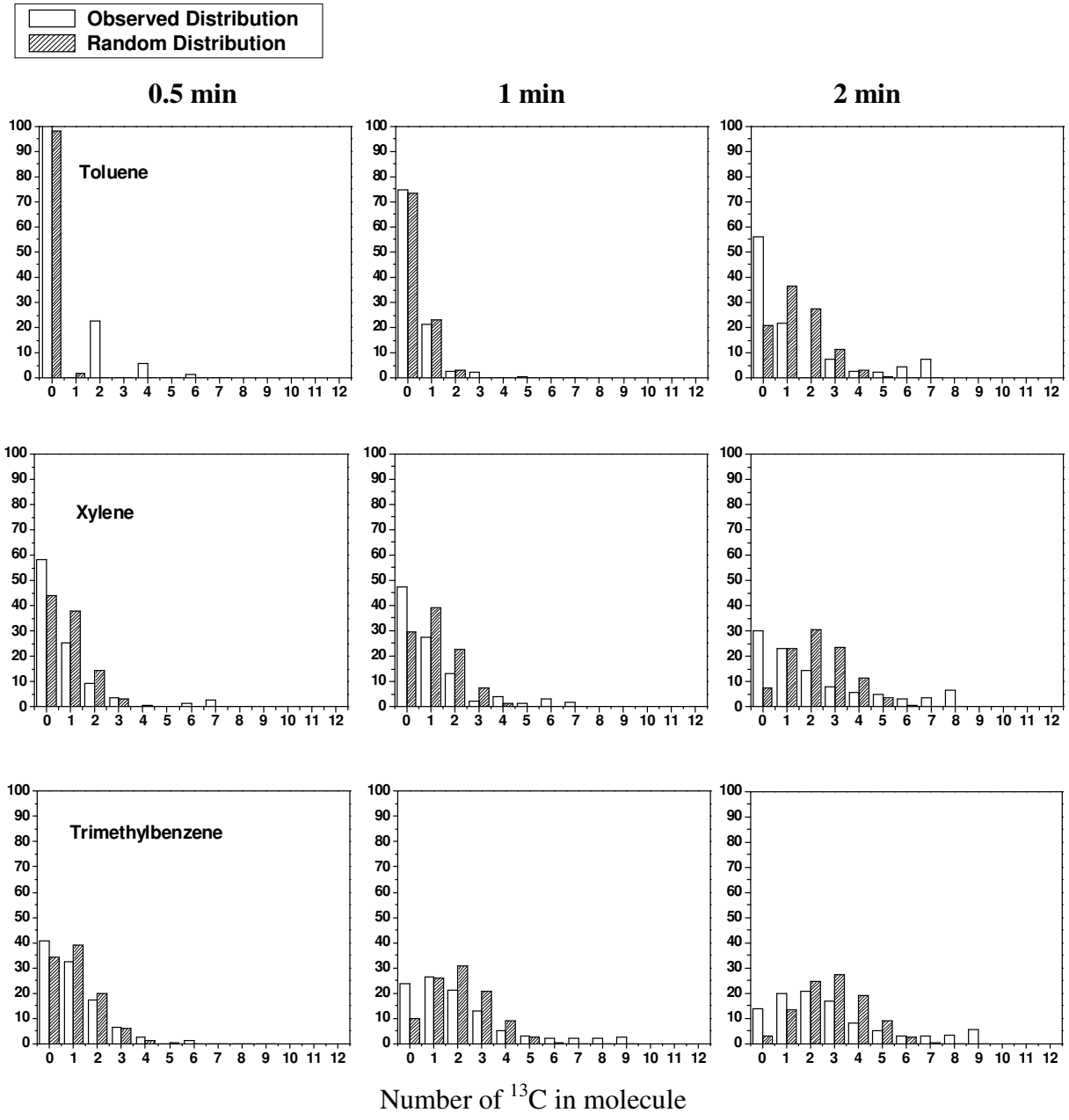

Figure 6.55: distribution of ^{13}C in the retained hydrocarbons after 5 min ^{12}C methanol reaction for followed by a switch to ^{13}C methanol over ZSM-22(207) catalyst.

The distribution not random, especially after 2 minutes of ^{13}C methanol reaction. With increasing ^{13}C methanol reaction, the number of molecules containing more than one ^{13}C carbons in a molecule increases.

Figure 6.55 continued

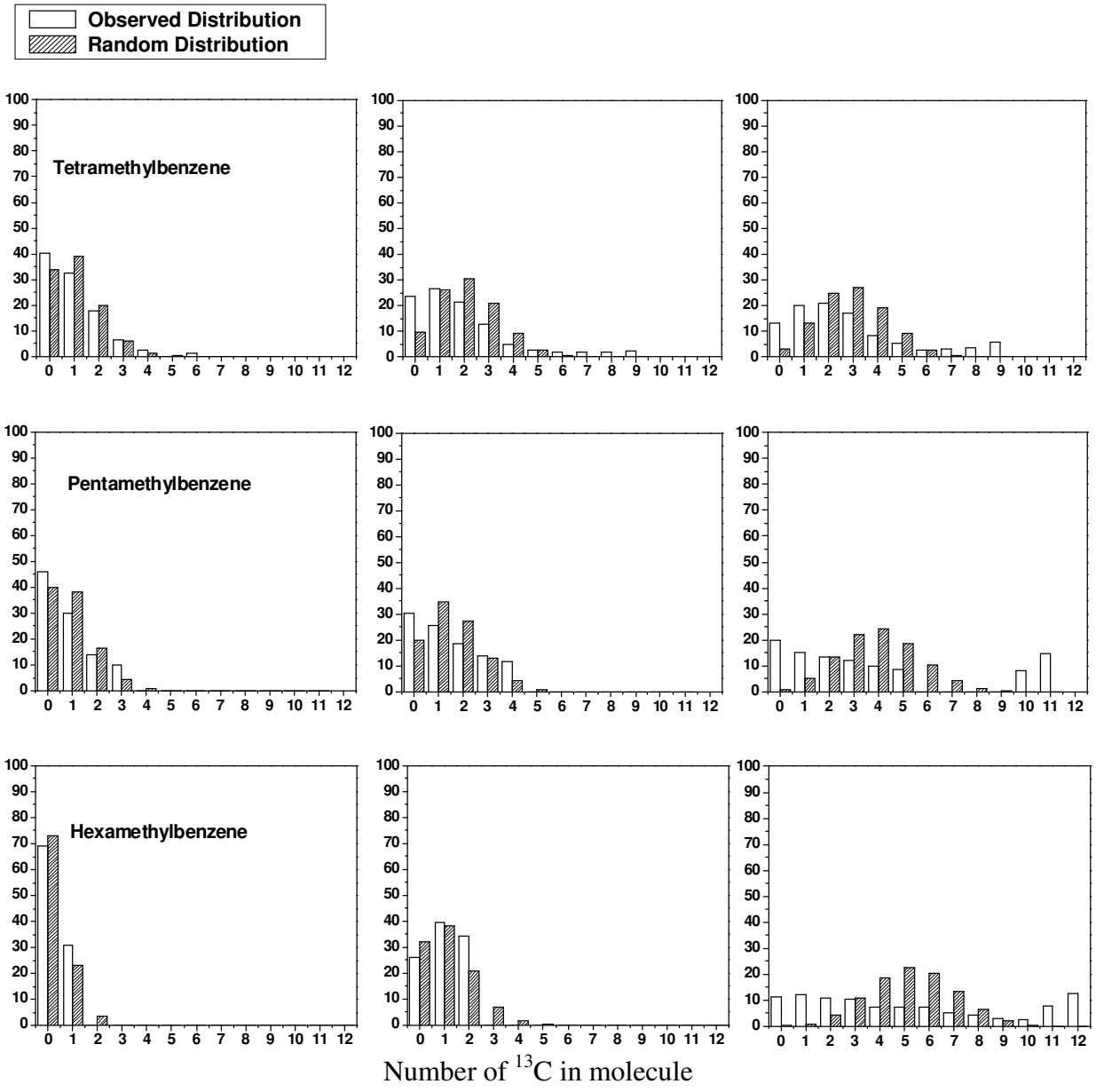

Figure 6.55 distribution of ^{13}C in the retained hydrocarbons after 5 minutes ^{12}C methanol reaction followed by a switch to ^{13}C methanol over ZSM-22(207) catalyst.

Figure 6.56 displays the distribution of ^{13}C in the retained hydrocarbons after 18 minutes ^{12}C methanol reaction followed by a switch to ^{13}C methanol and further reaction for 0.5, 1 and 2 minutes.

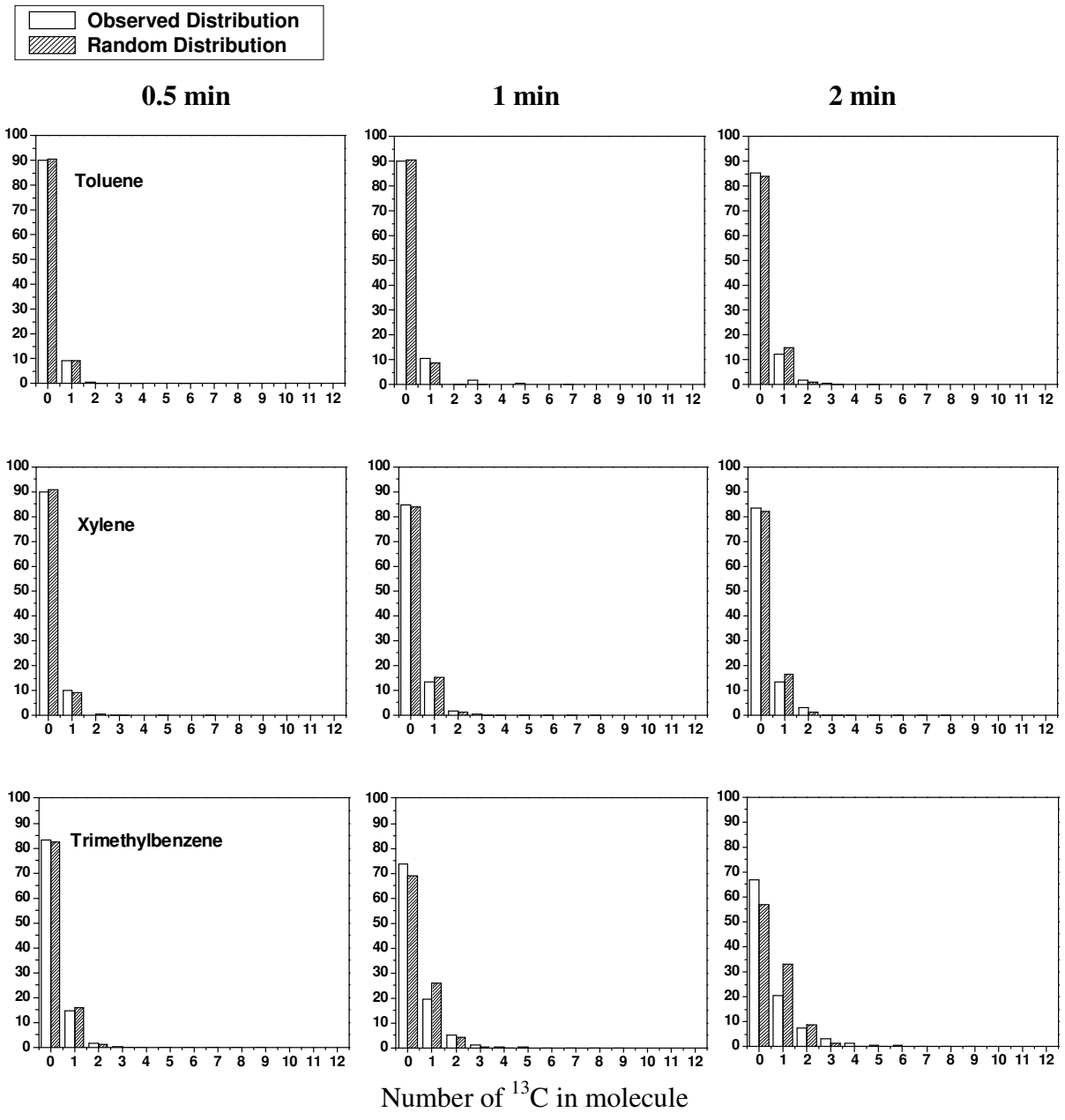

Figure 6.56: distribution of ^{13}C in the retained hydrocarbons after 18 minutes ^{12}C methanol reaction for followed by switch to ^{13}C methanol over ZSM-22(207) catalyst.

Even after 2 minutes of ^{13}C reaction, most of the carbons in the molecules are unlabeled.

Figure 6.56 continued

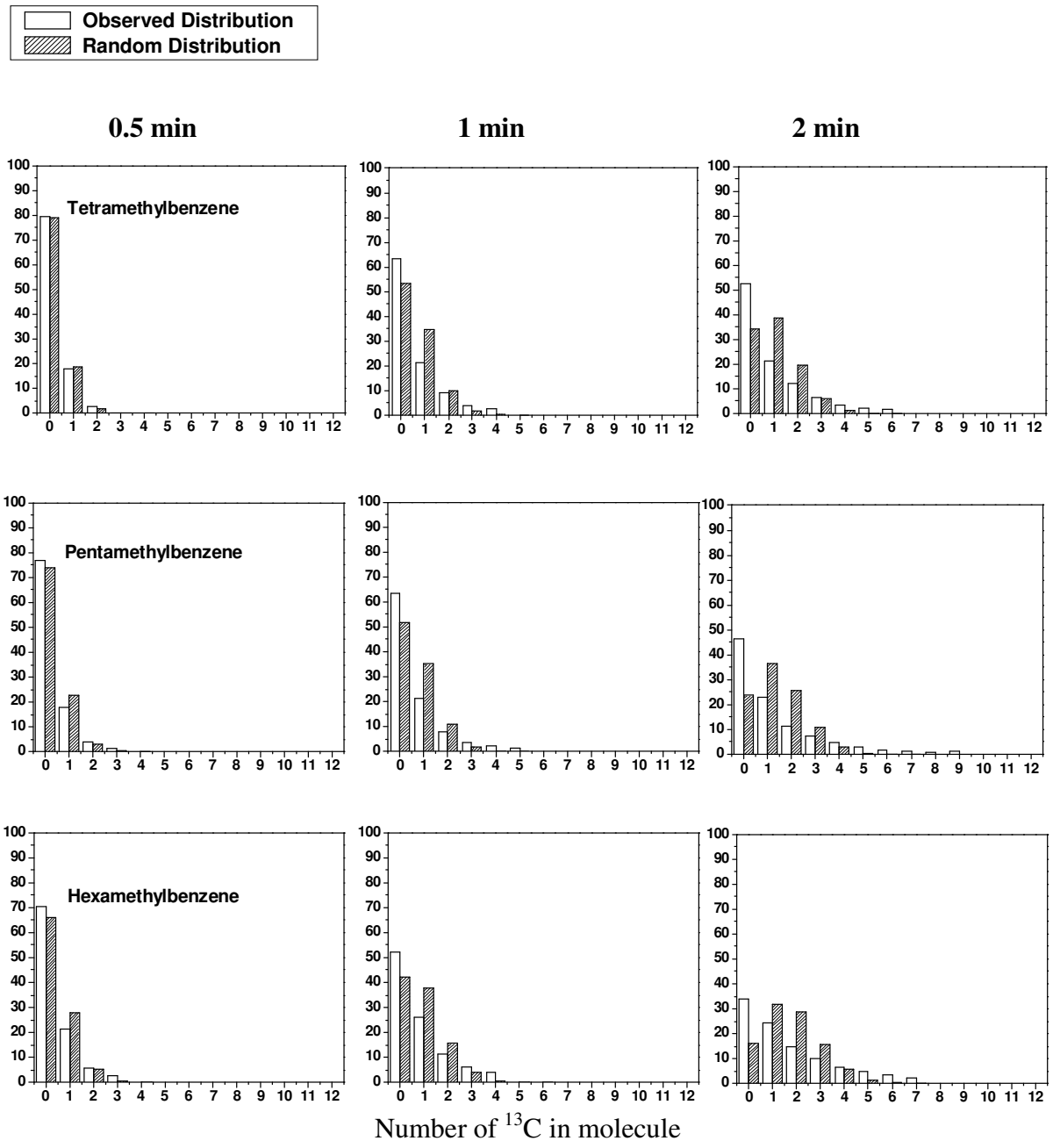

Figure 6.56 distribution of ^{13}C in the retained hydrocarbons after 18 minutes ^{12}C methanol reaction followed by a switch to ^{13}C methanol over ZSM-22(207) catalyst.

6.7 Conclusions and further work

Conclusions

ZSM-22 catalysts can be synthesized in wider conditions. Depending on the organic template used, homogenization of the gel may be required during crystallization. The Si/Al ratio can be controlled.

Unlike the previous reports [39-41], ZSM-22 is an active catalyst for the MTH reaction. Low feed rates and temperature in the range 400-500 °C are required for appreciable conversion. The product spectrum of the ZSM-22 catalyzed MTH reaction is intermediate those found in MTO (SAPO-34 based) and MTG (ZSM-5 based). At 400 °C the catalyst showed high selectivity for C_{5+} fraction which could be used for the production of environmentally friendly low-aromatic gasoline. Aromatic reactions centers required for initial alkene formation were found to reside inside the narrow channels of ZSM-22. However, after few minutes on stream, the ^{13}C incorporation to the aromatic reaction centers was very low, this observation suggests that the alkene methylation-cracking mechanism is main reaction mechanism of the MTH reaction over ZSM-22 catalyst. Post synthesis treatment (desilication) has improved the catalytic activity of one batch of the catalyst, suggesting that the activity of the material can be improved.

Further work

It could be interesting to do more desilication experiments, and also to try another approach to create mesopores in the crystals.

Study on the deactivation mechanism of the catalyst could be interesting. A study has shown HNO_3 treatment selectively removes external surface acid sites from ZSM-22 crystals [65], it could be interesting to selectively dealuminate the external surface of the catalyst which might avoid formation of coke on the external surface of the catalyst, which in turn might improve the life time of the catalyst.

It could be interesting to co-feed C_3^+ olefins to methanol and see whether it lead to additional olefins formations. Co-feeding of methylbenzenes (eg. toluene) could also be a source of voluble in formation.

There are other 10-ring unidirectional zeolites, with slight differences in the dimensions and shapes of the 10-ring channel (eg. ZSM-23 and ZSM-48). The effect of slight variation in the channel dimensions on the product spectrum of the MTH reaction could be studied using these catalysts. A SUZ-4 zeolite (see Appendix 5) has 10-ring straight channels interconnected by zigzag 8-ring channels, creating a bigger free space at the channel interactions. It could be interesting to see the effect of the zigzag 8-ring channels and the free space at the channel interactions on the product spectrum of the MTH reaction.

APPENDIX

APPENDIX 1

List of reagents

Reagents used in the synthesis and characterization of ZSM-22

Reagent	Composition	Supplied by
1,8-diaminooctane	$C_8H_{20}N_2$	FLUKA
1-ethylpyridinum bromide	$C_7H_{10}BrN$	MERCK
Aluminum standard	Al	FLUKA
Aluminum sulphate	$Al_2(SO_4)_3.16H_2O$	J. T. Baker
Dichloromethane	$CH_2\ Cl_2$	BDH Laboratory
Diethylamine	$C_2H_{11}N$	FLUKA
Hydrofluoric acid	HF	Merck
LUDOX AS-30	SO_2	SIGMA ALDRICH
Methanol	CH_3OH (^{12}C)	BDH Laboratory
Methanol	CH_3OH (^{13}C)	ICON
Potassium hydroxide	KOH	MERCK
Silicon standard	Si	FLUKA
Sodium hydroxide	NaOH	MERCK
Sulphuric acid	H_2SO_4	MERCK
Water	H_2O (deionised)	---
Water glass (40 wt%)	SO_2	KEBOLabAB

APPENDIX 2

Calculations

Methanol conversion (%), selectivity (%), and yield (%) was calculated from the integrated area of peaks generated by GC-FID.

Methanol conversion was calculated as

$$Conversion = \frac{\sum area\ of\ all\ compounds - area\ of\ (MeOH + DME)}{\sum area\ of\ all\ compounds} \cdot 100$$

Selectivity for a given compound *x* was calculated as

$$Selectivity\ (X) = \frac{area\ of\ compound\ X}{\sum area\ of\ all\ products} \cdot 100$$

Yield for a given compound *x* was calculated as

$$Yield\ (X) = \frac{Convertion\ \cdot\ Selectivity\ (X)}{100}$$

APPENDIX 3

Synthesis of ZSM-22

1. Synthesis using 1-ethylpyridinum bromide as structure directing agent

The following conditions were common for all the syntheses of ZSM-22 using 1, 8-diaminoocatane as a structure directing agent.

- $Al_2(SO_4)_3.16H_2O$ was used as a source of Al
- Water glass (30 wt%) was used as a source of Si
- KOH was used as a source of K
- The crystallization occurred at 160 °C

Table A3.2 syntheses using 1—ethylpyridinium bromide as structure directing agent

Syn. no.	Gel Si/Al	Ageing at room temp.	Crystallization time (days)	Crystallization conditions	Result
1.1	15	--	4 days	Static	ZSM-22 + amorphous
1.2	29	--	4 days	Static	ZSM-22 + amorphous
1.3	40	--	4 days	Static	ZSM-22
1.4	57	--	4 days	Static	ZSM-22
1.5	100	--	4 days	Static	ZSM-22 + cristobalite

2. Synthesis using diethylamine as structure directing agent

The following conditions were common for all the syntheses of ZSM-22 using 1, 8-diaminoocatane as a structure directing agent.

- $Al_2(SO_4)_3.16H_2O$ was used as a source of Al
- Water glass (40 wt%) was used as a source of Si
- NaOH was used as a source of Na
- The crystallization occurred at 170 °C

Table A3.2 syntheses using diethyamine as structure directing agent

Syn. no.	Gel Si/Al	Ageing at room temp.	Crystallization time	Crystallization conditions	Result
2.1	15	--	48 h	Vertical rotation	ZSM-22
2.2	30	--	48 h	Vertical rotation	ZSM-22
2.3	45	--	48 h	Vertical rotation	ZSM-22 + amorphous
2.4	23	--	48 h	Vertical rotation	ZSM-22 + amorphous
2.5	37	--	48 h	Vertical rotation	ZSM-22 + amorphous
2.6	45	--	72 h	Vertical rotation	ZSM-22 + amorphous
2.7	45	--	72 h (seed)	Vertical rotation	ZSM-22 + ZSM-5
2.8	60	--	72 h	Vertical rotation	ZSM-22 + ZSM-5
2.9	75	--	72 h	Vertical rotation	ZSM-22 + ZSM-5

In both Table A3.1 and Table A3.2, the syntheses resulted in pure ZSM-22 catalyst are reproducible.

3. Syntheses using 1, 8-diaminoocatane as structure directing agent

The following conditions were common for all the syntheses of ZSM-22 using 1, 8-diaminoocatane as a structure directing agent.

- $Al_2(SO_4)_3.16H_2O$ was used as a source of Al
- LUDOX AS-30 was used as a source of Si
- KOH was used as a source of K
- The crystallization occurred at 160 °C

Table A3.3 syntheses using 1, 8-diaminooctane as structure directing agent

Syn. no.	Gel Si/Al	Ageing at room temp.	Crystallization time (hours)	Crystallization conditions	Result
3.1	45	24 h	72 h	Static	ZSM-11
3.2	45	24 h	72 h	Horizontal stirring	ZSM-22 + trace cristobalite
3.3	45	24 h	72 h	Vertical rotation	ZSM-22
3.4	45	24 h	72 h	Vertical rotation	ZSM-22
3.5	45	24 h	72 h	Vertical rotation	ZSM-22
3.6	45	24 h	72 h	Vertical rotation	ZSM-22
3.7	45	24 h	72 h	Vertical rotation	ZSM-22
3.8	45	24 h	72 h	Vertical rotation	ZSM-22
3.9	30	24 h	72 h	Vertical rotation	ZSM-22
3.10	130	24 h	72 h	Vertical rotation	ZSM-22 + cristobalite + ZSM-5
3.11	180	24 h	72 h	Vertical rotation	ZSM-22 + cristobalite + ZSM-5
3.12	220	24 h	72 h	Vertical rotation	ZSM-22 + cristobalite + ZSM-5
3.13	130	24 h	36 h	Vertical rotation	ZSM-22 + cristobalite + ZSM-5
3.14	180	24 h	36 h	Vertical rotation	ZSM-22 + cristobalite + ZSM-5
3.15	220	24 h	36 h	Vertical rotation	ZSM-22 + cristobalite + ZSM-5
3.16	130	24 h	60 h	Static	ZSM-22 + cristobalite + ZSM-5
3.17	180	24 h	60 h	Static	ZSM-22 + cristobalite + ZSM-5
3.18	220	24 h	60 h	Static	ZSM-22 + cristobalite + ZSM-5
3.19	130	--	13 h	Horizontal stirring	ZSM-22 + amorphous
3.20	180	--	13 h	Horizontal stirring	ZSM-22
3.21	220	--	13 h	Horizontal stirring	ZSM-22 + cristobalite
3.22	45	24 h	72 h	Vertical rotation	ZSM-22
3.23	45	24 h	72 h	Vertical rotation	ZSM-22
3.24	45	24 h	72 h	Vertical rotation	ZSM-22
3.25	45	24 h	72 h	Vertical rotation	ZSM-22
3.26	30	24 h	72 h	Vertical rotation	ZSM-22

The of composition the gel (Si/Al = 45) was 8.9 K_2O : Al_2O_3 : 90 SiO_2 : 3 K_2SO_4 : 27.3 DAO : 3588 H_2O. To change the Si/Al ratio of the gel, the amount of $Al_2(SO_4)_3.16H_2O$ was changed. To change the Si/Al ratio of the gel, the amount of $Al_2(SO_4)_3.16H_2O$ was changed.

In the syntheses Tables (Table A3.1, Table A3.2 and Table A3.3), syntheses that resulted in a completely a different phase or amorphous without ZSM-22 crystals are not included.

APPENDIX 4

Calculation of GC-MS response factor

Two mixtures containing triMB, pentaMB, hexaMB, naphtalene and CH_2Cl_2 (containing hexachloroethane standard) were prepared with different concentrations.

	TriMB	pentaMB	hexaMB	napthalene	CH_2Cl_2
Mixture 1	4.1 mg	5 mg	5 mg	5 mg	100 mL
Mixture 2	4.1 mg	5 mg	5 mg	5 mg	200 mL

Mixture 1 and 2 were analyzed using GC-MS. The syringe was rinsed with CH_2Cl_2 (without standard), and a pure CH_2Cl_2 was injected into the GCMS. This was performed to check the syringe was clean enough. After the blank run was over, the two mixtures were analyzed. A blank analysis was performed between the two mixtures, to be sure that no residuals were present in the syringe. For each compound in the calibration mixture, including hexachloroethane standard, the Total ion-chromatogram was integrated. The following procedure was followed to calculate the calibration factor for each aromatic compound.

The concentration of each aromatic compound is given by

$$C_{mg/L}(x) = \frac{M_{mg}(x)}{V_L(cal.mix)}$$

Where $C_{mg/L}\ (x)$: Concentration of aromatic compound x in milligram per litter, $M_{mg}\ (x)$: mass of aromatic compound x dissolved in the mixture, in milligrams, $V_L\ (cal.mix)$: Volume of the calibration mixture in litter. The relative Total ion-chromatogram area of the aromatic compound x was calculated using

$$A_{rel}(x) = \frac{A_{obs}(x)}{A_{obs}(std)}$$

The response factor is then calculated as

$$K_{L/mg}(x) = \frac{A_{rel}(x)}{C_{mg/L}(x)}$$

Where $K_{mg/L}\ (x)$: response factor for a compound x in milligram

APPENDIX 5

Synthesis and characterization of SUZ-4

SUZ-4 zeolite is known by the three letter IUPAC code SZR. The framework of SUZ-4 consists of 4-, 5-, 6-, 8- and 10-membered rings of three dimensional channel systems. It has orthorhombic unit cell with dimensions of a = 18.8696, b = 14.4008, and c = 7.5140 Å [10]. The 10-membered ring channels of SUZ-4 are the main straight channels in the framework and they are interconnected by zigzag 8-ring channels as illustrated in Figure A5.1.

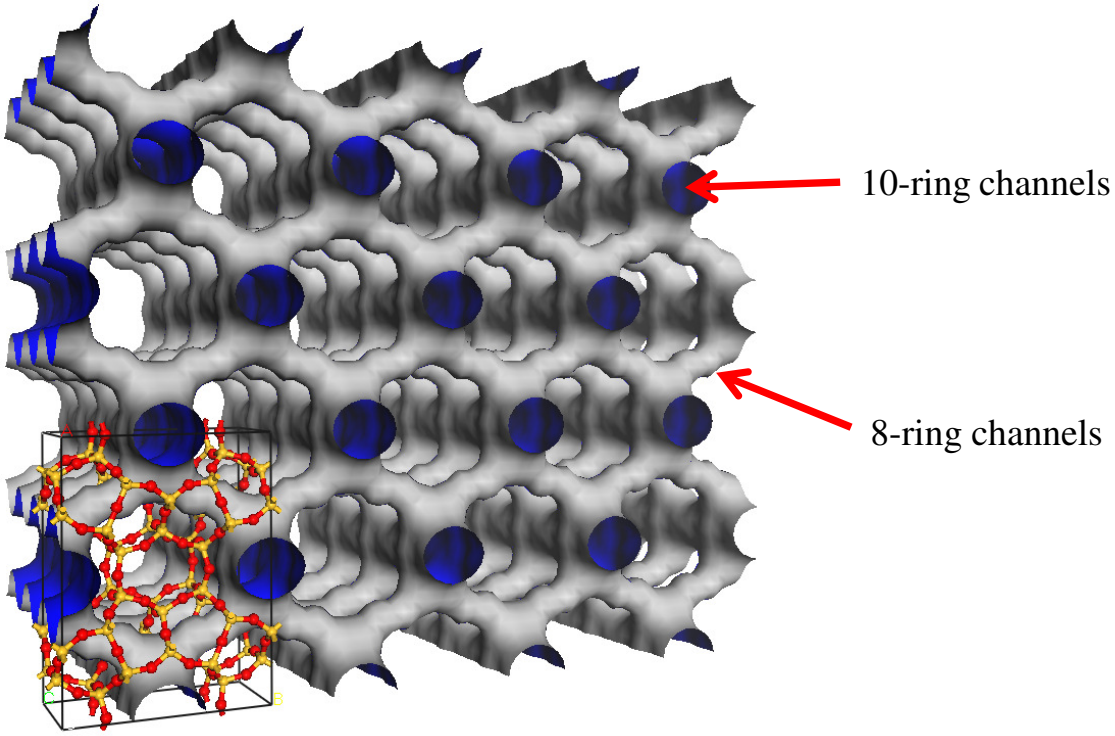

Figure A5.1 illustration of the pore system of SUZ-4 zeolite, note that the 4- 5- and 6- ring cannels are removed in the illustration as they too narrow to be accessed by a reactant molecules.

The 10-ring straight channels of SUZ-4 zeolite are 4.6 x 5.2 Å in dimensions, slightly smaller than the 10-ring straight channels of ZSM-22 (4.6 x 5.7 Å). However, at the channel intersections, SUZ-4 has bigger free space.

It could be interesting to see the catalytic activity of SUZ-4 for the MTH reaction, and to find out the effect of the zigzag 8-rings on the product spectrum. In the following section the synthesis of SUZ-4 and XRD diffraction patterns and SEM images of the product are presented.

Synthesis of SUZ-4

A SUZ-4 zeolite was synthesized according to the procedure in reference [83]. The following solutions were prepared

i. 0.4 g Al-wire was dissolved in KOH solution (3.3 g KOH + 50.6 g water)
ii. 7.93 g TEAOH (25 wt %)
iii. 18.23 g LUDOX AS-40 (40 wt %)

To the clear solution i, solution ii and solution iii were added successively while stirring at 60 °C. The batch composition of the synthesis mixture was 7.92 K_2O : Al_2O_3 : 16.21 SiO_2 : 1.83 TEAOH : 507 H_2O. The gel was transferred to 40 ml Teflon lined stainless steel autoclaves. The Si/Al ratio was varied by changing the amount of Al-wire dissolved in KOH solution. Crystallization of the gel was carried out under horizontal stirring conditions at 160 °C. After crystallization was complete, the reaction mixture was diluted with distilled water and the product was recovered by filtration. The resulting product was washed and dried overnight at 90 °C.

Table A5.1 synthesis conditions used during the crystallization of SUZ-4 zeolite

Syn. no.	Gel Si/Al	Ageing at room temp.	Crystallization time	Crystallization conditions	Result
SUZ-4-1	8	--	2 days	Horizontal stirring	SUZ-4 + amorphous
SUZ-4-2	8	--	5 days	Horizontal stirring	SUZ-4
SUZ-4-3	13	--	3 days	Horizontal stirring	SUZ-4
SUZ-4-4	17	--	2 days	Horizontal stirring	amorphous

Characterization of SUZ-4

Figure A5.2 display the XRD diffraction profiles of SUZ-4 having Si/Al ratio of 8 and 13 in the synthesis gel. The synthesis product is free from structural impurities. Figure A5.3 displays SEM image of SUZ-4 catalyst having Si/Al = 8. The crystals were needle shaped and ~2-3 µm in length.

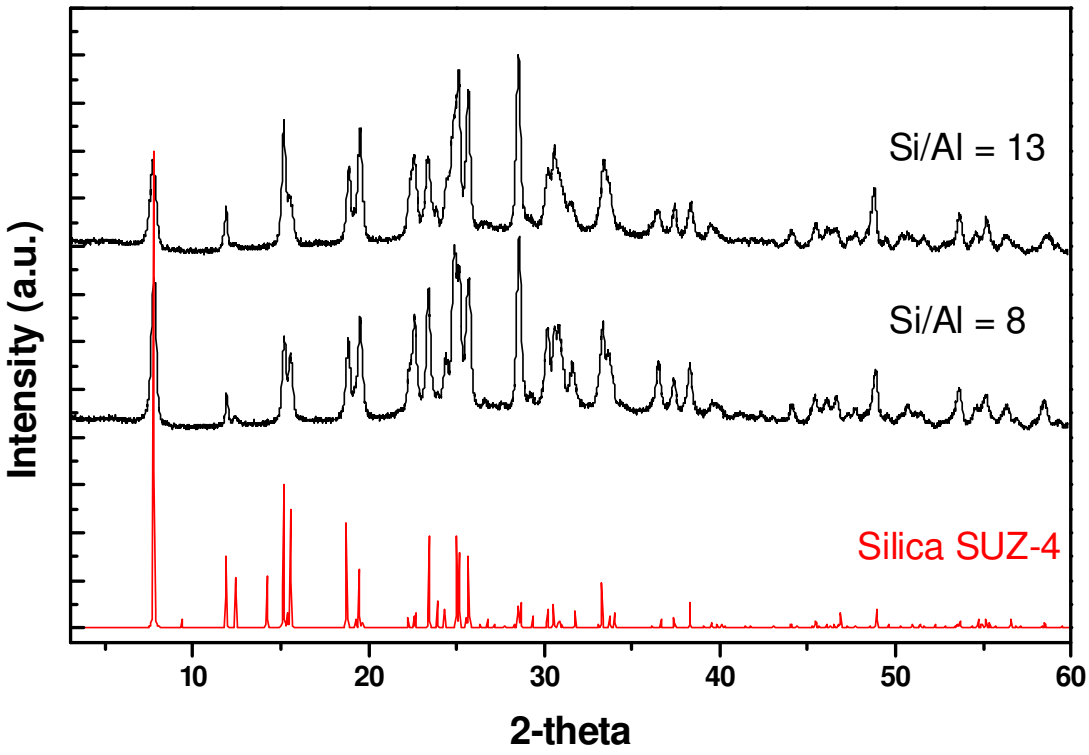

Figure A5.2 XRD diffraction profile of SUZ-4 having gel Si/Al = 8 and 13, synthesis number SUZ-4-2 and SUZ-4-3 in Table A5.1.

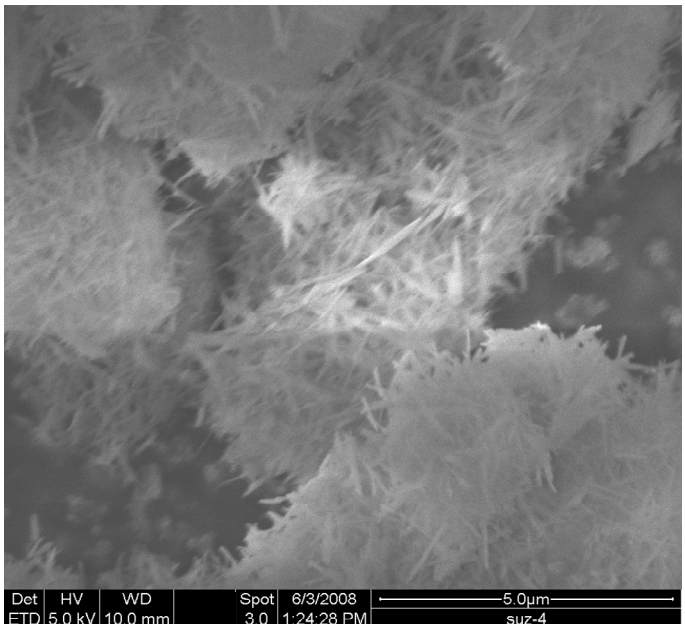

Figure A5.3 SEM image of SUZ-4 having gel Si/Al = 8, synthesis number SUZ-4-2 in Table A5.1.

APPENDIX 6

Supplementary information

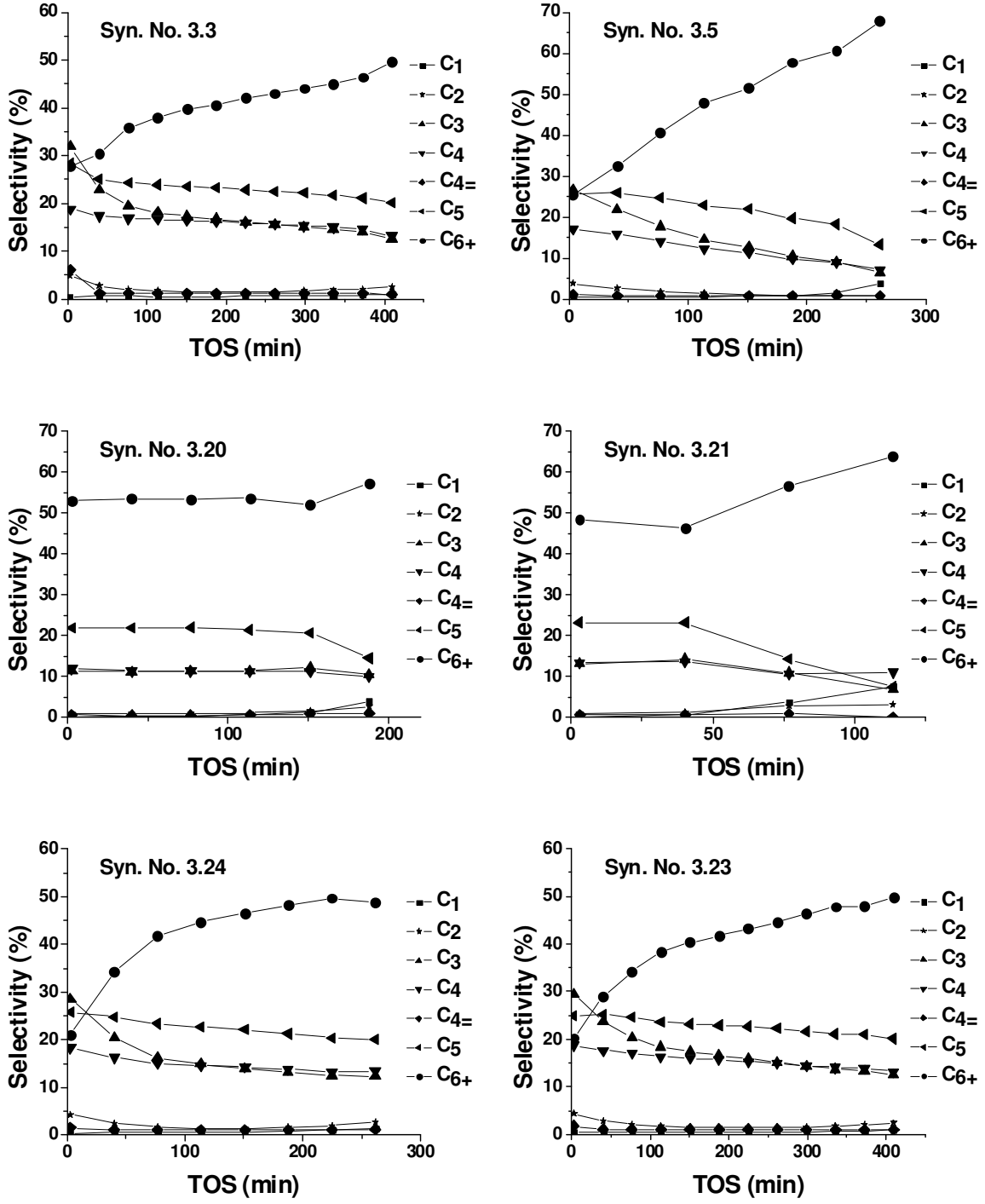

Figure A6.1 Product selectivity of the MTH reaction over ZSM-22 catalysts at 400 °C, WHSV = 2 $gg^{-1}h^{-1}$

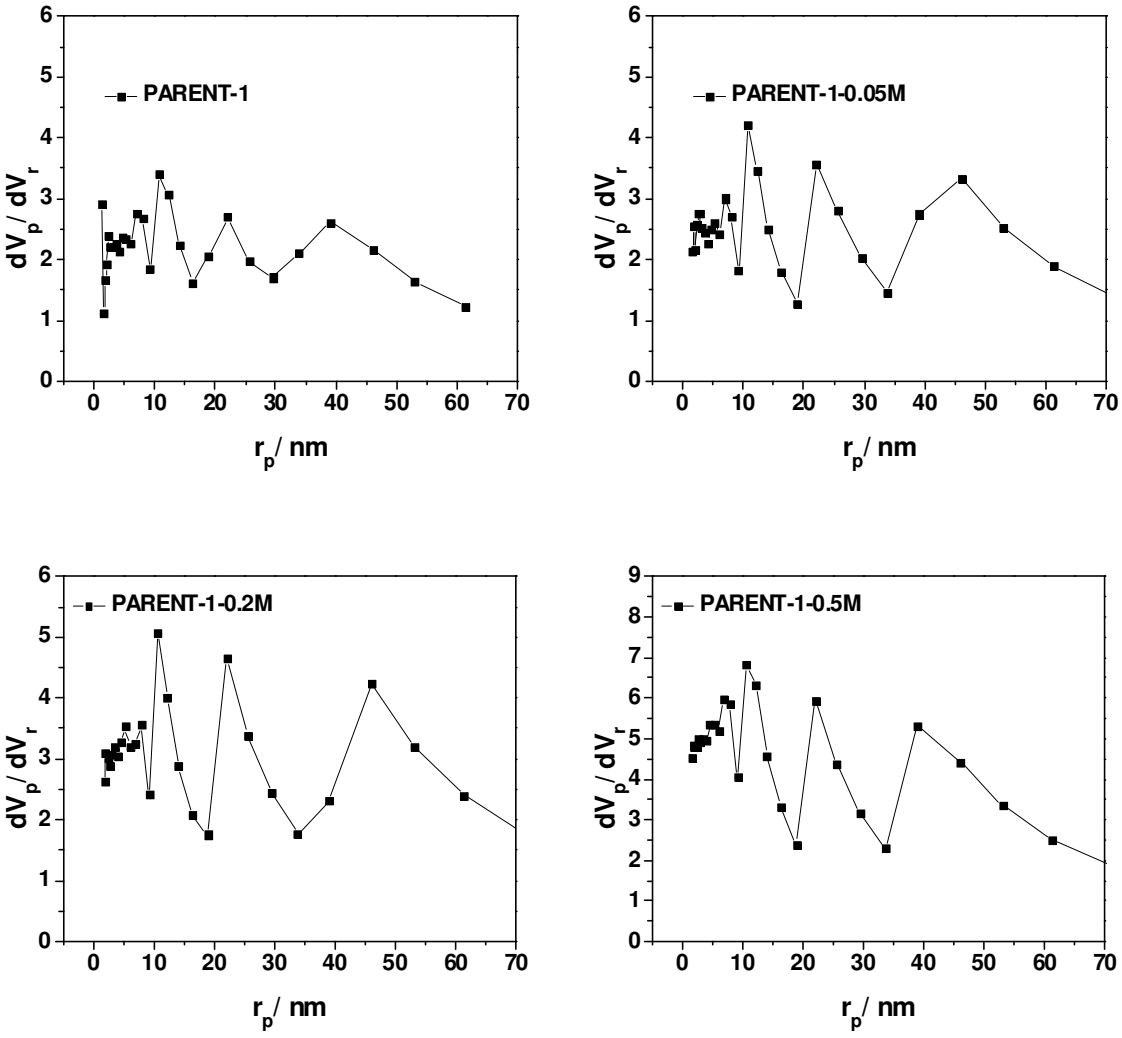

Figure A6.2 BJH mesopore distribution plots of ZSM-22 catalysts

APPENDIX 7

Paper accepted for publication in *chemcatchem*, 2009.

COMMUNICATION

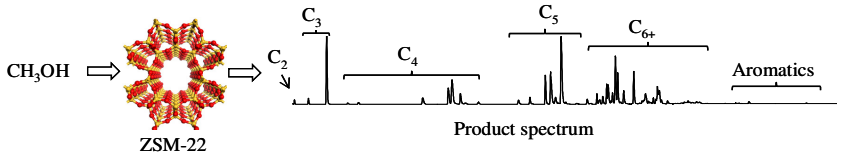

Shape selectivity gives unique product spectrum: A zeolite catalyst previously believed to be inactive in the conversion of methanol to hydrocarbon is now found to yield a unique product rich in branched C_{5+} alkenes without the formation of aromatic products. This discovery has potential implications for the production of cleaner transportation fuels from natural gas or biomass.

*Shewangizaw Teketel, Stian Svelle, Karl-Petter Lillerud, Unni Olsbye**

Page No. – Page No.

Shape selective conversion of methanol-to-hydrocarbons over 10-ring unidirectional channel acidic H-ZSM-22

DOI: 10.1002/cctc.200((will be filled in by the editorial staff))

Shape selective conversion of methanol-to-hydrocarbons over 10-ring unidirectional channel acidic H-ZSM-22

Shewangizaw Teketel[a], Stian Svelle[a], Karl-Petter Lillerud[a], Unni Olsbye*[a]

With the forecasted depletion in global oil reserves, new routes to petrochemical products from natural gas, coal or biomass are becoming increasingly important. The methanol-to-hydrocarbons (MTH) reaction constitutes the final step in one such route. The MTH reaction proceeds over Brønsted-acidic zeolite or zeotype catalysts, and near-commercial processes exist for the methanol to gasoline (MTG) reaction over ZSM-5, as well as the methanol to olefin (MTO) reaction over SAPO-34.[1] A breakthrough in the mechanistic understanding of the MTH reaction was the formulation of the "hydrocarbon pool mechanism" by Dahl and Kolboe,[2, 3] which postulates that methanol is continuously added to aromatic reaction centers from which light alkenes are split off in later reaction steps.[4] Recently, the importance of methylation and cracking of alkenes was highlighted for ZSM-5.[5, 6] ZSM-22 (TON) is less studied[7-10] as MTH catalyst and has one dimensional non-interacting 10-ring channels with diameters of 0.46 x 0.57 nm.[11] Cui and et al.[7-9] reported the failure of ZSM-22 to convert methanol to olefins. Their studies of ZSM-22 showed a low production of olefins during the first pulses of methanol, however the amount of olefin quickly decreased to essentially zero. This failure as MTH catalyst was ascribed to the narrow pores, which were assumed to be too small to accommodate the complete catalytic cycle of the hydrocarbon pool mechanism. Flow experiments (at 250 to 400 °C) showed relatively constant yields of trace amounts of ethene and propene. The low reactivity was believed to be the result of traces of ZSM-11, impurities in the methanol (acetone) and/or external acid sites. In this communication we report studies of the MTH reaction over ZSM-22 at a wider range of reaction conditions and find that the previous conclusions[7-10] are not universally valid. At suitable conditions, ZSM-22 has conversion capacity comparable to that of SAPO-34, reaction intermediates reside within the pores, and the product spectrum is intermediate to those found in MTO and MTG.

Several batches of ZSM-22 with different Si/Al ratios were synthesized and all were found to be active catalysts for the MTH reaction. XRD confirmed the crystallinity and purity of the product. SEM revealed needle shaped crystals of 2-3 µm length. ^{27}Al-NMR showed that, for the samples discussed here, Al is located exclusively in the framework, both for as-made and calcined/ion-exchanged samples. BET surface areas were in the range 160 – 207 m^2g^{-1}. Two ZSM-22 catalysts (Si/Al = 30 by ICP-AES) with BET surface areas of 173 and 207 m^2g^{-1}, denoted ZSM-22(173) and ZSM-22(207) respectively, will be discussed.

Figure 1 (left) shows the conversion of methanol over ZSM-22(173) (WHSV = 2.05 h^{-1}) as a function of time on stream (TOS) at different reaction temperatures. At temperatures above 350 °C, the initial conversion is 100 % and appreciable conversion is observed for several hours. However, deactivation is very rapid at 350 °C. Note that the feed rate is lower than in other studies: WHSV = 48 h^{-1} was used by Cui et al.[8] and WHSV = 10 h^{-1} was used by Li et al.[10]

Figure 1 (right) displays the total conversion capacity, defined as the amount (in grams) of methanol converted to products per gram catalyst before complete deactivation (see [12]). At 450 and 500 °C the conversion capacities are close to 12 gg^{-1}. Bleken et al. [13] have studied the MTH reaction over SAPO-34 and SSZ-13 (the zeolite analogue) catalysts with an acid site density corresponding to Si/Al = 11, and found a maximum conversion capacity of ~25 gg^{-1}. Thus, if the difference in acid site concentration (a factor 3) is considered, the amount of methanol converted to hydrocarbons over ZSM-22 catalyst is slightly larger than the amount of methanol converted over SAPO-34 and SSZ-13 per acid site before deactivation. [13] We note that the ZSM-22(207) catalyst displays a higher conversion capacity than ZSM-22(173) at 400 °C (see Table 1 below), thereby outperforming SAPO-34 in this respect.

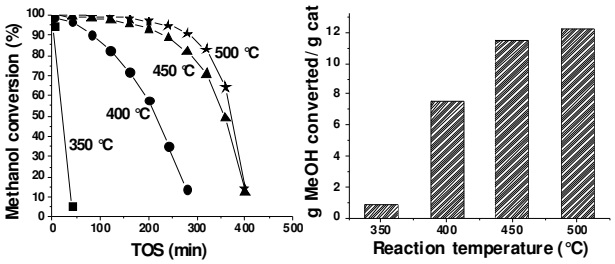

Figure 1. Effect of temperature on methanol conversion (%) over ZSM-22(173) as a function of time on stream (left) and gram amount of methanol converted per gram catalyst before complete deactivation (right). WHSV = 2.05 h^{-1}.

The product selectivites were studied in detail for ZSM-22(207). Figure 2 displays the product selectivity (left) and the composition of the C_{5+} fraction (right) as a function of TOS. Selectivity for C_3 (mostly propene) was highest initially and decreased with increasing deactivation. There was a gradual decrease in the C_4 and C_5 selectivities with deactivation. A remarkable increase for the C_{6+} fraction was observed with progressive deactivation of the catalyst. Notably, very little C_2 is formed. The C_{5+} fraction was closely inspected (see Figure 2 and Supporting Information), and branched alkenes were the most abundant (70 %) and, linear and cyclic alkenes were the second and third most abundant products. Interestingly, very little aromatics (~1 %) were observed, which we attribute to the unique shape selectivity induced by the non-intersecting 10-ring pores.[14] The product spectrum in the MTH reaction over ZSM-22 is intermediate to that

[a] S. Teketel, Assoc. Prof. S. Svelle, Prof. K.P. Lillerud, Prof. U. Olsbye
inGAP Senter for forskningsdrevet innovasjon
Senter for materialvitenskap og nanoteknologi
Kjemisk institutt, Universitet i Oslo
P.O. Box 1033 Blindern, N-0315
Oslo, Norway
Fax: (+47) 22-85-54-41
E-mail: unni.olybye@kjemi.uio.no

Supporting information for this article is available on the WWW under http://dx.doi.org/10.1002/cctc.200xxxxxx.

found for SAPO-34 and ZSM-5, and this might provide product flexibility in an MTH application. Ideally, gasoline should consist of branched alkanes with mainly five to ten carbon atoms and there are limits on aromatic content.[15] The ZSM-22 MTH product meets these requirements and might be suitable as gasoline after hydrogenation. Alternatively, the alkene rich product might be utilized as an alkylation feedstock to increase the carbon number and provide saturation.

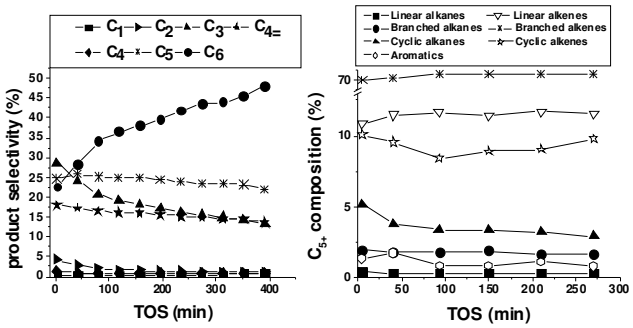

Figure 2. Product selectivity (C%) as a function of time on stream, selectivity for C_1 to C_{6+} hydrocarbons (left) and alkane, alkene, aromatics selectivity in C_{5+} fraction (right). Reaction carried out at 400 ℃ over ZSM-22(207), WHSV = 2.05 h^{-1}.

Table 1 displays the effect of feed rate on methanol conversion as a function of time on stream. WHSV = 2.05, 3.03 and 4.05 h^{-1} were used for this investigation. The catalysts were deactivated more rapidly with a modest increase in feed rate. It has been shown that at very high feed rates (~ 300 h^{-1}) the hydrocarbon pool reactions responsible for methanol conversion may be suppressed for ZSM-5.[6] Cui et al. studied the MTH reaction over ZSM-22 at a high feed rate (48 h^{-1}) which is probably high enough to suppress hydrocarbon pool formation and secondary reactions for this catalyst. The conversion capacity, last line in Table 1, also suffers from increased feed rate.

Table 1. Effect of feed rate on methanol conversion (%) over ZSM-22(207) as a function of time on stream at 400 ℃.

TOS[a]	2.05[b]	3.03[b]	4.05[b]
3	99	99	98
40	97	63	46
80	93	53	30
120	89	40	9
gg^{-1}	12.0	5.50	4.50

[a] TOS (min) [b] WHSV ($gg^{-1}h^{-1}$)

The hydrocarbons retained in deactivated ZSM-22(207) was investigated by dissolving the samples in HF, extracting the organics with CH_2Cl_2, and analyzing the extracts by GC-MS. Figure 3 shows the total ion chromatograms thus obtained for a series of catalysts after various methanol reaction times at 400 ℃. For deactivated catalysts higher concentration of hydrocarbons are seen and especially of heavier compounds. Clearly, selectivity for slim retained hydrocarbons was observed. This finding agrees well with the pore geometry of ZSM-22, evidenced by the absence of pyrene, which must be too big to fit into the channel. Polymethylbenzenes as small as trimethybenzene are linked to alkene formation,[5] and this indicates that hydrocarbon pool reaction mechanism is operative over ZSM-22. Small amounts of ethylbenzene and ethyltoluene were also observed. This may be related to intermediates in the synthesis of ethene, although ehtylbenzenes could also form by back reaction of ethene with aromatics[16]. Based on these findings we speculate that the retained hydrocarbons can sustain alkene formation. Once alkenes are produced, they can undergo further methylation and cracking, leading to net methanol conversion, and also to coking reactions.[17] This is related to the recently proposed dual cycle[5, 18] mechanism for methanol conversion, where both alkenes and aromatics my act, possibly independently, as intermediates for product formation in the MTH reaction.

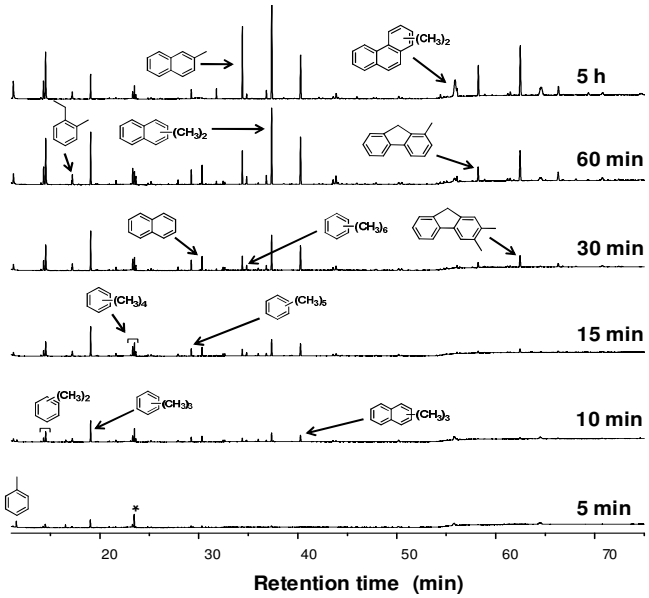

Figure 3. GC-MS total ion chromatogram of hydrocarbon extracts at different time on stream. Reaction carried out at 400 ℃ over ZSM-22(207), WHSV = 2.05 h^{-1}. (NB: all the peaks are normalized relative to the standard peak C_2Cl_6 indicated by * in the chromatogram)

Capillary X-ray diffractograms were recorded for the catalysts after feeding methanol for various times, Figure 4. Clearly, the crystallinity was retained. Importantly, low angle (2θ) peak intensities decreased slightly with increasing TOS.

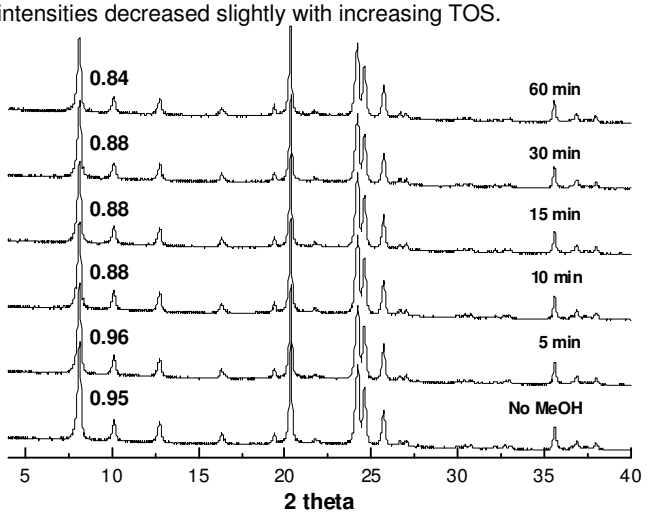

Figure 4. Capillary XRD profile of ZSM-22(207) after methanol feed for various times at 400 ℃, WHSV = 2.05 h^{-1}. The numbers are the ratios between the reflections at ~7 and ~20 °.

For zeolites, the low angle reflection intensities are sensitive to the presence of non framework species, whereas the high angle reflection intensities are determined mainly by atoms in the framework[19]. Thus, the decrease in low angle intensities can be explained by the formation of hydrocarbons in the channels of ZSM-22 catalyst, indicating that hydrocarbon pool mechanism occurs inside the 10 rings of the catalyst.

In conclusion, ZSM-22 zeolite is an active catalyst in the MTH reaction. Low feed rates and temperatures in the range 400-500 ℃ are required for appreciable conversion. The catalysts showed high selectivity for branched C_{5+} fraction alkenes which could be used for the production of cleaner gasoline. Aromatic reaction centers required for initial alkene formation were found to reside inside the narrow channels of ZSM-22, and it is proposed that

further conversion of methanol to a large extent proceeds via alkene methylation and cracking.

Experimental Section

Details on synthesis and characterization of representative samples are given in the Supporting Information.

Catalytic experiments were carried out in a fixed bed glass reactor (i.d. 10 mm) as described previously[13]. 50 mg of calcined and ion exchanged catalyst (particle size 0.25-0.42 mm) was used for each test. Before each test, the reactor was heated to 550 °C under a flow of helium. The catalysts were calcined *in situ* at this temperature under a flow of pure oxygen for one hour. The carrier gas, He, was saturated by methanol (BDH Laboratory supplies, >99.8% chemical purity) at 20 °C. The reactor effluent was analyzed by on-line GC.

The organic material retained in the catalyst after methanol conversion was analyzed by dissolving 20 mg of spent catalysts in 15% HF and analyzing the organic extract using GC-MS.[13]

Acknowledgements

S. Teketel acknowledges the Norwegian Quota Scheme for financial support.

Keywords: heterogeneous catalysis • methanol-to-hydrocarbon process • shape selectivity • zeolites • ZSM-22

[1] S. Kvisle, T. Fuglerud, S. Kolboe, K. P. Lillerud, U. Olsbye, I. V. Vora, in *Handbook of Heterogeneous Catalysis, Vol. 6*, **2008**, pp.2950-2965.
[2] I. M. Dahl, S. Kolboe, *J. Catal.* **1996**, *161*, 304-309.
[3] I. M. Dahl, S. Kolboe, *Catal. Lett.* **1993**, *20*, 329-336.
[4] B. Arstad, S. Kolboe, *Catal. Lett.* **2001**, *71*, 209-212.
[5] M. Bjørgen, S. Svelle, F. Joensen, J. Nerlov, S. Kolboe, F. Bonino, L. Palumbo, S. Bordiga, U. Olsbye, *J. Catal.* **2007**, *249*, 195-207.
[6] S. Svelle, P. A. Rønning, S. Kolboe, *J. Catal.* **2004**, *224*, 115-123.
[7] Z. M. Cui, Q. Liu, W. G. Song, L. J. Wan, *Angew. Chem.* **2006,** *118,* 6662-6665; *Angew. Chem. Int. Ed.* **2006**, *45*, 6512-6515.
[8] Z. M. Cui, Q. Liu, S. W. Baint, Z. Ma, W. G. Song, *J. Phys. Chem. C* **2008**, *112*, 2685-2688.
[9] Z. M. Cui, Q. Liu, Z. Ma, S. W. Bian, W. G. Song, *J. Catal.* **2008**, *258*, 83-86.
[10] J. Z. Li, Y. Qi, Z. M. Liu, G. Y. Liu, D. Z. Zhang, *Catal. Lett.* **2008**, *121*, 303-310.
[11] C. Baerlocher, W. M. Meier, D. H. Olsen, *Atlas of Zeolite Framework Types*, Elsevier, Amesterdam, **2001,** p.269.
[12] Ø. Mikkelsen, S. Kolboe, *Microporous Mesoporous Mater.* **1999**, *29*, 173-184.
[13] F. Bleken, M. Bjørgen, L. Palumbo, S. Bordiga, S. Svelle, K. P. Lillerud, U. Olsbye, *Top. Catal.* **2008,** 52, 218-228.
[14] J. F. Haw, W. G. Song, D. M. Marcus, J. B. Nicholas, *Acc. Chem. Res.* **2003**, *36*, 317-326.
[15] J. A. Moulijn, M. Makkee, A. V. Diepen, *Chemical Process Technology*, Jon Wiley and Sons, **2001,** p.88.
[16] D. M. Marcus, W. G. Song, L. L. Ng, J. F. Haw, *Langmuir* **2002**, *18*, 8386-8391.
[17] R. M. Dessau, R. B. Lapierre, *J. Catal.* **1982**, *78*, 136-141.
[18] S. Svelle, F. Joensen, J. Nerlov, U. Olsbye, K. P. Lillerud, S. Kolboe, M. Bjørgen, *J. Am. Chem. Soc.* **2006**, *128*, 14770-14771.
[19] B. Christian, B. M. Lynne, *Stud. Surf. Sci. Catal.***1994,** *85*, 391-428

Received: ((will be filled in by the editorial staff))
Published online: ((will be filled in by the editorial staff))

Supporting information

Shape selective conversion of methanol-to-hydrocarbons over 10-ring unidirectional channel acidic H-ZSM-22

Shewangizaw Teketel, Stian Svelle, Karl-Petter Lillerud, Unni Olsbye[*]

Catalyst synthesis

ZSM-22 catalysts were synthesized according procedures found in the literature.[1, 2] 1.05 g of aluminium sulphate (J. T. Baker) was added to 10.89 g of distilled water and the mixture was stirred until the aluminium sulphate was dissolved completely. A solution of 2.4 g of potassium hydroxide (MERCK) dissolved in 10.89 g of distilled water was prepared and mixed with the aluminium sulphate solution. Another solution of 6.26 g diaminooctane (FLUKA) dissolved in 43.6 g of distilled water was prepared and added to the first mixture. The resulting mixture was mixed very well and a solution of 2.05 g silica (LUDOX AS-30 collidal silica, SIGMA ALDRICH) in 16.14 g of distilled water was added under vigorous stirring. The batch composition of the synthesis mixture was 8.9 K_2O : Al_2O_3 : 90 SiO_2 : 3 K_2SO_4 : 27.3 DAO : 3588 H_2O. The final mixture was stirred for 30 min. After 24 hours ageing time at room temperature, the gel was transferred to 40 ml teflon lined stainless steel autoclaves. The crystallization was carried out for three days at 160 ℃ in a tumbling oven (25 rpm). Teflon coated bar magnets were used to enhance the gel mixing. Then, the reaction mixture was diluted with distilled water and the product was recovered by filtration. The resulting product was washed and dried overnight at 90 ℃. The template was removed by calcination under a flow of pure oxygen at 550 ℃ for 12 hours and ion exchanged 3 x 2 hours with 1M NH_4NO_3 at 70℃. The ion exchanged catalysts were calcined at 550 ℃ for 2 hours in static air, for 1 hour *ex situ* in a flow of pure oxygen, and for 1 hour *in situ* in the fixed bed reactor in a flow of pure oxygen prior to each catalytic experiment, to desorb ammonia.

Catalyst Characterization

The purity and crystallinity of the products were identified using X-ray diffraction on a Siemens D-5000 diffractometer using $CuK\alpha_1$ radiation (λ= 0.1541nm). SEM images were taken on a Quanta 200 F (FEI) instrument. BET measurements were performed using a BELSORP-mini II instrument. Elemental composition of the catalysts was determined by using Varian VISTA PRO CCD simulant ICP-AES instrument. ^{27}Al-NMR spectra were recorded using a Bruker Avance 200 DMX instrument.

Figure 1 displays the Powder X-ray diffraction (XRD) pattern of ZSM-22 catalysts having Si/Al ratios of 20, 30 and 80. The patterns obtained were similar to those found in literature.[1, 3] The catalysts were well crystalline and free from structural impurities.

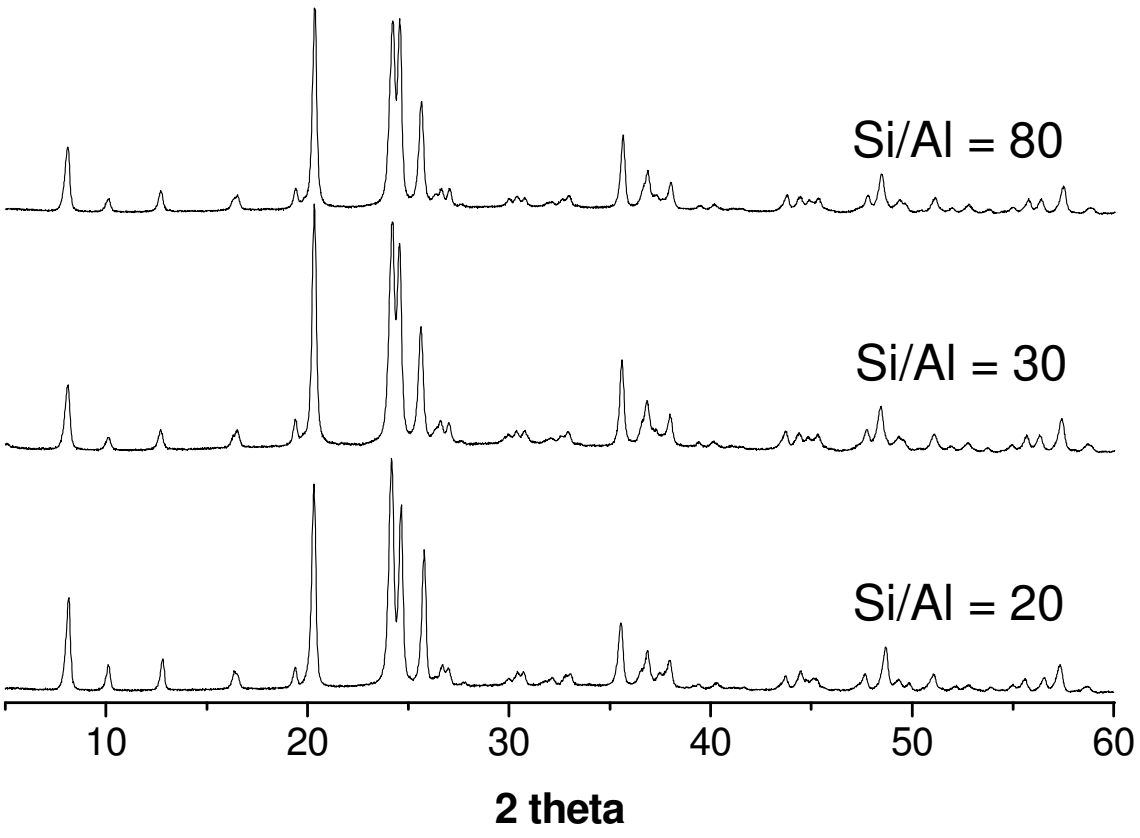

Figure 4. XRD diffraction pattern of as made ZSM-22 catalysts with different Si/Al ratios.

Figure 2 displays SEM images of a representative ZSM-22 catalyst (Si/Al = 80). The crystals were needle shaped and 2-3 µm in length. SEM images confirmed that there was no unreacted amorphous phase in the ZSM-22 catalysts.

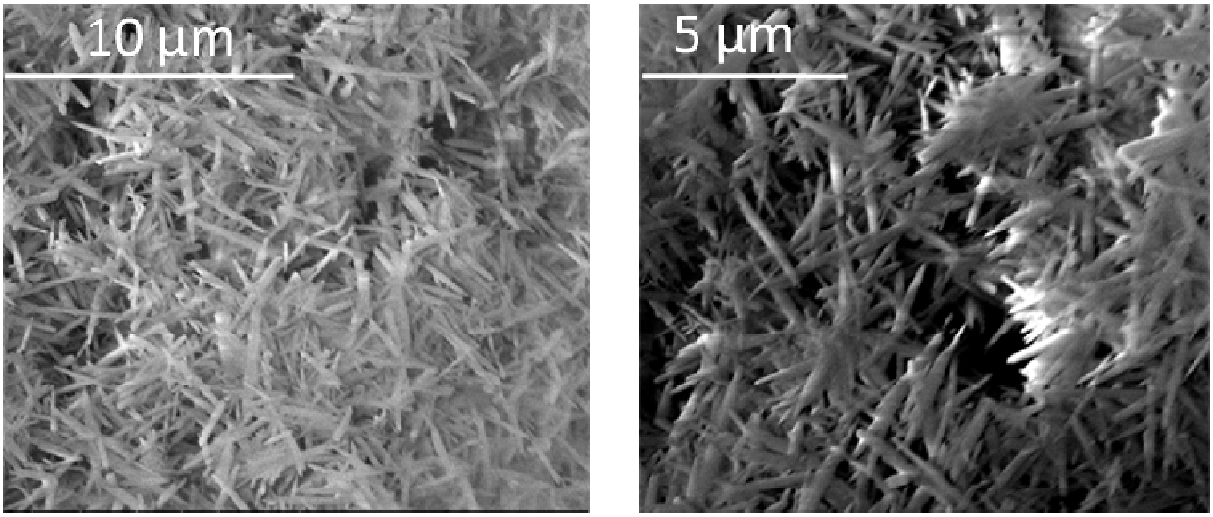

Figure 2. SEM images of ZSM-22 catalyst.

Figure 3 displays N_2 adsorption / desorption isotherms for ZSM-22(173) (left panel) and ZSM-22(207) (right panel) catalysts. The isotherms obtained were typical of microporous materials. The catalysts have BET surface areas of 173 and 207m^2g^{-1} respectively. Surface areas in this range have been reported previously for the same structure.[4, 5]

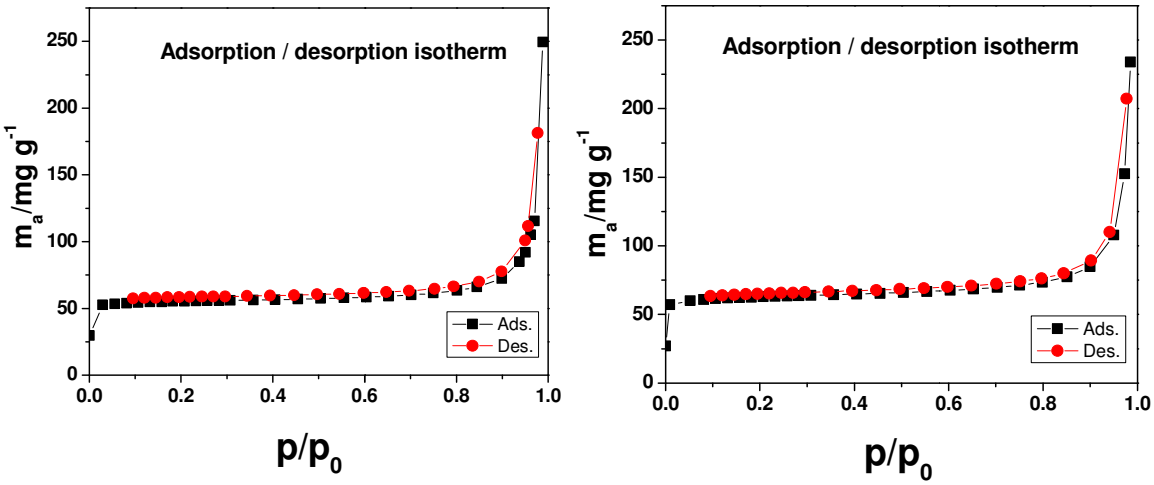

Figure 3. BET adsorption/ desorption isotherm of ZSM-22(173) (left panel) and ZSM-22(207) (right panel) catalysts.

Figure 4 displays ^{27}Al-NMR spectra for ZSM-22(173) and ZSM-22(207) catalysts. As seen from the spectra for as-made catalysts only one peak at about 50 ppm

corresponding to aluminum in tetrahedral framework positions is observed. Furthermore, calcination produces negligible amounts of extra framework aluminum at about 0 ppm.[6, 7]

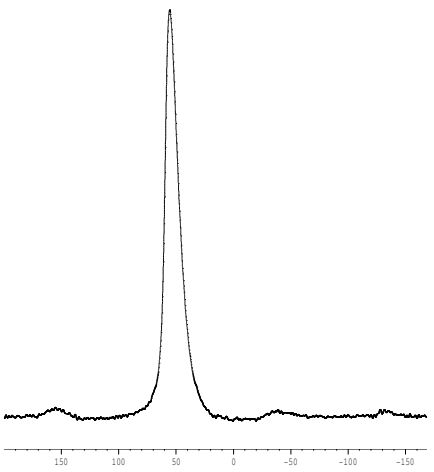

ZSM-22(173) as-made

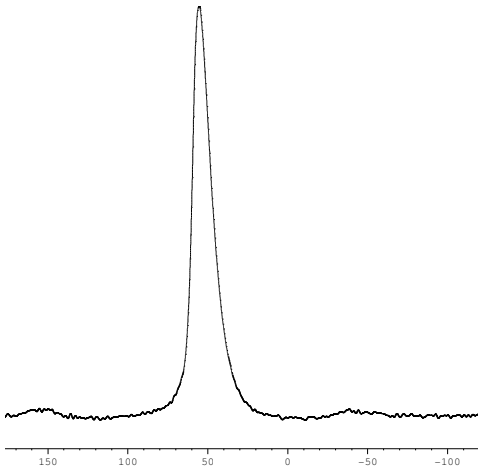

ZSM-22(207) as-made

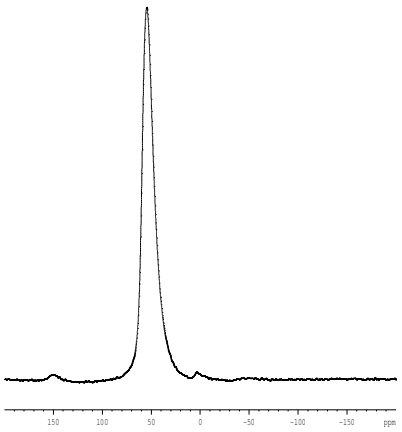

ZSM-22(173) calcined and ion exchanged

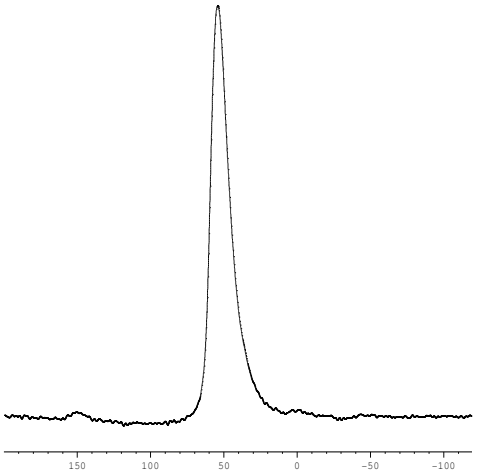

ZSM-22(207) calcined and ion exchanged

Figure 4. ^{27}Al-NMR spectra for as-made and calcined ZSM-22(173) and ZSM-22(207) catalysts. The peak at 50 ppm corresponds to framework aluminum; the small peak at 0 ppm corresponds to extra framework aluminum.

Figure 5 displays GC-MS total ion chromatograms of methanol to hydrocarbon reaction effluent over ZSM-22(207) catalyst as a function of time on stream (TOS), reaction carried out at 400 ℃, WHSV = 2.05 h^{-1}. The catalyst showed high selectivity

for propene in the C_1-C_4 fraction and for branched alkenes in C_{5+} fraction. Negligible amounts of aromatics (~ 1%) and very little C_2 were detected.

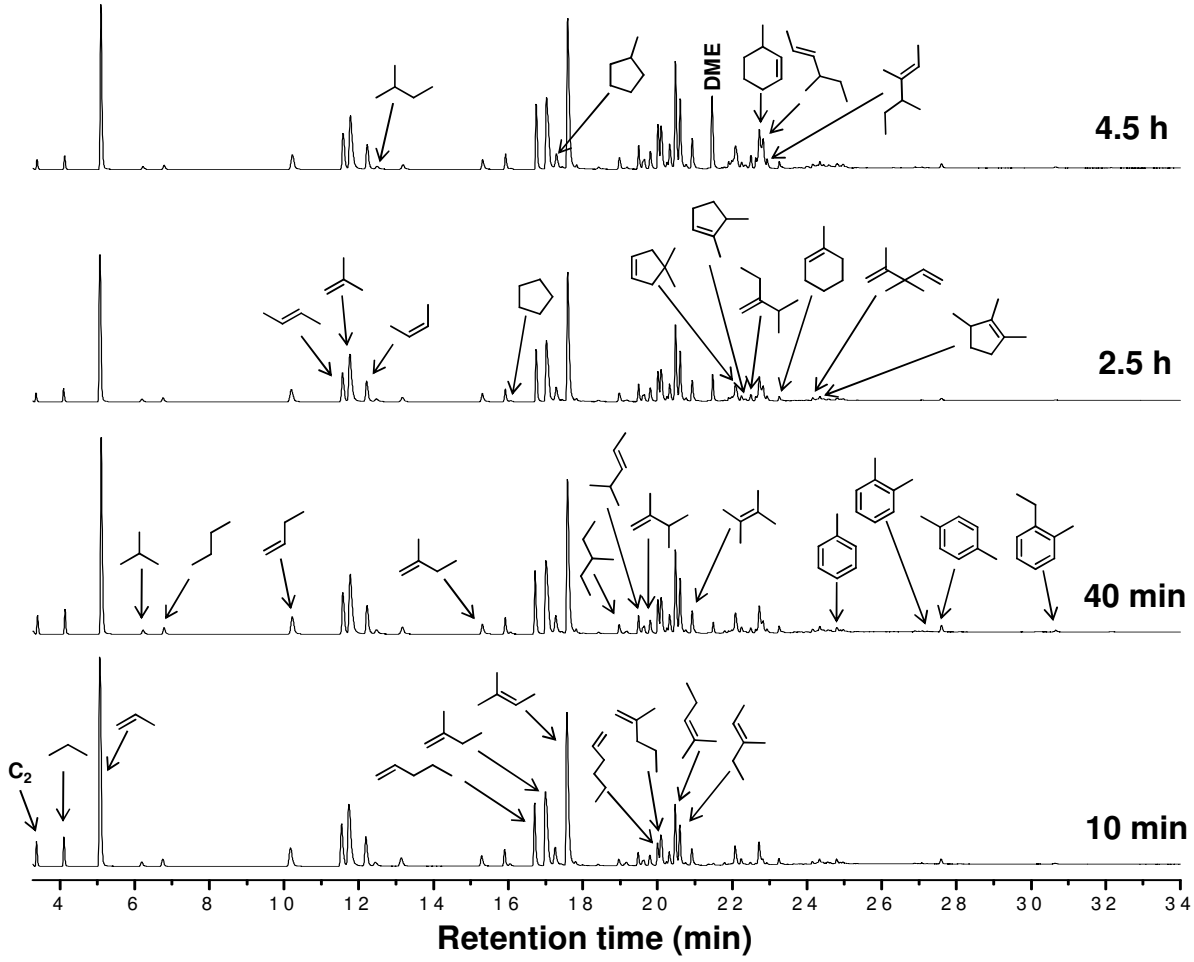

Figure 5. GC-MS total ion chromatograms of the MTH reaction effluent as a function of time on stream. The experiment was carried out at 400 ℃ over ZSM-22(207), WHSV = 2.05 h^{-1}. (NB: C_1 is not shown in the chromatogram)

Reference

[1] D. Masih, T. Kobayashi, T. Baba, *Chem. Commun.* **2007**, 3303-3305.

[2] H. Robson, K. P. Lillerud, *Verified Synthesis of Zeolitic Materials*, Elsevier, Amsterdam, **2001,** p.258.

[3] N. Kumar, L. E. Lindfors, R. Byggningsbacka, *Appl. Catal. A,* **1996**, *139*, 189-199.

[4] J. Z. Li, Y. Qi, Z. M. Liu, G. Y. Liu, D. Z. Zhang, *Catal. Lett.* **2008**, *121*, 303-310.

[5] K. Hayasaka, D. Liang, W. Huybrechts, B. R. De Waele, K. J. Houthoofd, P. Eloy, E. M. Gaigneaux, G. van Tendeloo, J. W. Thybaut, G. B. Marin, J. F. M. Denayer, G. V. Baron, P. A. Jacobs, C. E. A. Kirschhock, J. A. Martens, *Chem. Euro. J.* **2007**, *13*, 10070-10077.

[6] M. Derewinski, P. Sarv, A. Mifsud, *Catal. Today* **2006**, *114*, 197-204.

[7] H. V. Bekkum, E. M. Flanigen, P. A. Jacobs, J. C. Jansen, *Introduction to Zeolite Science and Practice*, Elsevier, **2001,** p.405.

REFERENCES

[1] I. Chorkendorff, J. W. Niemantsverdriet, *Concepts of Modern Catalysis and Kinetics*, WILEY-VCH, Weinheim, **2003**.

[2] C. Baerlocher, W. M. Meier, D. H. Olsen, *Atlas of Zeolite Framework Types*, Elsevier, Amesterdam, **2001**.

[3] A. Dyer, *An Introduciton to Zeolite Molecular Sieves*, John Wiley & Sons, Chichester.

[4] L. B. McCusker, F. Liebau, G. Engelhardt, *Pure Applied Chem.* **2001**, *73*, 381-394.

[5] A. Corma, *J. Catal.* **2003**, *216*, 298-312.

[6] M. Guisnet, J.-P. Gilson, *Zeolites for Cleaner Technologies, Vol. 3*, Imperial College Press, London, **2001**.

[7] J. F. Haw, J. B. Nicholas, T. Xu, L. W. Beck, D. B. Ferguson, *Acc. Chem. Res.* **1996**, *29*, 259-267.

[8] B. Smit, T. L. M. Maesen, *Nature* **2008**, *451*, 671-678.

[9] B. Marler, *Zeolites* **1987**, *7*, 393-397.

[10] http://www.iza-structure.org/databases/.

[11] G. T. Kokotailo, J. L. Schlenker, F. G. Dwyer, E. W. Valyocsik, *Zeolites* **1985**, *5*, 349-351.

[12] S. Kvisle, T. Fuglerud, S. Kolboe, K. P. Lillerud, U. Olsbye, I. V. Vora, *Handbook of Heterogeneous Catalysis, Vol. 6*, **2008**.

[13] http://rru.worldbank.org/documents/publicpolicyjournal/279gerner.pdf,

[14] M. Stocker, *Microporous Mesoporous Mater.* **1999**, *29*, 3-48.

[15] J. F. Haw, D. M. Markus, *Handbook of Zeolite Science and Technology*, New York, **2003**.

[16] J. Q. Chen, A. Bozzano, B. Glover, T. Fuglerud, S. Kvisle, *Catal. Today* **2005**, *106*, 103-107.

[17] http://www.lurgi.de/website/fileadmin/user_upload/pdfs/19_Methan-Propylen-E_rev060707.pdf.

[18] T. Mole, J. A. Whiteside, D. Seddon, *J. Catal.* **1983**, *82*, 261-266.

[19] T. Mole, G. Bett, D. Seddon, *J. Catal.* **1983**, *84*, 435-445.

[20] I. M. Dahl, S. Kolboe, *Catal. Lett.* **1993**, *20*, 329-336.

[21] I. M. Dahl, S. Kolboe, *J. Catal.* **1994**, *149*, 458-464.

[22] I. M. Dahl, S. Kolboe, *J. Catal.* **1996**, *161*, 304-309.

[23] Ø. Mikkelsen, P. O. Rønning, S. Kolboe, *Microporous Mesoporous Mater.* **2000**, *40*, 95-113.

[24] B. Arstad, S. Kolboe, *Catal. Lett.* **2001**, *71*, 209-212.

[25] B. Arstad, S. Kolboe, *J. Am. Chem. Soc.* **2001**, *123*, 8137-8138.

[26] A. Sassi, M. A. Wildman, H. J. Ahn, P. Prasad, J. B. Nicholas, J. F. Haw, *J. Phys. Chem. B* **2002**, *106*, 2294-2303.

[27] M. Bjørgen, U. Olsbye, S. Kolboe, *J. Catal.* **2003**, *215*, 30-44.

[28] W. G. Song, J. B. Nicholas, A. Sassi, J. F. Haw, *Catal. Lett.* **2002**, *81*, 49-53.

[29] M. Bjørgen, U. Olsbye, D. Petersen, S. Kolboe, *J. Catal.* **2004**, *221*, 1-10.

[30] M. Bjørgen, F. Bonino, S. Kolboe, K. P. Lillerud, A. Zecchina, S. Bordiga, *J. Am. Chem. Soc.* **2003**, *125*, 15863-15868.

[31] M. Bjørgen, F. Bonino, B. Arstad, S. Kolboe, K. P. Lillerud, A. Zecchina, S. Bordiga, *ChemPhysChem* **2005**, *6*, 232-235.

[32] R. F. Sullivan, R. P. Sieg, G. E. Langlois, C. J. Egan, *J. Am. Chem. Soc.* **1961**, *83*, 1156.

[33] R. M. Dessau, R. B. Lapierre, *J. Catal.* **1982**, *78*, 136-141.

[34] R. M. Dessau, *J. Catal.* **1986**, *99*, 111-116.

[35] M. Bjørgen, S. Svelle, F. Joensen, J. Nerlov, S. Kolboe, F. Bonino, L. Palumbo, S. Bordiga, U. Olsbye, *J. Catal.* **2007**, *249*, 195-207.
[36] S. Svelle, P. A. Rønning, S. Kolboe, *J. Catal.* **2004**, *224*, 115-123.
[37] S. Svelle, P. O. Rønning, U. Olsbye, S. Kolboe, *J. Catal.* **2005**, *234*, 385-400.
[38] S. Svelle, F. Joensen, J. Nerlov, U. Olsbye, K. P. Lillerud, S. Kolboe, M. Bjørgen, *J. Am. Chem. Soc.* **2006**, *128*, 14770-14771.
[39] Z. M. Cui, Q. Liu, W. G. Song, L. J. Wan, *Angew. Chem. Int. Ed.* **2006**, *45*, 6512-6515.
[40] Z. M. Cui, Q. Liu, Z. Ma, S. W. Bian, W. G. Song, *J. Catal.* **2008**, *258*, 83-86.
[41] Z. M. Cui, Q. Liu, S. W. Baint, Z. Ma, W. G. Song, *J. Phys. Chem. C* **2008**, *112*, 2685-2688.
[42] J. Z. Li, Y. Qi, Z. M. Liu, G. Y. Liu, D. Z. Zhang, *Catalysis Letters* **2008**, *121*, 303-310.
[43] T. L. M. Maesen, M. Schenk, T. J. H. Vlugt, J. P. de Jonge, B. Smit, *Journal of Catalysis* **1999**, *188*, 403-412.
[44] R. Kumar, P. Ratnasamy, *J. Catal.* **1989**, *116*, 440-448.
[45] H. Robson, K. P. Lillerud, *Verified Synthesis of Zeolitic Materials* 2ed., Elsevier Amsterdam, **2001**.
[46] M. Bjørgen, F. Joensen, M. S. Holm, U. Olsbye, K. P. Lillerud, S. Svelle, *Appl. Catal. A* **2008**, *345*, 43-50.
[47] J. C. Groen, J. A. Moulijn, J. Perez-Ramirez, *Ind. Eng. Chem. Res.* **2007**, *46*, 4193-4201.
[48] M. S. Holm, M. K. Hansen, C. H. Christensen, *Eur. J. Inorg. Chem.* **2009**, 1194-1198.
[49] D. Bradon, W. D. Kaplan, *Microstructural Characterization of Materials*, John Wiley & Sons, Chichester, **2006**.
[50] B. Christian, B. M. Lynne, *Stud. Surf. Sci. Catal. 85*, 391-428
[51] S. Jørgensen. KJM 4010, *Scanning Electron Microscope*, University of Oslo, <http://www.nt.ntnu.no/users/torani/Training/Invitation_to_the_SEM_World.pdf>.
[52] C. B. Boss, K. J. Fredeen, *Concepts, Instrumentation and Techniques in Inductively Coupled Plasma Opyical Emission Spectrometer*, 3rd ed., PerkinElmer, USA, **2004**.
[53] S. Brunauer, P. H. Emmett, E. Teller, *J. Am. Chem. Soc.* **1938**, *60*, 309-319.
[54] www.tainstruments.com/library_download.aspx?file=TA231.PDF.
[55] P. O. Rønning, University of Oslo **1998** (Ph.D. thesis).
[56] D. Masih, T. Kobayashi, T. Baba, *Chem. Commun.* **2007**, 3303-3305.
[57] L. R. Martens, J. P. Verduijn, G. M. Mathys, *Catal. Today* **1997**, *36*, 451-460.
[58] R. M. Highcock, G. W. Smith, D. Wood, *Acta Crystallogr. Sect. C: Cryst. Struc. Commun.* **1985**, *41*, 1391-1394.
[59] M. Derewinski, M. Machowska, *Rec. Adv. Sci.Techno. Zeolites and Related Materials, Pts A - C* **2004**, *154*, 349-354.
[60] K. Hayasaka, D. Liang, W. Huybrechts, B. R. De Waele, K. J. Houthoofd, P. Eloy, E. M. Gaigneaux, G. van Tendeloo, J. W. Thybaut, G. B. Marin, J. F. M. Denayer, G. V. Baron, P. A. Jacobs, C. E. A. Kirschhock, J. A. Martens, *Chem. Eur. J.* **2007**, *13*, 10070-10077.
[61] P. J. Hogan, T. V. Whittam, J. J. Birtill, A. Stewart, *Zeolites* **1984**, *4*, 275 - 279.
[62] M. Derewinski, P. Sarv, A. Mifsud, *Catal. Today* **2006**, *114*, 197-204.
[63] H. V. Bekkum, E. M. Flanigen, P. A. Jacobs, J. C. Jansen, *Introduction to Zeolite Science and Practice*, Elsevier, **2001**.
[64] A. Zecchina, G. Spoto, S. Bordiga, *Phys. Chem. Chem. Phys.* **2005**, *7*, 1627-1642.
[65] S. H. Baeck, W. Y. Lee, *App. Catal. A* **1998**, *168*, 171-177.

[66] F. Wakabayashi, J. N. Kondo, K. Domen, C. Hirose, *J. Phys. Chem.* **1995**, *99*, 10573-10580.
[67] C. O. Arean, G. T. Palomino, F. Geobaldo, A. Zecchina, *J. Phys. Chem.* **1996**, *100*, 6678-6690.
[68] F. Geobaldo, S. Fiorilli, B. Onida, G. Giordano, A. Katovic, E. Garrone, *J. Phys. Chem. B* **2003**, *107*, 1258-1262.
[69] M. S. Holm, S. Svelle, F. Joensen, P. Beato, C. H. Christensen, S. Bordiga, M. Bjørgen, *Appl. Catal. A* **2009**, *356*, 23-30.
[70] H. Knozinger, S. Huber, *J. Chem. Soc., Faraday Trans.* **1998**, *94*, 2047-2059.
[71] M. Bjørgen, S. Kolboe, *Appl. Catal. A* **2002**, *225*, 285-290.
[72] Ø. Mikkelsen, S. Kolboe, *Microporous Mesoporous Mater.* **1999**, *29*, 173-184.
[73] F. Bleken, M. Bjørgen, L. Palumbo, S. Bordiga, S. Svelle, K. P. Lillerud, U. Olsbye, *Top. Catal.* **2009**, *52*, 218-228.
[74] S. H. Brown, D. Levin, R. Shinnar, W. A. Weber, *US Patent 6,372,949* **2002**.
[75] J. F. Haw, W. G. Song, D. M. Marcus, J. B. Nicholas, *Acc. Chem. Res.* **2003**, *36*, 317-326.
[76] J. A. Moulijn, M. Makkee, A. V. Diepen, *Chemical Process Technology*, Jon Wiley and Sons, **2001**.
[77] P. R. Courty, A. Chauvel, *Catal. Today* **1996**, *29*, 3-15.
[78] J. Bousquet, M. Valais, *Appl. Catal. A* **1996**, *134*, N8-N18.
[79] M. Bjørgen, U. Olsbye, S. Svelle, S. Kolboe, *Catal. Lett.* **2004**, *93*, 37-40.
[80] D. M. Marcus, W. G. Song, L. L. Ng, J. F. Haw, *Langmuir* **2002**, *18*, 8386-8391.
[81] B. P. C. Hereijgers, F. Bleken, M. H. Nilsen, S. Svelle, K. P. Lillerud, M. Bjørgen, B. M. Weckhuysen, U. Olysbye, *J. Catal.* **2009**, *DOI: 10.1016/j.jcat.2009.03.009*
[82] M. Bjørgen, F. Joensen, K. P. Lillerud, U. Olsbye, S. Svelle, *Catal. Today* **2009**, *142*, 90-97.
[83] S. Jiang, Y. K. Hwang, S. H. Jhung, J. S. Chang, J. S. Hwang, T. X. Cai, S. E. Park, *Chem. Lett.* **2004**, *33*, 1048-1049.